

https://dspace.org/

A First-Principles Study on Phase Stability, Electronic Structure and optical properties of some halide perovskites for photovoltaic applications

Abdallah Ali, Ibrahim Omer

2019
https://hdl.handle.net/10539/28192

Downloaded from a DSpace repository. https://dspace.org/



A First-Principles Study on Phase Stability, Electronic Structure and Optical Properties of some Halide Perovskites for Photovoltaic Applications

Ibrahim Omer Abdallah Ali
710353@students.wits.ac.za

Supervisor Professor Daniel P. Joubert
daniel.joubert2@wits.ac.za
Co-Supervisor Doctor Mohammed S. H. Suleiman
suleiman@aims.ac.za

A thesis submitted for the degree of Doctor of Philosophy (PhD) at the School of Physics.

Johannesburg, 2019

Declaration

I, the undersigned, hereby declare that the work contained in this PhD thesis is my original work, and that any work done by others or by myself previously has been acknowledged and referenced accordingly. This thesis is submitted to the University of the Witwatersrand, Johannesburg, in fulfillment of the requirements for the degree of Doctor of Philosophy (PhD) at the School of Physics. It has not been submitted before for any degree or examination in any other university.



Ibrahim Omer Abdallah Ali, 28 February 2019

Abbreviations

- DFT: Density Functional Theory
- MBPT: Many-Body Perturbation Theory
- EOS: Equation of State
- SMRT: Single-Mode Relaxation-Time
- BSE: Bethe-Salpeter Equation
- GW: G(Green's function) W (Screened coulomb interaction)
- PDOS: Partial Density of States
- SAIP: South African Institute of Physics
- KWAMS: Khartoum Workshop on Advances in Materials Science
- CSIR: Council for Scientific and Industrial Research
- CHPC: Centre for High Performance Computing
- ASESMA: African School on Electronic Structure Methods and Applications
- TWAS: The World Academy of Sciences
- NRF: The National Research Foundation
- SUST: Sudan University of Science and Technology
- WITS: University of the Witwatersrand
- GGA: Generalized Gradient Approximation

- PBE: Perdew, Burke and Ernzerhof
- TDOS: Total Density of States
- PDOS: Partial Density of States
- CBM: Conduction Band Minimum
- VBM: Valence Band Maximum
- SOC: Spin Orbit Coupling
- HSE: Heyd-Scuseria-Ernzerhof
- PCE: power conversion efficiency
- LED: Light Emitting Diodes
- PV: Photovoltaic
- DC: Direct Current
- AC: Alternating Current
- SQ: Shockley-Gueisser
- TE: Thermoelectric Effect
- LDA: Local Density Approximation
- HK: Hohenberg and Kohn
- KS: Kohn-Sham
- PAW: Projector Augmented Wave
- MBJ: Modified Becke Johnson
- HF: Hartree-Fock
- B3LYP: Becke, three-parameter, Lee-Yang-Parr
- QP: Quasi-Particle
- RPA: Random Phase Approximation
- IQP: Independent-Quasi-Particle
- DF: Distribution Function

- RTA: Relaxation Time Approximation
- TD: Transport Distribution
- BTE: Boltzmann Transport Equation
- PDF: Phonon Distribution Function
- VASP: Vienna Ab-initio Simulation Package
- MLWFS: Maximally-Localized Wannier Functions

Abstract

Hybrid and all-inorganic halide perovskites have recently emerged as new materials for solar cell applications leading to a new class of semiconductor photovoltaic cells. The power conversion efficiencies of perovskite based solar cells have been improved significantly to over 20%. This performance is due to the exceptional properties of hybrid halide perovskites displaying high absorption coefficients, high carrier mobility, direct and tunable band gaps and long diffusion lengths. However, poor long-term stability of organic-inorganic halide perovskite solar cells in oxygen and moisture remains the biggest challenge for realistic implementation of perovskite solar cells. In this thesis, we present a detailed ab-initio investigation of the structural, mechanical, dynamical stabilities, electronic, lattice thermal conductivities, transport and optical properties of the orthorhombic perovskites of hybrid methylammonium lead triiodide ($CH_3NH_3PbI_3$), hybrid methylammonium tin triiodide ($CH_3NH_3SnI_3$), and all-inorganic caesium lead triiodide ($CsPbI_3$).

Our theoretical calculations of the structural, mechanical, dynamical stabilities, electronic, lattice thermal conductivities, transport and optical properties are based on density functional theory (DFT) and many-body perturbation theory (MBPT) calculations. The structural properties (e.g. equilibrium lattice parameters and cohesive energy) were extracted from the calculated energy-volume equation of state (EOS). Mechanical and dynamical stabilities were tested on elastic constants and phonon dispersion relation, respectively. The lattice thermal conductivities were calculated within the single-mode relaxation-time (SMRT) approximation and linearized phonon Boltzmann equation as implemented in phono3py code. The calculations of the electronic transport properties of the optimized structure were performed using the Boltzmann transport theory within

the constant relaxation time approximation as implemented in the BoltzWann code. In order to investigate the optical spectra, we carry out Bethe-Salpeter equation (BSE) calculations on top of non-self-consistent G_0W_0 calculations.

Using the cohesive energy, we found that all the studied structures are energetically stable. The calculations of the elastic constants and phonon dispersions at zero pressure showed that $CH_3NH_3PbI_3$ and $CsPbI_3$ in the orthorhombic structures remained stable, while the orthorhombic $CH_3NH_3SnI_3$ is only stable at 0.7 GPa. The most energetically stable configurations were used to investigate electronic properties through total and partial density of states (PDOS) and band structure analysis. The calculated lattice thermal conductivities for $CH_3NH_3PbI_3$ and $CsPbI_3$ were found to be very low and anisotropic. Despite low thermal conductivity, $CH_3NH_3PbI_3$ in the orthorhombic phase at low temperature exhibits a very small figure of merit. This suggest that the orthorhombic $CH_3NH_3PbI_3$ is a poor candidate for thermoelectric applications. Finally, with the help of the frequency-dependent microscopic dielectric tensor we derived all the desired frequency-dependent optical spectra such as absorption coefficient, refractive index, reflectivity and energy-loss spectrum of the stable configurations. The average optical band gap of $CH_3NH_3PbI_3$, $CsPbI_3$ and $CH_3NH_3SnI_3$ was found to be 2.01 eV, 2.49 eV and 1.28 eV, respectively. This suggest that these materials in the orthorhombic phase may be potential material for solar photovoltaic applications. Using the Shockley-Queisser model we estimated the solar cell efficiency of the compounds.

Our obtained results were discussed within the employed theoretical methods and compared with experiment and with previous theoretical studies. Moreover, we report for the first time first theoretical attempt to study the mechanical and dynamical stabilities of lead-free tin halide perovskite under pressure. We hope that the present theoretical investigation would be helpful in providing a better theoretical knowledge of these materials.

Publications

1. Ibrahim Omer A Ali, Daniel P Joubert, and Mohamed S H Suleiman. First-Principles Calculations of the Electronic and Optical Properties of $CH_3NH_3PbI_3$ for Photovoltaic Applications. *Materials Today: Proceedings*, 5(4):10570-10576, 2018. Ref. [1].

2. Ibrahim Omer A Ali, Daniel P Joubert, and Mohammed S H Suleiman. A theoretical investigation of structural, mechanical, electronic and thermoelectric properties of orthorhombic $CH_3NH_3PbI_3$. *The European Physical Journal B*, 91(10):263, Oct 2018. Ref. [2]

3. Ibrahim Omer A Ali, Daniel P Joubert, and Mohammed S H Suleiman. First-principles investigation of lattice thermal conductivity and structural stability of $CH_3NH_3PbI_3$. In South African Institute of Physics 62nd Annual Conference (SAIP 2017), edited by Prof. Japie Engelbrecht (SU/2017), pp. 2 - 7. ISBN: 978-0-620-82077-6, Dec 2018. Available online at http://events.saip.org.za. Ref. [3]

4. Ibrahim Omer A Ali, Daniel P Joubert, and Mohammed S H Suleiman. Investigation of Thermoelectric Properties of $CH_3NH_3PbI_3$: Density Functional Theory and Boltzmann Transport Calculations. In South African Institute of Physics 62nd Annual Conference (SAIP 2017), edited by Prof. Japie Engelbrecht (SU/2017), pp. 8 - 13. ISBN: 978-0-620-82077-6, Dec 2018. Available online at http://events.saip.org.za. Ref. [4]

5. Ibrahim Omer A Ali, Daniel P Joubert, and Mohammed S H Suleiman. First-Principles Study of Structural, Mechanical, Dynamical Stabilities, Electronic and

Optical Properties of Orthorhombic $CH_3NH_3SnI_3$ Under Pressure. *Under review*

Presentations and Activities

1. 4 - 17 January 2017, 3rd Khartoum Workshop on Advances in Materials Science (KWAMS'17), University of Khartoum, Khartoum, **Sudan**.
2. 28 - 31 March 2017, 1st Africa Energy Materials Conference, the Council for Scientific and Industrial Research (CSIR), Pretoria, **South Africa**.
3. 03 - 07 July 2017, 62rd Annual Conference of the South African Institute of physics (SAIP2017), University of Cape Town, Cape Town, **South Africa**. Investigation of Thermoelectric Properties of $CH_3NH_3PbI_3$: Density Functional Theory and Boltzmann Transport Calculations talk presentation
4. 03 - 07 July 2018, 62rd Annual Conference of the South African Institute of physics (SAIP2018), University of Cape Town, Cape Town, **South Africa**. First-principles investigation of lattice thermal conductivity and structural stability of $CH_3NH_3PbI_3$ poster presentation
5. 15 - 20 January 2018, The 8th CHPC Introductory Programming Summer School. Hosted by Northwest-University (NWU) Potchefstroom and the Centre for High Performance Computing (CHPC) of the Council for Scientific and Industrial Research (CSIR) and funded by the Department of Science and Technology (DST), **South Africa**.
6. 22 Oct 2018 - 02 Nov 2018, 5th African School on Electronic Structure Methods and Applications (ASESMA 2018), Addis Ababa Science and Technology University (AASTU), Addis Ababa, **Ethiopia**.

DEDICATION

To my beloved family, to the soul of my parents and to the soul of my niece.

ACKNOWLEDGEMENTS

I would like to give a warm thanks to both on my supervisors, Daniel P. Joubert and Mohammed S. H. Suleiman, for their valuable guidance and close follow up throughout the course of this project. Their dedication, time and knowledge have been of great importance to the progress of the project.

Thanks to Professor Daniel P. Joubert for giving me an opportunity to work in his research group and for the best support I could wish for. I thank him for playing major role in my career development. Special thanks to Dr. Mohammed S. H. Suleiman for his reserved effort in reading my thesis and correcting errors and also for the knowledge and tips he has shared with me.

I would like to thank my family. Great appreciation to my wives, my daughters , son and my brothers for their encouragement and prayers. To those who indirectly contributed in this research, your kindness means a lot to me. Thank you very much.

This thesis was fully funded by TWAS-NRF Doctoral Fellowships, University of the Witwatersrand, and Sudan University of Science and Technology (SUST). This support is gratefully acknowledged.

The Centre for High Performance Computing (CHPC), Cape Town (South Africa) is acknowledged for providing computational resources.

Contents

Declaration i

Abbreviations ii

Abstract v

Publications vii

Presentations ix

Dedication x

Acknowledgements xi

List of Figures xix

List of Tables xxi

1 Introduction 1

1.1 Motivations and Overview 1
1.2 Photovoltaics 2
1.3 Thermoelectricity 4
1.4 Halide Perovskites 6
1.5 Aims 10
1.6 Structure of this Thesis 11

2 Theoretical Methods 12

2.1 Many-Body Problem: The Basic Problem . . . 12
2.2 Born-Oppenheimer Approximation . . . 14
2.3 Electronic Density . . . 16
2.4 Density Functional Theory (DFT) . . . 17
2.4.1 The Hohenberg-Kohn Theorems . . . 17
2.4.2 Constrained Search Formulation . . . 19
2.4.3 The Kohn-Sham (KS) Equations . . . 19
2.4.4 Spin-orbit Coupling (SOC) . . . 21
2.4.5 Solving Kohn-Sham Equations . . . 21
2.5 Many Body Perturbation Theory (MBPT) . . . 27
2.5.1 Quasi-Particle (QP) . . . 27
2.5.2 GW Approximation . . . 29
2.5.3 Bethe-Salpeter Equation (BSE) . . . 30
2.6 Transport Phenomena . . . 33
2.6.1 The Boltzmann Equation . . . 33
2.6.2 Transport Coefficients . . . 35
2.7 Lattice Thermal Conductivity . . . 37

3 Computational Details **39**
3.1 DFT Calculations . . . 39
3.2 Calculations of Structural Properties . . . 41
3.2.1 Cohesive Energy . . . 41
3.2.2 Bulk Modulus and its Pressure Derivative B' . . . 42
3.2.3 Equation of State and Lattice Parameters . . . 42
3.3 Stability Properties . . . 43
3.3.1 Elastic Stability . . . 43
3.3.2 Dynamical Stability . . . 46
3.4 Electronic Density of States (DOS) . . . 47
3.5 Electronic Transport Properties . . . 48
3.6 Lattice Thermal Conductivity . . . 49
3.7 GW and BSE Calculations Detail . . . 50
3.8 Microscopic Dielectric . . . 50
3.9 Optical Spectra Calculations . . . 51

4 Results and Discussions **52**

4.1 **Methylammonium Lead Triiodide Perovskite** . . . 52
4.1.1 Structural Properties . . . 52
4.1.2 Mechanical Stability . . . 54
4.1.3 Dynamical Stability . . . 55
4.1.4 Electronic Properties . . . 56
4.1.5 Lattice Thermal Conductivity . . . 59
4.1.6 Electronic Transport Properties . . . 61
4.1.7 Optical Properties . . . 64
4.2 **Caesium Lead Triiodide Perovskite** . . . 66
4.2.1 Structural Properties . . . 67
4.2.2 Mechanical Stability . . . 68
4.2.3 Dynamical Stability . . . 69
4.2.4 Electronic Properties . . . 70
4.2.5 Lattice Thermal Conductivity . . . 72
4.2.6 Optical Properties . . . 74
4.3 **Methylammonium Tin Triiodide Perovskite** . . . 76
4.3.1 Structural Properties . . . 76
4.3.2 Mechanical Stability . . . 77
4.3.3 Dynamical Stability . . . 78
4.3.4 Electronic Properties . . . 80
4.3.5 Optical Properties . . . 81

5 Conclusions and Future Work **85**
5.1 Conclusions . . . 85
5.1.1 $APbI_3$ (A = CH_3NH_3 or Cs) . . . 85
5.1.2 Methylammonium Tin Triiodide Perovskite . . . 87
5.2 Future Work . . . 89

Appendix A Hartree-Fock Approximation **90**

Appendix B Greenfls Function **94**

Appendix C Vienna Ab-initio Simulation Package (VASP) **96**

Appendix D Dielectric Function **98**

Appendix E Efficiency of Halide Perovskites **102**

References **104**

List of Figures

1.1 Fundamental solar cell efficiency limits for AM1.5 solar spectrum. 4

3.1 (Color online) The crystal structure of the $CH_3NH_3XI_3$ (X= Pb or Sn) orthorhombic phase with space group Pnma (No. 62) (left) the Brillouin zone of the orthorhombic lattice (right) [5]. 40

3.2 (Color online) The crystal structure of the $CsPbI_3$ orthorhombic phase with space group Pnma (No. 62). 41

4.1 (Color online) Energy-volume equation of states using PBE and PBEsol for the orthorhombic $CH_3NH_3PbI_3$. 53

4.2 (Color online) Low-frequency regions of the calculated phonon dispersion relation of $CH_3NH_3PbI_3$ using PBEsol (the full vibrational frequency spectra spans up to 100 THz). 56

4.3 The heat capacity at constant volume as a function of temperature for the orthorhombic $CH_3NH_3PbI_3$. The inset shows specific heat C_v when temperature goes from 0 K up to 150 K. 57

4.4 (Color online) DFT calculated electronic structure of the orthorhombic $CH_3NH_3PbI_3$: band structure (left), total density of states (TDOS) and $CH_3NH_3^+$ cation projected density of states PDOS (middle), and Pb and I atomic orbital PDOS. 58

4.5 (Color online) DFT calculated band structure of the orthorhombic $CH_3NH_3PbI_3$ using PBEsol including spin orbit-coupling (SOC). 59

4.6 (Color online) The calculated lattice thermal conductivity ($Wm^{-1}K^{-1}$) in the a-, b- and c-directions for the orthorhombic $CH_3NH_3PbI_3$. 60

4.7 (Color online) The phonon group velocities (Left) and the phonon lifetimes (Right) for the orthorhombic $CH_3NH_3PbI_3$ at 150 K in the first Brillouin zone. 61
4.8 (Color online) Variation of Seebeck coefficient with respect to chemical potential μ for the orthorhombic $CH_3NH_3PbI_3$ at different temperatures in the (a) a-direction, (b) b-direction, and (c) c-direction. 62
4.9 (Color online) Variation of electrical conductivity σ with respect to chemical potential μ for the orthorhombic $CH_3NH_3PbI_3$ at different temperatures in the (a) a-direction, (b) b-direction, and (c) c-direction. 63
4.10 (Color online) Variation of electronic thermal conductivity κ_e with respect to chemical potential μ for the orthorhombic $CH_3NH_3PbI_3$ at different temperatures in the (a) a-direction, (b) b-direction, and (c) c-direction. 63
4.11 (Color online) Calculated power factor $S^2\sigma$ with respect to chemical potential μ for the orthorhombic $CH_3NH_3PbI_3$ at different temperatures in the (a) a-direction, (b) b-direction, and (c) c-direction. 63
4.12 (Color online) Calculated figure of merit with respect to chemical potential μ for the orthorhombic $CH_3NH_3PbI_3$ at different temperatures in the (a) a-direction, (b) b-direction, and (c) c-direction. 64
4.13 (Color online) Optical spectra for the orthorhombic $CH_3NH_3PbI_3$ calculated using PBEsol: (a) real $\varepsilon_{re}(\omega)$ and the imaginary $\varepsilon_{im}(\omega)$ parts of the dielectric function, (b) Refraction $n(\omega)$ and extinction coefficient $k(\omega)$, (c) Energy loss $L(\omega)$ and absorption coefficient $\alpha(\omega)$. 65
4.14 (Color online) Tauc plot of the absorption coefficient, showing the polarization-dependent onsets for the orthorhombic $CH_3NH_3PbI_3$. 66
4.15 Calculated total binding energy versus volume using PBE and PBEsol of the orthorhombic $CsPbI_3$. 68
4.16 (Color online) Phonon dispersion relation graph of the orthorhombic $CsPbI_3$ calculated using PBEsol. 70
4.17 The heat capacity at constant volume as a function of temperature for the orthorhombic $CsPbI_3$. The inset shows specific heat C_v when temperature goes from 0 K up to 150 K. 71

4.18 (Color online) DFT calculated electronic structure of the orthorhombic $CsPbI_3$: band structure (left), total density of states (TDOS) and Cs^+ cation projected density of states PDOS (middle), and Pb and I atomic orbital PDOS. 72
4.19 (Color online) The calculated lattice thermal conductivity ($Wm^{-1}K^{-1}$) in the *a*-, *b*- and *c*-directions for the orthorhombic $CsPbI_3$. 73
4.20 (Color online) The phonon group velocities (Left) and the phonon lifetimes (Right) for the orthorhombic $CsPbI_3$ at 150 K in the first Brillouin zone. 73
4.21 (Color online) Optical spectra of the orthorhombic $CsPbI_3$ calculated using PBEsol: (a) real $\varepsilon_{re}(\omega)$ and the imaginary $\varepsilon_{im}(\omega)$ parts of the dielectric function, (b) Refraction $n(\omega)$ and extinction coefficient $k(\omega)$, (c) Energy loss $L(\omega)$ and absorption coefficient $\alpha(\omega)$. 74
4.22 (Color online) Tauc plot of the absorption coefficient, showing the polarization-dependent onsets of the orthorhombic $CsPbI_3$. 75
4.23 (Color online) The crystal structure of the $CH_3NH_3SnI_3$ orthorhombic phase with space group Pnma (No. 62). 77
4.24 Phonon dispersion curves at (a) 0 GPa and (b) 0.7 GPa for the orthorhombic $CH_3NH_3SnI_3$. 79
4.25 (Color online)DFT calculated electronic structure of the orthorhombic $CH_3NH_3SnI_3$ at 0.7 GPa: band structure (left), total density of states (TDOS) and $CH_3NH_3^+$ cation projected density of states PDOS (middle), and Sn and I atomic orbital PDOS. 81
4.26 (Color online) The calculated real parts $\varepsilon_{re}(\omega)$ and imaginary parts $\varepsilon_{im}(\omega)$ of the dielectric tensor for polarization vectors *a*, *b*, and *c* for the orthorhombic $CH_3NH_3SnI_3$. 82
4.27 (Color online) The calculated refractive index $n(\omega)$ and reflectivity $R(\omega)$ for polarization vectors *a*, *b*, and *c* for the orthorhombic $CH_3NH_3SnI_3$. . 82
4.28 (Color online) The calculated absorption coefficient $\alpha(\omega)$, energy loss $L(\omega)$ and the Tauc plot of the absorption coefficient for polarization vectors *a*, *b*, and *c* for the orthorhombic $CH_3NH_3SnI_3$. 83
4.29 (Color online) Tauc plot of the absorption coefficient for the orthorhombic $CH_3NH_3SnI_3$, showing the polarization-dependent onsets. 83

E.1 Estimated efficiency of $CH_3NH_3PbI_3$ (red point) using Shockley-Queisser model. 102
E.2 Estimated efficiency of $CsPbI_3$ (red point) using Shockley-Queisser model. 103
E.3 Estimated efficiency of $CH_3NH_3SnI_3$ (red point) using Shockley-Queisser model. 103

List of Tables

4.1 Calculated and experimental equilibrium parameters of the orthorhombic $CH_3NH_3PbI_3$: Lattice constants (a(Å), b(Å), c(Å)), equilibrium volume V_0(Å^3) and cohesive energy E_{coh} (eV/atom). 53

4.2 PBE and PBEsol calculated independent elastic constants C_{ij} for the orthorhombic $CH_3NH_3PbI_3$ in (GPa) compared other theoretical study (PBE+D2). 54

4.3 The calculated bulk moduli (B_R, B_V, B_H in GPa), shear moduli (G_R, G_V, G_H in GPa), Young's modulus for the orthorhombic $CH_3NH_3PbI_3$ (E in GPa), and the other theoretical study. 54

4.4 The calculated B/G ratio, Poisson's ratio (ν), the shear anisotropic factors (A_1, A_2, A_3) for the orthorhombic $CH_3NH_3PbI_3$, with the corresponding theoretical study. 54

4.5 Our calculated, reported experimental electronic band gap of the orthorhombic $CH_3NH_3PbI_3$. 58

4.6 The calculated lattice thermal conductivity ($Wm^{-1}K^{-1}$) in the a-, b- and c-directions with the corresponding average values for the orthorhombic $CH_3NH_3PbI_3$. 60

4.7 Calculated equilibrium parameters of the orthorhombic $CsPbI_3$: Lattice constants (a(Å), b(Å), c(Å)), equilibrium volume V_0(Å^3) and cohesive energy E_{coh}(eV/atom) compared with the other experimental (Exp.) and theoretical study (PBE). 67

4.8 Calculated independent elastic constants in (GPa) for the orthorhombic $CsPbI_3$. 69

4.9 The calculated bulk moduli (B_R, B_V, B_H in GPa), shear moduli (G_R, G_V, G_H in GPa), Young's modulus (E in GPa) of the orthorhombic $CsPbI_3$. 69
4.10 Our calculated, reported experimental electronic band gap of the orthorhombic $CsPbI_3$. 71
4.11 Calculated parameters of the orthorhombic $CH_3NH_3SnI_3$: Lattice constants (a(Å), b(Å), c(Å)), initial volume V_0(Å^3) and cohesive energy E_{coh} (eV/atom) at 0.7 GPa compared with the other experimental and theoretical study at zero-pressure. 77
4.12 Calculated independent elastic constants for the orthorhombic $CH_3NH_3SnI_3$ in GPa (Cal.) at 0.7 GPa compared with the other theoretical study (PBE+D2) at zero-pressure. 78
4.13 The calculated bulk moduli B in GPa, shear moduli G in GPa and Young's modulus E_H in GPa (Cal.) for the orthorhombic $CH_3NH_3SnI_3$ at 0.7 GPa compared with the other theoretical study (PBE+D2) at zero-pressure. 78
4.14 The calculated B/G ratio, Poisson's ratio (ν), the shear anisotropic factors (A_1, A_2, A_3) (Cal.) for the orthorhombic $CH_3NH_3SnI_3$ at 0.7 GPa, with the corresponding theoretical study (PBE+D2) at zero-pressure. . 79
4.15 Calculated electronic band gap of the orthorhombic $CH_3NH_3SnI_3$ perovskite at 0.7 GPa compared to experimentally reported ones at zero-pressure (Exp.) and to previous theoretical study using HSE06 at zero-pressure (Theory). 80

1

Introduction

1.1 Motivations and Overview

The search for renewable sources of energy has been the focus of huge scientific research in the last few decades, with the view to benefit from an alternative source of energy to prevent the possible global energy crises. Historically, photovoltaic devices can be generally classified into three generations: First generation solar cells using crystalline silicon shows high power conversion efficiency PCE of more than 20%, but this technology is facing a strong challenge due to relatively high production cost at large-scale. The second generation solar cells are thin-film solar cells based on amorphous silicon, CIGS and CdTe, with lower cost than the first generation have a PCE of around 19.6%, but they are also facing problems in large-scale production. The third generation solar cells aim to achieve high PCE devices but still use thin-film technologies using organic or organometallic materials as well as inorganic materials, with low cost and high efficiency, however, complex fabrication process. A new class of thin-film solar cells currently under investigation are perovskite solar cells [6, 7].

Since the first efficient solid-state perovskite solar cells were reported in mid-2012 [8], rapid development of the organic-inorganic hybrid halide perovskites have been made, and a new era in optoelectronic and solar cells technologies has emerged. This family of perovskite materials possesses interesting properties such as high carrier mobility, an adjustable spectral absorption range, strong solar absorption, long diffusion lengths, and ease of fabrication [8, 9]. The unique attributes of these perovskites make the

hybrid halide perovskites highly promising materials for various practical applications including high performance in converting solar light into electrical power [9, 10], light emitting diodes (LED), photodetectors and lasers [9].

1.2 Photovoltaics

Photovoltaic (PV) is the conversion of light energy (sunlight) directly into electricity [11]. The elementary cornerstone of the PV technology is the so-called solar cell. Solar cells are made of semiconductor materials and can be as a two-semiconductor device which conduct like a diode in the dark and generates a photo-voltage when charged by the sun. The working principle of solar cells system are based on the so-called photovoltaic effects. The photovoltaic effect was first reported by a French physicist, Edmund Bequerel in 1839 [11, 12].

PV cells are connected in series and in parallel in order to produce useful DC voltage and current level, and this DC voltages is converted to AC power of appropriate frequency using power electronic inverter [12].

Shockley-Queisser Model

The efficiency of photovoltaic system is calculated using two models, Shockley-Gueisser (SQ) model (also called detailed balance limit) and spectroscopy limited maximum efficiency model. The Shockley-Queisser (SQ) limit is the theoretical maximum efficiency that can be achieved by a solar cell with a certain band gap and at standard testing conditions [1] [13, 14]. In Shockley-Gueisser model, the maximum ultimate efficiency η^* [2] is defined as the maximum output power density (P_{max}) derived by the cell and the total incident power density from the solar spectrum (P_{in}) impinging on the cell

$$\eta^* = \frac{P_{\text{max}}}{P_{\text{in}}}. \tag{1.2.1}$$

[1] Standard testing conditions:

1. 25* cell temperature.
2. Air mass (AM) 1.5.
3. One sun illumination (1000 W/m^2).

[2] To obtain the ultimate effieciency η^*, an idealized solar cell model with $T_c = 0K$ is considered. it is surrounded by a balckbody with temperature of $T_s = 600K$.

The maximum output per unit area per unit time can be expressed as:

$$P_{\max} = E_g N_s, \tag{1.2.2}$$

where E_g is the band gap of the absorber and N_s is the number of incident photon per unit area per unit time with energy above E_g. The total number of photons frequency greater than E_g impinging from the sun, assumed as a blackbody at temperature T_s, in unit time and falling upon the solar cell per unit area N_s is given by:

$$N_s = \frac{2\pi(k_B T_s)^3}{h^3 c^2} \int_{x_g}^{\infty} \frac{x^2 dx}{e^x - 1}, \tag{1.2.3}$$

where h, c, k_B and T_s are the Planck constant, the speed of light, the Boltzmann constant and the temperature of the sun respectively and $x_g = E_g/(k_B T_s)$. Incontrast, the total incident energy density coming from sun at T_s and falling upon the solar cell, P_{in} is given by [14, 15]

$$\begin{aligned} P_{\mathrm{in}} &= \frac{2\pi(k_B T_s)^4}{h^3 c^2} \int_0^{\infty} \frac{x^3 dx}{e^x - 1}, \\ &= \frac{2\pi(k_B T_s)^4}{15 h^3 c^2}. \end{aligned} \tag{1.2.4}$$

The maximum value of the η^* is approximately 44% for the optimized band gap energy of 1.1 eV [14].

The Shockley-Gueisser limit is calculated by examining the amount of electrical energy that is extracted per phonon of incoming sunlight. To estimate the upper limit of each device concept, different assumptions are made. There are four unavoidable losses that limit the solar conversion efficiency of a device with a single absorption threshold or band gap: only photons with an energy above the band gap can be absorbed (incomplete absorption), excess energy from high energy photons will be lost (thermalization), blackbody radiation causes spontaneous emission of photons, and a small fraction of carriers will recombine (radiative recombination) [16]. A summary of theses losses can be shown in Figure 1.1 [17].

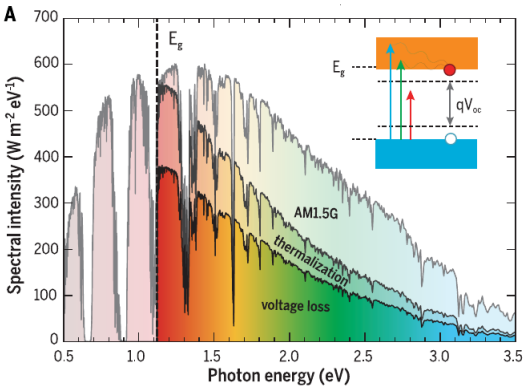


Figure 1.1: Fundamental solar cell efficiency limits for AM1.5 solar spectrum.

1.3 Thermoelectricity

The thermoelectric effect (TE) describes two fundamental phenomena, namely, the Seebeck effect [18] and the Peltier effect [19]. In the Seebeck effect, temperature gradient is directly converted to electrical current. A related effect, the Peltier effect, involves direct conversion of a voltage difference to a temperature gradient [20].

Seebeck Effect

The Seebeck effect was discovered in early 1800s by T. J. Seebeck [18]. Seebeck showed that by joining together two different materials, A and B, and holding the two junctions at different temperatures, say T_h and T_c ($< \mathrm{T}_h$), develops a voltage difference ΔV across the two junctions [20]. Under open circuit, the potential difference is proportional to the temperature difference; i.e.

$$\Delta V = -S_{\mathrm{AB}} \Delta T = -S_{\mathrm{AB}} (T_h - T_c), \tag{1.3.1}$$

where S_{AB} is the differential Seebeck coefficient, known as the thermopower and T_h is the hot-side temperature, T_c is the temperature of cold-side [21, 22].

Peltier Effect

Opposite to the Seebeck effect, in 1834, the Peltier effect was discovered by the French physicist Jean Charles Athanase Peltier. Peltier observed that when an electric current

is made to flow through the junction of two different materials, A and B, heat is either absorbed or rejected at the junction [20, 23, 24]. The heat generated per unit time is

$$\dot{Q} = \Pi_{\mathrm{AB}} I = (\Pi_{\mathrm{A}} - \Pi_{\mathrm{B}}) I, \tag{1.3.2}$$

where Π_{AB} is the relative Peltier coefficient and I is the electric current. The two effects (Seebeck and Peltier) are coupled to each other via [23]

$$\Pi = ST. \tag{1.3.3}$$

Thermoelectric Figure of Merit

The efficiency of thermoelectric materials is characterized by a dimensionless figure of merit ZT[3],

$$ZT = \frac{S^2\sigma}{\kappa} T, \tag{1.3.4}$$

where S, σ, T and κ are the Seebeck coefficient, electrical conductivity, temperature and total thermal conductivity, respectively [20]. The term $S^2\sigma$ is called the power factor. The total thermal conductivity κ is constituted by two contributions electronic thermal conductivity (κ_e) and lattice thermal conductivity (κ_L); i.e., $\kappa = \kappa_e + \kappa_L$. The electronic thermal conductivity κ_e is coupled to the electrical conductivity σ through the Wiedemann-Franz law [20, 24]

$$\kappa_e = \sigma L T, \tag{1.3.5}$$

where L is known as Lorenz number. To obtain a high figure of merit (ZT) from equation (1.3.4), large Seebeck coefficient (S) and electrical conductivity (σ) are desired, while thermal conductivity (κ) must be minimized [24].

[3] "The expressions for figure of merit , Z and ZT, are used interchangeably in the field of TE. Z is the figure of merit with units of 1/K (1/T), and ZT is the standard notation for the dimensionless figure of merit" [20].

Thermoelectric Efficiency

The power generation efficiency (η) of a thermoelectric couple is given by the energy supplied to the couple (W) over the net heat flow rate ($\dot{Q}_h$) at the hot junction

$$\begin{aligned}\eta &= \frac{W}{\dot{Q}_h} \\ &= (T_h - T_c)/T_h[(\sqrt{1+ZT_{\text{ave}}} - 1)/(\sqrt{1+ZT_{\text{ave}}} + T_c/T_h)],\end{aligned} \tag{1.3.6}$$

where T_{ave} is the average temperature. Thus, from equation (1.3.6), one can see that the power generation efficiency η is proportional to $(1+ZT_{\text{ave}})$ and that the efficiency η approaches the Carnot efficiency if ZT approaches infinity [20, 24].

1.4 Halide Perovskites

Perovskite refers to the crystal structure of the mineral calcium titanium oxide ($CaTiO_3$), discovered by Gustav Rose [25, 26]. This structure was characterized by Russian mineralogist Lev A. Perovski, from which it derives its name. Perovskites are materials described by the chemical formula ABX_3, where A and B are cations of different sizes and X is an anion [8, 9]. The perovskite structure has been found in different types, for example oxide and halide perovskites. The latter materials family spans organic-inorganic hybrid halide perovskites as well as all-inorganic halide perovskites [27]. The stability and phase of a perovskite structure strongly depend on the relative sizes of the constituent ions. The relationship between anions and cations, determined whether they form the perovskite structure, set by Goldschmidt, who introduced the tolerance factor,

$$t = \frac{r_{\text{A}} + r_{\text{X}}}{\sqrt{2}(r_{\text{B}} + r_{\text{X}})}, \tag{1.4.1}$$

where r_A, r_B and r_X are the ionic radii of the A-, B- and X-site ions, respectively [28, 29].

In the organic-inorganic hybrid halide perovskites, the large cation A is usually the methylammonium ion (CH_3NH_3), but formamidinium ($NH_2CH{=}NH_2$) and ethylammonium ($CH_3CH_2NH_3$) are also possible. The small cation B is normally Pb, but, if possible, replacement of Pb by Sn is recommended, because, non-toxic Sn-based perovskites show high charge carrier mobilities and strong absorption in the infrared (IR)

region [30]. The anion X is a halogen ion, usually I, but F, Cl and Br are also of interest [8, 10]. In addition, perovskites with mixed halides (e.g. $CH_3NH_3PbI_{3-x}Cl_x$ and $CH_3NH_3PbI_{3-x}Br_x$) and/or mixed Sn-Pb (e.g. $CH_3NH_3Sn_xPb_{1-x}I_3$ [31]) are also being considered.

In all-inorganic halide perovskites the cation A is Cs, but Rb is also possible. The cation B is normally Pb, but Sn is of interest and the X anion is a halogen [32]. Caesium lead halides have a perovskite structure, and generally reported by Moller, with the general formula $CsPbI_3$ (X = Cl, Br or I) [33].

Methylammonium Lead Iodide Perovskite

Methylammonium lead iodide perovskite $CH_3NH_3PbI_3$ was first reported by Weber in 1978 [34]. Depending on temperature, $CH_3NH_3PbI_3$ perovskites can exist in any of the following sable phases cubic (space group $Pm\bar{3}m$, at $T \geq 327$ K) [35], tetragonal (space group I4/mcm, at $165 \leq T \leq 327$ K) [30] or orthorhombic (space group Pnma, $T < 165$ K) [36]. It is believed that perovskite can function - in solar cells - at the highest efficiencies in simplified device architectures, without the need for complex nanostructures [37].

In recent years, due to experimental progress, many theoretical investigations using density functional theory on electronic and structural properties of hybrid halide perovskites are emerging. Different approaches have been adopted, using local density approximation (LDA), generalized gradient approximation (GGA), hybrid functional methods (HSE), and quasi-particle GW methods [38]. In 2004, Chang et al. [39] studied structural and electronic properties of cubic ($CH_3NH_3PbI_3$) using (LDA) and found that the effects of the organic molecule on the electronic and optical properties are weak. Wang et al. [40] investigated the orthorhombic phase of $CH_3NH_3PbI_3$ by first-principles calculations using local, semi-local and non-local exchange-correlation approximations. In their calculations, the theoretical band gap is found to be 1.74 eV. Brevio F. et al. [41] studied the vibrational spectra of the orthorhombic phase of $CH_3NH_3PbI_3$. Other studies by Feng [42] investigated the mechanical properties of the cubic, tetragonal and orthorhombic phases of $CH_3NH_3AI_3$ (A = Pb or Sn). However, to the best of our knowledge, the dynamical and mechanical properties of orthorhombic perovskite $CH_3NH_3PbI_3$ have not been investigated extensively.

Resent experimental studies show that $CH_3NH_3PbI_3$ is characterized by an ultra-low

thermal conductivity of 0.5 $Wm^{-1}K^{-1}$ for millimeter size single crystal and 0.3 $Wm^{-1}K^{-1}$ for polycrystals [43] at room temperature, and a large Seebeck coefficient (-6500 μV/K) was reported [30], which are ideal properties for thermoelectric applications. However, the electrical conductivity needs to be enhanced. This could be done by photoinduced doping (in $CH_3NH_3PbI_3$) [44]. The theoretical study using density functional theory by Xin Qian et al. [45] found a very low thermal conductivity (0.59 $Wm^{-1}K^{-1}$) for the tetragonal phase of $CH_3NH_3PbI_3$ at room temperature, and higher thermal conductivity for the pseudocubic phase of $CH_3NH_3PbI_3$ (1.8 $Wm^{-1}K^{-1}$) at 330 K.

Zhao et al. [46] studied the thermoelectric transport properties of both cubic and tetragonal phases of $CH_3NH_3PbI_3$ using density functional theory and Boltzmann transport equation. In their study, they found that at the impurity concentration $10^{18}cm^{-3}$ and room temperature the figure of merit ZT value of tetragonal phase could be optimized to reach unity, and the hole-doped $CH_3NH_3PbI_3$ exhibits superior thermoelectric property than the electron-doped one. Y. He and Galli [47] used ab-initio calculations to study $CH_3NH_3AI_3$ (A = Pb and Sn) for solar thermoelectric applications and they realized that it is possible to have figure of merit ZT ranging from (1 to 2) by optimizing the lattice thermal conductivity through engineering the perovskite superlattices. Their study shows that the maximum ZT values can be obtained from electron doping rather than from hole doping. Lee et al. [48] used density functional theory to study ABI_3 (A= CH_3NH_3, CH_3CHNH_2; B = Pb, Sn) as potential thermoelectric materials, and they suggested that ABI_3 in terms of power factor ($S^2\sigma$) alone has a poor thermoelectric performance, but it can be increased to the levels of the existing best thermoelectric counterpart (Bi_2Te_3) by electron doping.

Caesium Lead Iodide Perovskite

At higher temperature (634 K), $CsPbI_3$ possesses a cubic phase (space group $Pm\bar{3}m$) [49]. As temperature decreases, the cubic phase is transformed to a tetragonal phase [50], but there is no clearly define temperature range in the literature. At low temperatures (i.e. 293 K [30] and 298 K [49]), CsPbI3 possesses an orthorhombic phase (space group Pnma) known as yellow phase.

Eperson et al. [51] fabricated working inorganic $CsPbI_3$ solar cells for the first time, with band gap of 1.73 eV for the black phase and 2.82 eV for the yellow phase. Chang et al. [39] calculated the structural and electronic properties for the cubic $CsPbX_3$ (X

= Cl, Br or I) by first-principles calculations. In their study, the theoretical band gap is found to be 1.46 eV, 1.12 eV and 1.1 eV for the anions Cl, Br and I, respectively. Murad et al. [50], in 2017 investigated the structural, electronic and optical properties of the cubic, tetragonal and orthorhombic phases of $CsPbX_3$ (X = Cl, Br or I) for solar cells and energy storage applications, using density functional theory. In their study, the calculated band gap is found to be 1.68 eV for the orthorhombic $CsPbI_3$, which is underestimated compared to the experimental one 2.82 eV. However, other calculations [52] predicted an energy band gap of 2.64 eV.

Calculations of room-temperature lattice thermal conductivity showed very low values of 0.54 $Wm^{-1}K^{-1}$ and 0.25 $Wm^{-1}K^{-1}$ for cubic $CsSnI_3$ and $CsPbI_3$, respectively [32]. The maximal figure of merit ZT at 1000 K was found, in the same study [32], to be 0.63 and 0.64 for n-type $CsSnI_3$ and $CsPbI_3$, respectively.

Methylammonium Tin Iodide Perovskite

$CH_3NH_3PbX_3$ (X = Cl, Br or I) is considered as a promising material for solar cell application with an expected photo conversion efficiency 20.1% [38, 53]. However, this progress in efficiency, is hindered by many challenges such as the instability of many its phases [54] and the toxicity of lead [55]. Therefore, it is necessary to find an alternative stable material that does not contain toxic lead. A possible candidate is methylammonium tin iodide perovskite, $CH_3NH_3SnI_3$, which has been reported to have a band gap of 1.21 eV and 1.35 eV depending on the preparation method [30]. Depending on temperature, $CH_3NH_3SnX_3$ (X = Cl, Br or I) reveals a very rich phase diagram, in which the crystal goes from cubic, tetragonal, orthorhombic and monoclinic to triclinic phase by cooling (see Refs. 19-24 in [56]). At room temperature, $CH_3NH_3SnI_3$ presents a cubic phase, and it changes to tetragonal at 275 K, and to orthorhombic at 110 K [57, 58].

The first lead-free solar cell made of tin halide perovskite was demonstrated by Snaith's group [55] and Hao's group [59] in 2014; however stability of the material was a challenge. Hao et al. investigated the photovoltaics of tetragonal phase of $CH_3NH_3SnI_3$ and found that $CH_3NH_3SnI_3$ is a direct-gap semiconductor with an energy gap of 1.35 eV, which is significantly redshifted compared to the lead halide perovskite $CH_3NH_3PbI_3$, whose band gap is 1.55 eV and greater [60]. Theoretical studies were carried out by Paolo Umari et al. [61] using GW calculations including spin orbit coupling of $CH_3NH_3XI_3$

(X = Pb, Sn) in the tetragonal phase. Their calculations gave band gaps of 1.67 eV and 1.10 eV for $CH_3NH_3PbI_3$ and $CH_3NH_3SnI_3$ respectively. They showed $CH_3NH_3SnI_3$ to be a better candidate for electron transport than $CH_3NH_3PbI_3$. Xujie et al. [62] found experimentally that the lead-free tin halide perovskite $CH_3NH_3SnI_3$ undergoes a pressure-induced phase transition from tetragonal to orthorhombic at 0.7 GPa.

1.5 Aims

The project aims to study the phase stability, electronic structure, and optical properties of some halide perovskites for photovoltiac applications from first-principles applications. All calculations will be performed using the Vienna Ab-initio Simulation Package (VASP) code within the framework of density functional theory. To validate our work, our results are compared with experimental results and other theoretical results obtained previously. Motivated by the facts discussed in Section (1.4), the objectives of this thesis are:

1. To investigate the structural and electronic properties of $CH_3NH_3PbI_3$, $CH_3NH_3SnI_3$ and $CsPbI_3$ within density functional theory.
2. Elastic constants and phonon band structures will be calculated in order to test mechanical and dynamical stabilities.
3. To calculate optical properties of the most stable phases within the many-body perturbation theory BSE level of approximation, such as real and imaginary parts of the dielectric constant, refractive index and absorption coefficient.
4. To calculate the lattice thermal conductivities of the most stable phases within the single-model relaxation-time approximation and linearized phonon Boltzmann equation as implemented in phono3py code.
5. Calculate the electronic transport properties by solving the semiclassical Boltzmann transport equation on top of density functional theory calculations, within the constant relaxation time approximation in order to determine the suitability of the most stable phase for thermoelectric applications.
6. A comparison between hybrid halide and inorganic perovskite will be made by replacing the organic cation with the inorganic cation Cs, to study the effect of the inorganic cation Cs on the lattice thermal conductivity of the compound.

1.6 Structure of this Thesis

The rest of the thesis is organized as follows: In Chapter 2, we present the theoretical methods employed in the calculations, starting from the Schrödinger equation. Different methods to solve the problem will be needed, such as density functional theory (Section 2.4) and many-body perturbation theory (Section 2.5). Then we present an overview of the Boltzmann transport theory followed by transport coefficients (Section 2.6). Details about the computational methods are given in Chapter 3. Chapter 4 includes our results and discussion. Section 4.1 is devoted to the structural, mechanical, electronic, thermoelectric and optical properties of the orthorhombic phase of $CH_3NH_3PbI_3$ perovskite. Then Section 4.2 is dedicated to the structural, mechanical, electronic and optical properties of the orthorhombic phase of $CsPbI_3$ perovskite. Section 4.3 is dedicated to the structural, mechanical, electronic and optical properties of the orthorhombic phase of $CH_3NH_3SnI_3$ perovskite. Finally, Chapter 5 is where all the work is concluded and where directions for future works are given.

2

Theoretical Methods

2.1 Many-Body Problem: The Basic Problem

The description of properties of matter such as structure and dynamics of many-electron systems is one of the basic problems in condensed matter physics, chemistry and computational materials science. These systems comprise single atoms, the most elementary building blocks of ordinary matter, all kinds of molecules, ranging from dimers to proteins, as well as mesoscopic systems [63]. The solid matter consists of a configuration (may be periodic) of atoms in close proximity, the analysis of the electronic structure of matter is done by solving the fundamental Schrödinger equation (for convenience of notation, spin dependence has been suppressed in this section) with the general form

$$\hat{H}\Psi(\mathbf{R}_I;\mathbf{r}_i;t) = i\hbar\frac{\partial}{\partial t}\Psi(\mathbf{R}_I;\mathbf{r}_i;t); \tag{2.1.1}$$

where $\Psi(\mathbf{R}_I;\mathbf{r}_i;t)$ is the wave function of a many-body system which describe the quantum mechanical behaviour of the system, $\mathbf{R}_I$ (I= 1,2,3,...,P) is the position of the I^{th} nucleus, $\mathbf{r}_i$ (i= 1,2,3,...,N) is the position of the i^{th} electron, P are the number of nuclei and N are the number of electrons [64, 65].

To describe the properties of matter from theoretical methods our starting point is the Hamiltonian for the interacting system of N electrons and P nuclei, with the explicit

form:

$$\begin{aligned}\hat{H} = & -\frac{\hbar^2}{2m_e}\sum_{i=1}^{N}\nabla_i^2 - \sum_{I=1}^{P}\sum_{i=1}^{N}\frac{Z_I e^2}{|\mathbf{R}_I - \mathbf{r}_i|} + \frac{1}{2}\sum_{j\neq i}^{N}\sum_{i=1}^{N}\frac{e^2}{|\mathbf{r}_i - \mathbf{r}_j|} - \sum_{I=1}^{N}\frac{\hbar^2}{2M_I}\nabla_I^2 \\ & + \frac{1}{2}\sum_{I=1}^{P}\sum_{J\neq I}^{N}\frac{Z_I Z_J e^2}{|\mathbf{R}_I - \mathbf{R}_J|},\end{aligned} \tag{2.1.2}$$

where $\mathbf{R} = \{\mathbf{R}_I,\, I = 1, ...,P\}$ is a set of P nuclear coordinates, and $\mathbf{r} = \{\mathbf{r}_i,\, i = 1, ...,N\}$ is a set of N electronic coordinates. In general, we denoted electrons by i subscripts, nuclei denoted by I subscripts; Z_I and M_I are the charges and masses of the nuclei respectively; $\hbar$, m and e are the conventional fundamental constants [64, 66, 67]. It then follows in general, the Hamiltonian can be expressed as [66]:

$$\hat{H} = \hat{T}_n + \hat{V}_{nn} + \hat{T}_e + \hat{V}_{en} + \hat{V}_{ee}. \tag{2.1.3}$$

In equation (2.1.3), $\hat{T}_n$ represents the kinetic energy of the N nuclei of the system

$$\hat{T}_n = -\sum_{I=1}^{N}\frac{\hbar^2}{2M_I}\nabla_I^2. \tag{2.1.4}$$

The potential $\hat{V}_{nn}$ represents the repulsion among the nuclei

$$\hat{V}_{nn} = \frac{1}{2}\sum_{I=1}^{P}\sum_{J\neq I}^{P}\frac{Z_I Z_J e^2}{|\mathbf{R}_I - \mathbf{R}_J|}. \tag{2.1.5}$$

The rest terms in equation (2.1.3) are the electronic kinetic energy, the electrons-nuclei interaction energy and the electron-electron interaction energy operators:

$$\begin{aligned}\hat{T}_e &= -\frac{\hbar^2}{2m_e}\sum_{i=1}^{N}\nabla_i^2, \\ \hat{V}_{en} &= -\sum_{I=1}^{P}\sum_{i=1}^{N}\frac{Z_i e^2}{|\mathbf{R}_I - \mathbf{r}_i|}, \\ \hat{V}_{ee} &= \frac{1}{2}\sum_{j\neq i}^{N}\sum_{i=1}^{N}\frac{e^2}{|\mathbf{r}_i - \mathbf{r}_j|}.\end{aligned} \tag{2.1.6}$$

2.2 Born-Oppenheimer Approximation

The motion of any particle in the interacting system is a function of all other particle's motion; therefore the solution of the equation (2.1.1) is very complicated and approximation is required [66, 67]. The most important approximation is the so-called Born-Oppenheimer approximation which the wave function $\Psi(\mathbf{R}_I;\mathbf{r}_i)$ in equation (2.1.1) can be approximated as a product of the form

$$\Psi(\mathbf{R}_I,\mathbf{r}_i)=\Psi_e(\mathbf{R}_I,\mathbf{r}_i)\Psi_n(\mathbf{R}_I), \tag{2.2.1}$$

where $\Psi_e(\mathbf{R}_I,\mathbf{r}_i)$ is the electron wave-function and $\Psi_n(\mathbf{R}_I)$ is the nucleus wave-function. In equation (2.2.1) Born and Oppenheimer assume that the nuclei move much slower than the electrons, so Born and Oppenheimer ignored their motion and considered them as static. Using equation (2.1.1) and equation (2.2.1) [63] we obtain the set of two equations

$$\begin{aligned}\hat{H}_e\Psi_e(\mathbf{R}_I,\mathbf{r}_i)&=[\hat{T}_e+\hat{V}_{ee}+\hat{V}_{en}]\Psi_e(\mathbf{R}_I,\mathbf{r}_i)\\&=E_e\Psi_e(\mathbf{R}_I,\mathbf{r}_i),\end{aligned} \tag{2.2.2}$$

and the Hamiltonian for the nuclei has the form

$$\begin{aligned}\hat{H}_n\Psi_n(\mathbf{R}_I)&=[\hat{T}_n+\hat{V}_{nn}+E_e]\Psi_n(\mathbf{R}_I)\\&=E_n\Psi_n(\mathbf{R}_I).\end{aligned} \tag{2.2.3}$$

Therefore, the electronic Hamiltonian reduces to [68].

$$\hat{H}_e=\hat{T}+\hat{V}_{\mathrm{ee}}+\hat{V}_{\mathrm{en}}. \tag{2.2.4}$$

The time-dependent Schrödinger equation for the nuclear wave function is given by

$$i\hbar\frac{\partial}{\partial t}\Psi_q(\mathbf{R};t)=\left(-\sum_I\frac{\hbar^2}{2M_I}\nabla_I^2+V_{\mathrm{nn}}(\mathbf{R})+\tilde{V}_q(\mathbf{R})\right)\Psi_q(\mathbf{R};t), \tag{2.2.5}$$

with

$$\tilde{V}_q(\mathbf{R})=E_q(\mathbf{R})+\sum_I\frac{\hbar^2}{2M_I}\left\langle\Psi_q|\nabla_I^2|\Psi_q\right\rangle. \tag{2.2.6}$$

The last term in equation (2.2.6) is the diagonal correction to the energy levels due to the remaining coupling between the nuclear and the electronic degrees of freedom, this term is found to be proportional to m_e/M. The negligence of the diagonal term ,

known as Born-Oppenheimer approximation, therefore, the time-dependent Schrödinger equation for the nuclear system takes the form [64]

$$i\hbar\frac{\partial}{\partial t}\Psi_q(\mathbf{R};t) = \Big(-\sum_I \frac{\hbar^2}{2M_I}\nabla_I^2 + V_{\rm nn}(\mathbf{R}) + E_q(\mathbf{R})\Big)\Psi_q(\mathbf{R};t). \tag{2.2.7}$$

The dynamics of the mean values of position and momentum operators can be obtained by Ehrenfest's theorem [69]

$$\frac{d}{dt}\langle\mathbf{R}\rangle = \frac{1}{i\hbar}\langle\mathbf{R},\hat{H}\rangle + \langle\frac{\partial\mathbf{R}}{\partial t}\rangle = \frac{1}{M}\langle\hat{P}\rangle\,, \tag{2.2.8}$$

and

$$\frac{d}{dt}\langle\hat{P}\rangle = \frac{1}{i\hbar}\langle\hat{P},\hat{H}\rangle + \langle\frac{\partial\hat{P}}{\partial t}\rangle = \frac{1}{M}\langle-\nabla\hat{V}\rangle\,; \tag{2.2.9}$$

where $\hat{P}$ is the momentum and $\hat{V}$ is the potential of the Hamiltonian $\hat{H}$. Combining equations (2.2.8) and (2.2.9) give rise to the Newtonian equation of motion for the position mean value $\langle\mathbf{R}\rangle$

$$M\frac{d^2}{dt^2}\langle\mathbf{R}\rangle = \langle-\nabla\hat{V}\rangle\,. \tag{2.2.10}$$

Now, if we apply the classical nuclei approximation to the Born-Oppenheimer nuclear system (2.2.7), we get

$$M\frac{d^2}{dt^2}\mathbf{R} = -\nabla\hat{V} = -\nabla\Big[V_{\rm nn}(\mathbf{R}) + E_q(\mathbf{R})\Big], \tag{2.2.11}$$

where $E_q(\mathbf{R})$ is the $q^{\rm th}$ called *adiabatic potential energy surface*.

The Hellman-Feynman force theorem [70, 71, 72] relates the variation of the electronic energy with respect to an external parameter λ, to the expectation value of the derivative of the Hamiltonian with respect to the same parameter λ

$$\frac{\partial E_q(\lambda)}{\partial\lambda} = \langle\Psi_q(\mathbf{R})|\frac{\partial\hat{H}}{\partial\lambda}|\Psi_q(\mathbf{R})\rangle\,. \tag{2.2.12}$$

From equation (2.2.11), for $\lambda = \mathbf{R}_I$, i.e. considering the $I^{\rm th}$ nucleus, so the force on the nucleus I is

$$M\frac{d^2}{dt^2}\mathbf{R} = -\langle\Psi_q(\mathbf{R})|\frac{\partial\hat{H}}{\partial\mathbf{R}_I}|\Psi_q(\mathbf{R})\rangle - \langle\frac{\partial V_{\rm nn}}{\partial\mathbf{R}}\rangle\,. \tag{2.2.13}$$

The numerical integration of the above Newtonian equation of motion receives the name of first-principles or ab-initio molecular dynamics [66, 64]. The ground-state atomic

geometrical structure of a solid is found by the solution of the stationary problem i.e, $M\frac{d^2}{dt^2}\mathbf{R} = 0$

$$\langle\Psi_q(\mathbf{R})|\frac{\partial\hat{H}}{\partial\mathbf{R}_I}|\Psi_q(\mathbf{R})\rangle + \langle\frac{\partial V_{\rm nn}}{\partial\mathbf{R}}\rangle = 0 \tag{2.2.14}$$

and the procedure is known as geometry optimization [64].

2.3 Electronic Density

The many-body wave function of N electrons is written as

$$\Psi(\mathbf{r}\sigma) = \Psi(\mathbf{r}_1\sigma_1, \mathbf{r}_2\sigma_2, ..., \mathbf{r}_N\sigma_N), \tag{2.3.1}$$

Where $\mathbf{r}_i$ and σ_i are the position and the spin of the i^{th} electron, respectively. The many-body wave function must satisfies the following two conditions [66, 68, 73]

First, the wave function must be normalized

$$\langle\Psi|\Psi\rangle = \sum_{\sigma_1...\sigma_N}\int d\mathbf{r}_1\int d\mathbf{r}_2...\int d\mathbf{r}_N|\Psi(\mathbf{r}_1\sigma_1, \mathbf{r}_2\sigma_2, ..., \mathbf{r}_N\sigma_N)|^2 = 1. \tag{2.3.2}$$

Second, because electrons are fermions, the wave function must be antisymmetric under exchange of two electron labels i and j

$$\begin{aligned}\Psi(\mathbf{r}_1\sigma_1, ..., \mathbf{r}_i\sigma_i, .., \mathbf{r}_j\sigma_j, ..., \mathbf{r}_N\sigma_N) = \\ - \Psi(\mathbf{r}_1\sigma_1, ..., \mathbf{r}_j\sigma_j, .., \mathbf{r}_i\sigma_i, ..., \mathbf{r}_N\sigma_N).\end{aligned} \tag{2.3.3}$$

The electronic density $n_\sigma(\mathbf{r})$ for a given state is defined as the number of electrons per unit volume at the point $\mathbf{r}$ for that state. The total number of electrons is given by

$$\sum_\sigma\int n_\sigma(\mathbf{r})d\mathbf{r} = N. \tag{2.3.4}$$

To find $n_\sigma(\mathbf{r})d\mathbf{r}$, one can calculate the probability of finding electrons of spin σ at $\mathbf{r}$.

Since $|\Psi>$ are normalized, we get

$$n(\mathbf{r},\sigma) = N \sum_{\sigma_j=\sigma_2}^{\sigma_N} \int d\mathbf{r}_2 \int d\mathbf{r}_3 ... \int d\mathbf{r}_N |\Psi(\mathbf{r}\sigma, \mathbf{r}_2\sigma_2, \mathbf{r}_3\sigma_3, ..., \mathbf{r}_N\sigma_N)|^2, \tag{2.3.5}$$

with the density operator

$$\hat{n}(\mathbf{r},\sigma) = \sum_{i=1}^{N} \delta(\mathbf{r}_i - \mathbf{r})\delta(\sigma_i - \sigma). \tag{2.3.6}$$

2.4 Density Functional Theory (DFT)

Density functional theory is a mathematical tool for solving problems in many-body systems based on two theorems made by Hohenberg and Kohn (1964) as well as Kohn Sham (1965) [74, 75]. In this section we introduce the density functional theory concept and some of its approximations. We will start with the Hohenberg and Kohn (HK) theorem.

2.4.1 The Hohenberg-Kohn Theorems

The first theorem states that '*the external potential* $V_{\text{ext}}(\mathbf{r})$ *is (up to an arbitrary constant) a unique functional of* $n(\mathbf{r})$; *since, in turn* $V_{\text{ext}}(\mathbf{r})$ *fixes* $\hat{H}$ *we see that the full many particle ground state is a unique functional of* $n(\mathbf{r})$' [68].

Here, we assumed that $V_{\text{ext}}(\mathbf{r})$ and $V'_{\text{ext}}(\mathbf{r})$ are different external potential, but give the same ground state density $n_0(r)$. From the variational principle (cf. Ref. [65]), it follows that

$$\begin{aligned} E_0 < \langle \Psi' | \hat{H} | \Psi' \rangle &= E'_0 + \langle \Psi' | V_{\text{ext}} - V'_{\text{ext}} | \Psi' \rangle \\ &= E'_0 + \int n_0(\mathbf{r})[V_{\text{ext}} - V'_{\text{ext}}]d\mathbf{r}, \end{aligned} \tag{2.4.1}$$

and

$$\begin{aligned} E'_0 < \langle \Psi | \hat{H} | \Psi \rangle &= E_0 - \langle \Psi | V_{\text{ext}} - V'_{ext} | \Psi \rangle \\ &= E_0 - \int n_0(\mathbf{r})[V_{\text{ext}} - V'_{\text{ext}}]d\mathbf{r}. \end{aligned} \tag{2.4.2}$$

Adding equations (2.4.1) and (2.4.2), this leaves us with the clear contradiction

$$(E_0 + E_0^{'}) < (E_0 + E_0^{'}). \tag{2.4.3}$$

Therefore there cannot be two different external potential $V_{\text{ext}}(\mathbf{r})$ that gives the same ground state density, i.e. the ground state density uniquely specifies the external potential $V_{ext}(\mathbf{r})$. **The second theorem** states that '*a universal function* $F_{\text{HK}}[n]$ *of the energy* $E[n]$, *the functional that delivers the ground state energy of the system, delivers the lowest energy if and only if the input density is the true ground density* $E[n]$*'* [68].

Using the electronic Hamiltonian in equation (2.2.4), we can define the HK energy functional as

$$E[n] = \langle \Psi[n] | \hat{H} | \Psi[n] \rangle = \langle \Psi[n] | \hat{T} + \hat{V}_{\text{ee}} | \Psi[n] \rangle + V_{\text{ext}}[n], \tag{2.4.4}$$

and from the variational principle

$$E[n] < (F[n] + V_{\text{ext}}[n]) = F[n] + \int n(\mathbf{r}) V_{\text{ext}}(\mathbf{r}) d\mathbf{r} = E_0[n_0(\mathbf{r})]. \tag{2.4.5}$$

Since the kinetic energy $\hat{T}$ and the electron-electron interaction terms are functional of the density only. So $F[n]$ must be a universal functional of the density, and depends only on the electron density

$$F[n] = \langle \Psi[n] | \hat{T} + \hat{V}_{\text{ee}} | \Psi[n] \rangle \,. \tag{2.4.6}$$

From the variational principle we can derive that this functional acquires its minimum for the correct density $n(\mathbf{r})$ corresponding to $V_{\text{ext}}(\mathbf{r})$, since for a given $V_{\text{ext}}(\mathbf{r})$ and any density $n^{'}(\mathbf{r})$ we have

$$E[n^{'}(\mathbf{r})] < \langle \Psi^{'} | \hat{H} | \Psi^{'} \rangle = F[n^{'}(\mathbf{r})] + \int V_{\text{ext}}(\mathbf{r}) n^{'}(\mathbf{r}) d\mathbf{r} > \langle \Psi | \hat{H} | \Psi \rangle = E[n(\mathbf{r})]. \tag{2.4.7}$$

The Hohenberg and Kohn (HK) two theorems form the mathematical basis of density functional theory; so knowledge of $F[n]$ means the knowledge of the solution of the full many-body Schrödinger equation [64, 68, 74, 76].

2.4.2 Constrained Search Formulation

From the variational principle, the contradiction in equation (2.4.3) is true only for non-degenerate ground state system [76], Levy and Lieb [77], extend the Hohenberg and Kohn (HK) second theorem to degenerate ground state by a weaker constraint, which is some respects simpler and more constructive. The ground state energy can be found by minimizing $<\Psi|\hat{H}|\Psi>$ over all antisymmetric wave functions for N-particle

$$E_0[n] = \min_{\Psi\to N} <\Psi|\hat{H}|\Psi> . \tag{2.4.8}$$

The equation above can be minimized into two procedures. First step we think about all wave functions Ψ which capitulate a given density $n(\mathbf{r})$, and minimize over those wave functions

$$E_0[n] = \min_{\Psi\to N} <\Psi|\hat{H}|\Psi> = \min_{\Psi\to N} <\Psi|\hat{T}+\hat{V}_{\mathrm{ee}}|\Psi> + \int d\mathbf{r} v_{\mathrm{ext}}(\mathbf{r})n(\mathbf{r}). \tag{2.4.9}$$

Then we define the Levy- Lieb universal functional

$$F[n] = \min_{\Psi\to N} <\Psi|\hat{T}+\hat{V}_{\mathrm{ee}}|\Psi>, \tag{2.4.10}$$

this functional is defined for all wave functions that yield the input density $n(\mathbf{r})$. Second step the ground state energy is then found by minimizing over all N-electron densities $n(\mathbf{r})$ we get

$$E_0[n] = \min_{n}[\min_{\Psi\to N} <\Psi|\hat{T}+\hat{V}_{\mathrm{ee}}|\Psi> + \int d\mathbf{r} v_{\mathrm{ext}}(\mathbf{r})n(\mathbf{r})], \tag{2.4.11}$$

where during the minimization $v_{\mathrm{ext}}(\mathbf{r})$ is fixed, introducing the universal functional, this results in

$$E_0[n] = \min_{n}\big(F[n] + \int d\mathbf{r} v_{\mathrm{ext}}(\mathbf{r})n(\mathbf{r})\big). \tag{2.4.12}$$

We notice that $F[n]$ differs from the universal functional $F_{\mathrm{HK}}[n]$ only by the fact it is define for all densities that originate from an antisymmetric wave function [68].

2.4.3 The Kohn-Sham (KS) Equations

The Kohn-Sham ansatz rests on two assumptions. First, the exact ground state density can be represented by the ground state density of the auxiliary system (called the reference system) of non-interacting particles. Second, the auxiliary Hamiltonian is

chosen to have the usual kinetic operator and an effective local potential $v_s(\mathbf{r})$ acting on an electron of spin σ at point $\mathbf{r}$ [64, 66].

$$\hat{H}_{\text{aux}} = \sum_i \Big[-\frac{\hbar^2}{2m_e}\nabla_i^2 + v_s(\mathbf{r}_i)\Big]. \tag{2.4.13}$$

We can easily determine the ground state density by solving the following Schrödinger equation for single particle

$$\hat{H}\Psi_i = \varepsilon_i \Psi_i \tag{2.4.14}$$

$$[-\frac{\hbar^2}{2m_e}\nabla^2_{(\mathbf{r})} + v_s(\mathbf{r})]\Psi_i = \varepsilon_i^{\text{KS}}\Psi_i. \tag{2.4.15}$$

In the Kohn-Sham approach, the KS total energy for the interacting system can be written as

$$E_{\text{KS}} = T_s[n] + \int d\mathbf{r} v_{\text{ext}}(\mathbf{r}) d\mathbf{r} + E_{\text{H}}[n] + E_{\text{xc}}[n], \tag{2.4.16}$$

where $T_s[n]$ is the kinetic energy of the non-interacting electrons, $E_{\text{H}}[n]$ is the Hartree energy and $E_{\text{xc}}[n]$ is the *exchange-correlation energy* functional [66, 64, 76].

$$E_{\text{xc}}[n] = \langle \hat{T} \rangle - T_s[n] + \langle V_{\text{int}} \rangle - E_{\text{H}}[n], \tag{2.4.17}$$

where the exchange-correlation energy E_{xc} is the functional which contains every things that we can not handle with, thus must be approximated.

All terms in Kohn-Sham energy functional can be written in their explicit form except $E_{\text{xc}}[n]$ which has no explicit form [68]. Applying the variational principle, and taking the orbitals Ψ_i to be orthonormal $\langle \Psi_i | \Psi_j \rangle = \delta_{ij}$, then Kohn-Sham equation take the form

$$\{-\frac{\hbar^2}{2m_e}\nabla^2_{(\mathbf{r})} + \int \frac{n(\mathbf{r}')}{|\mathbf{r}-\mathbf{r}'|} d\mathbf{r}' + v_{\text{xc}}[n] + v_{\text{ext}}(\mathbf{r})\}\Psi_i(\mathbf{r}) = \varepsilon_i^{\text{KS}}\Psi_i(\mathbf{r}), \tag{2.4.18}$$

or

$$\{-\frac{\hbar^2}{2m_e}\nabla^2_{(\mathbf{r})} + V_{\text{KS}}(\mathbf{r})\}\Psi_i(\mathbf{r}) = \varepsilon_i^{\text{KS}}\Psi_i(\mathbf{r}), \tag{2.4.19}$$

where

$$V_{\text{KS}}(\mathbf{r}) = \int \frac{n(\mathbf{r}')}{|\mathbf{r}-\mathbf{r}'|} d\mathbf{r}' + v[n] + v_{\text{ext}}(\mathbf{r}), \tag{2.4.20}$$

with the exchange correlation functional v_{xc} which is defined as the functional derivative

of $E_{\rm xc}[n]$ with respect to $n(\mathbf{r})$ [66, 68, 76]

$$v_{\rm xc}(\mathbf{r}) = \frac{\partial E_{\rm xc}[n]}{\partial n(\mathbf{r})}. \tag{2.4.21}$$

The Kohn-Sham equations determine exactly the energy of the ground state density of many-body system, and must be solved self-consistently. One begin with a guessed density $n(\mathbf{r})$, to construct $V_{\rm KS}(\mathbf{r})$ until self-consistency is achieved [76].

2.4.4 Spin-orbit Coupling (SOC)

In a non-relativistic description, the Kohn-Sham approach (discussed in Sub-section 2.4.3) based on the electronic Hamiltonian in equation (2.2.4), where the spin-orbit coupling is negligible. However, number of applications where additional terms are needed in the Hamiltonian, such as spin-orbit coupling. The spin-orbit coupling is important, especially for core electrons of heavy metals. The spin-orbit interaction term $\hat{H}_{LS}$ of a many-body system is written as [78]

$$\hat{H}_{LS} = \sum_{i=1} \xi(r_i) L_i.S_i, \tag{2.4.22}$$

where L_i and S_i are the orbital and spin angular momenta, of the $i^{\rm th}$ electron, respectively, while $\xi(r_i)$ is a prefactor related to the derivative of the potential of the electron i. Therefore, to take the SOC into account the electronic Hamiltonian in equation (2.2.4) tales the form

$$\hat{H}_e = \hat{T} + \hat{V}_{\rm ee} + \hat{V}_{\rm en} + \hat{H}_{LS}. \tag{2.4.23}$$

2.4.5 Solving Kohn-Sham Equations

Plane Wave Basis

Bloch's theorem (cf. Ref. [79]) states that the electronic wave function of a periodic system can be expressed as a product of a plane wave $e^{i\mathbf{k}.\mathbf{r}}$ and a lattice periodic function $u_{\mathbf{k}}(\mathbf{r})$ ($\mathbf{k}$ denoting a wave vector within first Brillouin zone)

$$\Psi_{\mathbf{k}}(\mathbf{r}) = e^{i\mathbf{k}.\mathbf{r}} u_{\mathbf{k}}(\mathbf{r}). \tag{2.4.24}$$

The lattice periodic function, is invariant under translation by a lattice vector $\mathbf{R}$

$$u_{\mathbf{k}}(\mathbf{r}+\mathbf{R}) = u_{\mathbf{k}}(\mathbf{r}). \tag{2.4.25}$$

As $u_{\mathbf{k}}(\mathbf{r})$ is a periodic function, it can be expressed in term of a Fourier series as follows

$$u_{\mathbf{k}}(\mathbf{r}) = \sum_{\mathbf{G}} c_{\mathbf{G},\mathbf{k}} e^{i\mathbf{G}.\mathbf{r}}, \tag{2.4.26}$$

where $\mathbf{G}$ is a reciprocal lattice vector defined as $\mathbf{G}.\mathbf{b}= 2\pi m$, $\mathbf{b}$ is the translational vector of the crystal lattice and m is an arbitrary integer. Then, the KS orbitals are expanded in the following

$$\Psi_{\mathbf{k}}(\mathbf{r}) = \sum_{\mathbf{k},\mathbf{G}} c_{\mathbf{k},\mathbf{G}} e^{i(\mathbf{k}+\mathbf{G}).\mathbf{r}}. \tag{2.4.27}$$

Inserting the plane wave expression (2.4.27) into the Kohn-Sham equations (2.4.19), one obtain a secular equation

$$\sum_{\mathbf{G}} \left[\frac{\hbar}{2m} |\mathbf{k}+\mathbf{G}| \delta_{\mathbf{G}\mathbf{G}'} + V^{\sigma}_{\mathrm{KS}}(\mathbf{G}\text{-}\mathbf{G}') \right] c_{i,\mathbf{k}+\mathbf{G}'} = \varepsilon_i c_{i,\mathbf{k}+\mathbf{G}'}, \tag{2.4.28}$$

where $V^{\sigma}_{\mathrm{KS}}(\mathbf{G}\text{-}\mathbf{G}')$ is the Fourier transform of the Kohn-Sham potential. The accuracy of the calculation is set by fixing the plane wave energy cut-off $\mathrm{E_{cut}}$:

$$\frac{1}{2}|\mathbf{k}+\mathbf{G}|^2 < E_{\mathrm{cut}}. \tag{2.4.29}$$

k-Space and Brillouin-Zone

From equation (2.4.24), it is clear that there is a particular class of vectors $\mathbf{k}$ such that the phase factor $e^{i\mathbf{k}.\mathbf{r}} = 1$, and thus the wave function is in phase with the periodicity of the unite cell. The group of the three smallest independent such vectors is such enough to determine all the reciprocal lattice vectors, in the same way as with the primitive vectors in real space [64].

In the reciprocal space, the Wigner-Seitz cell, is known as the first Brillouin zone, and sometimes simply the Brillouin zone, for short. Its volume Ω_{R} is given by [64]

$$\Omega_{\mathrm{R}} = \mathbf{b}_i \cdot \mathbf{b}_j \times \mathbf{b}_k = \frac{(2\pi)^3}{\Omega}, \tag{2.4.30}$$

where Ω is the volume of the unit cell. There are many ways of sampling the Brillouin zone, the most common one used in this work is the Monkhorst-Panck grid which is a uniform grid [80].

Pseudopotentials

Electrons in solids are divided in valence electrons and inner core electrons. It is well known that the physical properties of solids depends on the valence electron more than the core electrons. The pseudopotentials takes this advantage by replacing the core electrons and the strong ionic potential by a weaker pseudopotential [81, 82]. The pseudopotential acts on a set of pseudo wave functions in place of the true valence wave function [82].

There are several pseudopotentials one can construct from first-principles such as norm-conserving pseudopotentials [83], ultra-soft pseudopotentials [84] or the potentials based on the projector augmented wave (PAW) method [85]. In this subsection, we demonstrate only the main principle of the pseudopotential concept.

Consider $|\Psi_c\rangle$ and $|\Psi_v\rangle$ to be the exact solutions of the Schrödinger equation for the inner core (c) electrons and those for the valence (v) electrons

$$\hat{H}\,|\Psi_n\rangle = E_n\,|\Psi_n\rangle\,, \tag{2.4.31}$$

where $n = c, v$. The valence wave functions oscillate rapidly in the region occupied by the core electrons due to the strong ionic potential in this region. These oscillations maintain the orthogonality between the core wave functions and the valence wave functions. Therefore, the valence orbitals can be written as a sum of smooth function, $|\Psi_v\rangle$, with an oscillating function due to this orthogonality.

$$|\Psi_v\rangle = |\varphi_v\rangle + \sum_c \alpha_{cv}\,|\Psi_c\rangle\,, \tag{2.4.32}$$

where $\alpha_{cv} = -\langle\Psi_c|\varphi_v\rangle$. For the smooth orbital the Schrödinger equation reads

$$\hat{H}\,|\varphi_v\rangle = E_v\,|\varphi_v\rangle + \sum_c (E_c - E_v)\,|\Psi_c\rangle\,\langle\Psi_c|\varphi_v\rangle\,. \tag{2.4.33}$$

The equation (2.4.33) indicates that $|\varphi_v\rangle$ satisfy Schrödinger-like equation with an en-

ergy dependent-Hamiltonian

$$\hat{H}^{\mathrm{PK}}(E) = \hat{H} - \sum_c (E_c - E) \left|\Psi_c\right\rangle \left\langle\Psi_c\right| . \tag{2.4.34}$$

Then we can identify

$$\hat{\omega}^{\mathrm{PK}}(E) = \hat{v} - \sum_c (E_c - E) \left|\Psi_c\right\rangle \left\langle\Psi_c\right| , \tag{2.4.35}$$

where $\hat{\omega}^{\mathrm{PK}}(E)$ is the pseudopotential, $\hat{v}$ stand for the true potential and the second term represents the repulsive potential which makes the pseudopotential much weaker than the true potential near the core. For more details, we refer to the literature [83, 84, 85, 86, 87, 88].

Exchange and Correlation Functionals

The most important quantity in the KS approach is the so-called exchange-correlation energy which is expressed as a function of the density $E_{\mathrm{xc}}[n]$, the exact explicit form of E_{xc} is unknown, so it must be approximated [66]. The first four rungs on Jacobs ladder [89, 90, 91] are (I) the local density approximation (LDA), (II) the generalized gradient approximation (GGA)and (III) the meta-GGA, and (IV) hybrid functionals. In this section we present, the generalized gradient approximation (GGA) [92, 93], the hybrid functionals (HSE06) [94] and the modified Becke Johnson potential (MBJ) [95].

Generalized Gradient Approximation (GGA)

The local density approximation (LDA) (cf. Ref. [96]) assumes that the density is the same every-where, so it does not give a good approximation when the density increased such as in molecule. To improve over local density approximation it is relevant to make the functional depend on the density and the gradient of the density $\nabla n(\mathbf{r})$, in order to account for non-homogeneity of the true electron density, that is the generalized gradient approximation (GGA) in which the exchange correlation functional takes the

form [66, 68, 92]

$$E_{\rm xc}^{\rm GGA}[n_\uparrow, n_\downarrow] = \int d\mathbf{r} n(\mathbf{r}) \epsilon_{\rm xc}(n_\uparrow, n_\downarrow, |\nabla n_\uparrow|, |\nabla n_\downarrow|, ...) \quad (2.4.36)$$

$$\equiv \int d\mathbf{r} n(\mathbf{r}) \epsilon_{\rm xc}^{\rm unif}(n(\mathbf{r})) F_{\rm xc}(n_\uparrow, n_\downarrow, |\nabla n_\uparrow|, |\nabla n_\downarrow|, ...), \quad (2.4.37)$$

where $F_{\rm xc}$ is dimensionless and $\epsilon_{\rm xc}^{\rm unif}(n(\mathbf{r}))$ is the exchange energy of the unpolarized uniform electron gas, ∇ terms refer to the gradient terms of the electron density [66]. The exchange correlation potential of GGA is given by

$$V_{\rm xc}^{\rm GGA} = \frac{\partial E_{xc}^{\rm GGA}}{\partial n(\mathbf{r})} = \left[\epsilon_{\rm xc} + n \frac{\epsilon_{\rm xc}}{n(\mathbf{r})} - \nabla (n \frac{\epsilon_{\rm xc}}{n(\mathbf{r})}) \right]_{\mathbf{r}}. \quad (2.4.38)$$

The most popular generalized gradient approximation functionals are Perdew-Burke-Ernzerhof (PBE) functional and revised PBE functional (PBEsol) that improves predictions of equilibrium properties of solids. We have used in our calculations the Perdew-Burke-Ernzerhof (PBE) [92] and revised functional PBEsol [93]

Meta-GGA

The meta-GGA functional includes the kinetic energy density in the expression of the exchange-correlation which is related to the second derivative of the density $\nabla^2 n(\mathbf{r})$. The exchange-correlation takes the form

$$E_{\rm xc}[n_\uparrow, n_\downarrow] = \int d\mathbf{r} n(\mathbf{r}) \epsilon_{\rm xc}(n_\uparrow, n_\downarrow, |\nabla n_\uparrow|, |\nabla n_\downarrow|, |\tau_\uparrow|, |\tau_\downarrow|), \quad (2.4.39)$$

where $n(\mathbf{r}) = n_\uparrow(\mathbf{r}) + n_\downarrow(\mathbf{r})$ is the total density, $\tau_\uparrow$ and $\tau_\downarrow$ are the Kohn-Sham orbital kinetic energy densities and

$$\tau_\sigma(\mathbf{r}) = \sum_i^{\rm occup} \frac{1}{2} |\varphi_{i\sigma}(\mathbf{r})|^2 \quad (2.4.40)$$

is the KS orbital $\varphi_{i\sigma}(\mathbf{r})$ kinetic energy density of electrons with spin σ [97].

Available meta-GGA flavours include: M06L [98], TPSS [97] and modified Becke Johnson potential (MBJ) [95]. MBJ is known to predict electronic properties at an accuracy comparable to GW method and hybrid functional. We will be using the MBJ in chapter 4 to calculate the band gap of the perovskite ($CH_3NH_3SnI_3$).

Hybrid Functionals

The Hartree-Fock (HF) approximation (see appendix A) provides a good description of single atoms and ions, however, the HF theory is limited to atomic systems, because correlation effects, which are not included in the HF approximation, are important in large molecules and solids. As these correlation effects are captured well within the local exchange-correlation functional. Hybrid functionals are a class of exchange-correlation functionals in DFT that are constructed by a suitable mixing of LDA/GGA exchange-correlation functionals with a certain portion of the exact HF exchange [99]. A.D. Becke [99, 100] mixture of local exchange-correlation functionals with HF exchange using the adiabatic connection (transform the non-interacting system to the physical interacting one)

$$E_{\mathrm{xc}}[n] = \int_0^1 u_{\mathrm{xc}}^{\lambda} d\lambda, \tag{2.4.41}$$

where λ is an inter-electronic coupling strength parameter, and $u_{\mathrm{xc}}^{\lambda}$ is the potential energy of exchange correlation at intermediate coupling λ. At $\lambda = 0$ the energy is the HF exchange energy, and for a fully interacting real system $\lambda = 1$. Solving the integral in equation (2.4.41) within this approximation leading the half-and-half form [66].

$$E_{\mathrm{xc}} = \frac{1}{2}(E_{\mathrm{x}}^{\mathrm{HF}} + E_{\mathrm{xc}}^{\mathrm{LDA}}). \tag{2.4.42}$$

The most popular hybird functional used in molecular calculations is the B3LYP functional [100, 101]

$$E_{\mathrm{xc}}^{\mathrm{B3LYP}} = E_{\mathrm{xc}}^{\mathrm{LDA}} + a_0(E_{\mathrm{x}}^{\mathrm{HF}} - E_{\mathrm{x}}^{\mathrm{LDA}}) + a_{\mathrm{x}}(E_{\mathrm{x}}^{\mathrm{GGA}} - E_{\mathrm{x}}^{\mathrm{LDA}}) + a_{\mathrm{c}}(E_{\mathrm{c}}^{\mathrm{GGA}} - E_{\mathrm{c}}^{\mathrm{LDA}}). \tag{2.4.43}$$

The mixing parameters a_0, a_{x} and a_{c} have been determined by fit against set of molecules experimental data. The PBE0 functional [102] which derived from PBE functional is described as

$$E_{\mathrm{xc}}^{\mathrm{PBE0}} = E_{\mathrm{xc}}^{\mathrm{PBE}} + \frac{1}{4}(E_{\mathrm{x}}^{\mathrm{HF}} - E_{\mathrm{x}}^{\mathrm{PBE}}). \tag{2.4.44}$$

In order to improve computational efficiency, the Heyd-Scuseria-Ernzerhof (HSE) exchange-correlation functional [103] uses an error function to split the Coulomb operator into short-range (sr) and long-range (lr) ($\frac{1}{r} = S_\omega(r) + L_\omega(r)$)

$$E_{xc}^{\mathrm{HSE}} = \alpha E_{\mathrm{x}}^{\mathrm{HF,sr}}(\mu) + (1-\alpha)E_{\mathrm{x}}^{\mathrm{PBE,sr}}(\mu) + \alpha E_{\mathrm{x}}^{\mathrm{PBE,lr}}(\mu) + E_{\mathrm{c}}^{\mathrm{PBE}}, \tag{2.4.45}$$

where α is the mixing factor and it control the exact $E_{\mathrm{x}}^{\mathrm{HF}}$ include in to the hybrid functional and μ is the screening parameter that controls the range separation.

2.5 Many Body Perturbation Theory (MBPT)

The properties of matter fall into two categories determined by the electronic ground state and electronic excited states. This distinction is evident in the physical properties of materials and also determines the framework for theoretical understanding and development of the entire field of electronic structure [66].

The Kohn-Sham (KS) density functional theory approach, provides good results for the ground state properties of many solids. However, a well known failure of DFT is that it does not describe the excited states (adding or removing energy) accurately [104], specially, DFT breaks down when used to calculate band gaps of insulators or semiconductors, which are often underestimated. This failure of DFT is linked to the fact that KS eigenvalues ϵ_i^{KS} and eigenstates Ψ_i do not have physical meanings. In order to obtain physical meaningful band gaps, a successful approach is to go beyond DFT using KS eigenstates as basis for many-body perturbation theory (MBPT) calculations. The approach is based on the concept of the so-called quasi-particle, Green function and the self-energy [105].

2.5.1 Quasi-Particle (QP)

Band gaps are experimentally measured by photo-electron spectroscopy. The direct photo-electron is described when a photon arrives with an energy $\hbar\omega$ and ejects an electron and the kinetic energy E_{kin} of the ejected electron is measured. The binding energy of this electron is given by the difference $E_i = E_{\mathrm{kin}} - \hbar\omega$. In reality the electrons are correlated though the Coulomb interaction, and the ejection of an electron is a many-body process. Therefore the motion of one electron depends on the motion of all other electrons $(N-1)$. Inverse photo-electron spectroscopy is the corresponding process where the number of electrons in the system increases from N to $N+1$. In the case of electron injection into a sample, the repulsive Coulomb interaction creates a Coulomb hole around the additional electron. Similarly, if an electron leaves the system, its Coulomb hole also vanishes. Relative to the ground-state N-electron system, the addition (removal) of an electron in indirect (direct) photo-electron spectroscopy

hence creates (annihilates) an ensemble consisting of the bare electron and its oppositely charged Coulomb hole. This ensemble behaves in many ways like a single-particle and is thus called quasi-particle [106]. The difference between the quasi-particle and a bare particle is usually described by the self- energy Σ, which must account for all exchange and correlation effects beyond the Hartree approximation. The full one-particle Green's function cannot be calculated exactly, and therefore one need to employ some approximations. Defining a non-interacting one-particle Greens function $G_o(\mathbf{r}, \mathbf{r}^{'}; E)$ for a system where the exchange and correlation effects are turned off leaving only the Hartree term, the interacting one-particle Green's function $G(\mathbf{r}, \mathbf{r}^{'}; E)$ is linked to $G_o(\mathbf{r}, \mathbf{r}^{'}; E)$ via Dyson's equation [107], recall equation (B.0.4)

$$G(\mathbf{r}, \mathbf{r}^{'}; E) = G_o(\mathbf{r}, \mathbf{r}^{'}; E) + \int \int G_o(\mathbf{r}, \mathbf{r}_1; E)\Sigma(\mathbf{r}_1, \mathbf{r}_2; E)G(\mathbf{r}_2, \mathbf{r}^{'}; E)d\mathbf{r}_1 d\mathbf{r}_2, \tag{2.5.1}$$

In the QP approximation, one-particle Green's function can be represented by QP energies

$$G_o(\mathbf{r}, \mathbf{r}^{'}; E) = \sum_n \frac{\Psi_n^{\mathrm{QP}}(\mathbf{r})\Psi_n^{\mathrm{QP}*}(\mathbf{r}^{'})}{E - E_n}, \tag{2.5.2}$$

Fourier transforming equation (B.0.7) to the energy space and inserting equation (2.5.2), one obtained the QP equation

$$\begin{aligned} &\left[-\frac{\hbar}{2m}\nabla^2(\mathbf{r}) + \int \frac{n(\mathbf{r}^{'})}{|\mathbf{r} - \mathbf{r}^{'}|}d\mathbf{r}^{'} + v_{\mathrm{ext}}(\mathbf{r}) \right] \Psi_i^{\mathrm{QP}}(\mathbf{r}) \\ &+ \int \Sigma(\mathbf{r}, \mathbf{r}^{'}; E_i^{\mathrm{QP}})\Psi_i^{\mathrm{QP}}(\mathbf{r}^{'})d\mathbf{r}^{'} = E_i^{\mathrm{QP}}\Psi_i^{QP}(\mathbf{r}^{'}), \end{aligned} \tag{2.5.3}$$

where $\Sigma(\mathbf{r}, \mathbf{r}^{'}; E_i^{\mathrm{QP}})$ is the self energy, $\int \frac{n(\mathbf{r}^{'})}{|\mathbf{r}-\mathbf{r}^{'}|}d\mathbf{r}^{'}$ is the Hartree potential of electrons, n is the electron density, v_{ext} is the external potential from ions, E_i^{QP} and Ψ_i^{QP} are the quasi-particle eigenvalues and eigenstates, respectively [104].

In the non-self-consistent GW approximation G_0W_0, used through this thesis, G_0 and W_0 are calculated using KS eigenvalues ϵ_i^{KS} and eigenstates Ψ_i [108]. By approximating the eigenstates of the quasi-particle equation (2.5.3) by KS eigenstates Ψ_i, the eigenvalues E_i^{QP} can be calculated to the first-order perturbation theory from the quasi-particle equation [104, 106]

$$E_i^{\mathrm{QP}} = \epsilon_i^{\mathrm{KS}} + \langle \Psi_i | \Sigma(E_i^{\mathrm{QP}}) - v_{\mathrm{xc}}^{\sigma} | \Psi_i \rangle \,. \tag{2.5.4}$$

2.5.2 GW Approximation

The self-energy operator Σ can be obtained by the solution of many-body problem self-consistently, but this method is very difficult to handle with. The practical way to simplify this is the so-called GW approximation (GWA), first proposed by Hedin in 1965 [109]. Hedin introduced set of five equations in five variables, which relate the Green function G (see appendix B), self-energy Σ (12), polarization propagator P (12), screened potential $W{=}\epsilon^{-1}\nu$ and vertex function Γ (123) [110]

$$\Sigma(12) = i\int d(34)G(14^{+})W(13)\Gamma(423), \tag{2.5.5}$$

$$P(12) = -i\int d(34)G(13)G(41^{+})\Gamma(342), \tag{2.5.6}$$

$$W(12) = \upsilon(12) + \int d(34)W(13)P(34)\upsilon(42), \tag{2.5.7}$$

$$\Gamma(123) = \delta(12)\delta(13) + \int d(4567)\frac{\delta\Sigma(12)}{\delta G(45)}G(46)G(75)\Gamma(673), \tag{2.5.8}$$

$$G(12) = G_{\mathrm{KS}}(12) + \int (d34)G_{\mathrm{KS}}(13)\Sigma(34)G(42), \tag{2.5.9}$$

where the simplifies notation $1{=}\ (x_1, t_1)$ *etc* and 1^{+} denotes that t $\rightarrow$ t + η for some positive infinitesimal η, and δ(1,2) is the Dirac delta function. Hedin's equations should in principle be solved self-consistently, and they are too computationally expensive for studying realistic systems. the most common approximation to simplify this approach is the so-called GW approximation. The vertex corrections are thereby excluded which corresponds to setting $\Gamma(123) = \delta(12)\delta(13)$ in equation (2.5.8). Consequently, the irreducible polarizability (see equation (2.5.6)) is described by $P(12) = -iG(12)G(21^{+})$, which equals the random phase approximation (RPA) and the neglect of electron-hole interactions [111, 112, 113]. Within the GW approximation, the self-energy $\Sigma(\mathbf{r}, \mathbf{r}^{'}; E_i^{\mathrm{QP}})$ can be written in terms of the Green function G and the screened Coulomb interaction W (explaining the name of GW approximation)

$$\Sigma_{\mathrm{GW}}(\mathbf{r}, \mathbf{r}^{'}; t) = iG(\mathbf{r}, \mathbf{r}^{'}; t)W(\mathbf{r}, \mathbf{r}, \mathbf{r}^{'}; t), \tag{2.5.10}$$

or its equivalent in terms of the energy

$$\Sigma_{\mathrm{GW}}(\mathbf{r}, \mathbf{r}^{'}; E) = i\int G(\mathbf{r}, \mathbf{r}^{'}; E + E^{'})W(\mathbf{r}, \mathbf{r}^{'}; E)dE^{'}. \tag{2.5.11}$$

The screened potential W can be obtained from the bare Coulomb interaction υ via

$$W(\mathbf{r},\mathbf{r}^{'};E) = \upsilon(\mathbf{r},\mathbf{r}^{'}) + \int d\mathbf{r}_1 d\mathbf{r}_2 W(\mathbf{r},\mathbf{r}_1;E)P(\mathbf{r}_1,\mathbf{r}_2;E)\upsilon(\mathbf{r}_2,\mathbf{r}^{'}), \tag{2.5.12}$$

where the polarization $P(\mathbf{r}_1,\mathbf{r}_2;E)$ is given by

$$P(\mathbf{r}_1,\mathbf{r}_2;E) = -iG(\mathbf{r},\mathbf{r}^{'};E)G(\mathbf{r}^{'},\mathbf{r};E), \tag{2.5.13}$$

or equivalently

$$W(\mathbf{r},\mathbf{r}^{'};E) = \int d(\mathbf{r}_1)\varepsilon^{-1}(\mathbf{r},\mathbf{r}_1;E)\upsilon(\mathbf{r_1},\mathbf{r}^{'}), \tag{2.5.14}$$

where $\varepsilon^{-1}(\mathbf{r},\mathbf{r}_1;E)$ is the dielectric function, which is normally calculated within the random phase approximation (RPA). The Equations (B.0.4), (2.5.11), (2.5.12) and (2.5.13) form a closed set that, can be solved self-consistently without further approximation [64].

2.5.3 Bethe-Salpeter Equation (BSE)

The inclusion of vertex Γ in equation (2.5.6) can be achieved through a second iteration Hedin's equation, using $\Sigma = iGW$ in the latter, this yields an integral equation for Γ

$$\Gamma(1,2,3) = \delta(1,2)\delta(1,3) + iW(1^{+},2)\int d(6,7)G(1,6)G(7,2)\Gamma(6,7,3), \tag{2.5.15}$$

using the approximation $\frac{\partial\Sigma}{\partial G} \approx iW$.

One can transform equation (2.5.15) to an integral form for a generalized ${}^{3}P$, defined as

$${}^{3}P(312) = -i\int d(67)G(16)G(72)\Gamma(673), \tag{2.5.16}$$

where ${}^{3}P(312)$ is a three-point polarizability. Multiplying with $-iG(41)G(25)$ on the left and integrating over $d(12)$

$${}^{3}P(345) = -iG(43)G(35) + i\int d(12)G(41)G(25)W(1^{+}2){}^{3}P(312). \tag{2.5.17}$$

In principle the polarization P can be obtained from $P(31) = {}^{3}P(311)$. However, the kernel GGW of the integral equation (2.5.15) can be seen as a four-point function. Therefore, it is convenient to introduce a four-point ${}^{4}P$. Following Ref. [113], we can

introduce the four dynamically interaction

$$^4W(1234) = W(12)\delta(13)\delta(24). \tag{2.5.18}$$

Then we get for equation (2.5.15) the four-point integral equation

$$^4P = {}^4P_{\mathrm{IQP}} - {}^4P^4W^4P_{\mathrm{IQP}}, \tag{2.5.19}$$

where P_{IQP} is the independent-quasi-particle polarization. Using Dyson-like screening equation one can directly obtain $\overline{P}$

$$\overline{P} = P + P\overline{v}\overline{P}, \tag{2.5.20}$$

where $\overline{v}$ is bare Coulomb potential interaction without long range term in reciprocal space reads

$$\overline{v}_{\mathbf{G}}(\mathbf{q}) = \begin{cases} 0 & \text{if } \mathbf{G} = 0; \\ v_{\mathbf{G}}(\mathbf{q}) = \frac{4\pi}{|\mathbf{q}+\mathbf{G}|^2} & \text{else.} \end{cases} \tag{2.5.21}$$

Putting together equations (2.5.19) and (2.5.20), we obtain the Bethe-Salpeter equation (BSE)

$$^4\overline{P} = {}^4P_{IQP} - {}^4P_{IQP}K^4\overline{P}, \tag{2.5.22}$$

where the kernel of the Bethe-Salpeter equation K is given by

$$K(1234) = \delta(12)\delta(34)\overline{v}(13) - \delta(13)\delta(24)W(12). \tag{2.5.23}$$

The Bethe-Salpeter approach to the calculation of two-particle excited states is straightforward extension of the GW approach for the calculation of one-particle excited states; and it leads to an effective two-particle excitonic Hamiltonian H^{2P} which is the general form found in time-dependent problems, which moreover provides information about the excitonic eigenstates and eigenvalues. The effective two-Hamiltonian (H^{2P}) is given by

$$H^{2P}(n_1n_2),(n_3n_4) = (\varepsilon_{n_2} - \varepsilon_{n_1})\delta n_1n_3\delta n_2n_4 + (fn_1 - fn_2)K(n_1n_2),(n_3n_4), \tag{2.5.24}$$

the indices n_i refer to the fact that matrix elements have been taken with respect to four eigenfunctions of the starting effective static one-particle Hamiltonian , fn_1 and

fn_2 represents the occupation numbers and each couple $(nn^{'})$ corresponds to a pair (vc) of an occupied and an empty state. In general the two-particle Hamiltonian is not Hermitian and can be further separated into four blocks: two blocks on the diagonal with the transition energies and the interaction Kernel K, and two off-diagonal coupling blocks with contributions only from the interaction Kernel:

$$H^{2p} = \begin{bmatrix} H^{2p,\mathrm{res}} & H^{\mathrm{coupling}} \\ -[H^{\mathrm{coupling}}]^* & -[H^{2p,\mathrm{res}}]^* \end{bmatrix}. \tag{2.5.25}$$

The resonant part is Hermitian, $(\mathrm{H}^{2p,\mathrm{res}})^* = (\mathrm{H}^{2p,\mathrm{res}})^T$, while the coupling part is symmetric, $\mathrm{H}^{\mathrm{coupling}} = (\mathrm{H}^{\mathrm{coupling}})^T$. Neglecting the coupling part is called the Tamm-Dancoff approximation. The effective two-particle equation with the static screening takes the form

$$H^{2p,\mathrm{res}}(n_1n_2)(n_3n_4)A_\lambda^{(n_3n_4)}) = E_\lambda A_\lambda^{(n_1n_2)}, \tag{2.5.26}$$

where E_λ and $A_\lambda^{n_1n_2}$ are the eigenvalues and eigenstates of the effective two-particle Hamiltonian H^{2P}, respectively. E_λ and $A_\lambda^{n_1n_2}$ can be obtained by diagonalising the resonant part of the two-particle Hamiltonian (2.5.26). From the obtained eigenvalues E_λ and eigenstates $A_\lambda^{n_1n_2}$ the four- and two-point quantities of interest are constructed [113]. The modified response function can be build from E_λ and $A_\lambda^{n_1n_2}$

$$\overline{P} = \sum_{\lambda\lambda'} \frac{A_\lambda^{(n_1n_2)} A_{\lambda'}^{(n_3n_4)}}{E_\lambda - \omega} N_{\lambda\lambda'}^{-1}, \tag{2.5.27}$$

where $N_{\lambda\lambda'}^{-1}$ is the overlap matrix defined by

$$N_{\lambda\lambda'}^{-1} = \sum_{n_1n_2} [A^{(n_1n_2)}]^* A_{\lambda'}^{(n_1n_2)}, \tag{2.5.28}$$

The *macroscopic dielectric function* $\varepsilon_{\mathrm{mac}}(\omega)$ can be constructed from a modified response function $\overline{P}$:

$$\varepsilon_{\mathrm{mac}}(\omega) = 1 - \lim_{q\to 0}[\upsilon_0(\mathbf{q})\overline{P}_{00}(\mathbf{q},\omega)]. \tag{2.5.29}$$

Considering only the resonant part of H^{2P}, the resulting operator is Hermitian and its eigenstates are orthogonal. Therefore, the simpler formula is

$$\varepsilon_{\mathrm{M}}(\omega) = 1 - \lim_{q\to 0} \upsilon_0(\mathbf{q}) \Sigma_\lambda \frac{|\Sigma_{n_1n_2}\langle n_1|\, e^{-i\mathbf{q}\cdot\mathbf{r}} |n_2\rangle A_\lambda^{n_1n_2}|^2}{\omega - E_\lambda + i\eta}, \tag{2.5.30}$$

2.6 Transport Phenomena

In this Section, a detailed derivation of theoretical framework needed for thermoelectric transport properties (electrical conductivity σ, Seebeck coefficient S and electronic thermal conductivity k_e) will be presented with using Boltzmann transport equation and relaxation time approximation. Moreover, the lattice thermal conductivity k_L will be described through the Boltzmann transport equation for phonons.

2.6.1 The Boltzmann Equation

The distribution function (DF) $f_{\mathbf{k}}(\mathbf{r}, t)$ determines the probability of having an electron with wave vector $\mathbf{k}$ at position $\mathbf{r}$ in space at a given time t. The Boltzmann equation begin with an attempt to determine how $f_{\mathbf{k}}(\mathbf{r}, t)$ can change with time. There are three possible type of effects [114]:

First due to the motion of the electrons, carriers will be moving into and out of any volume element around $\mathbf{r}$. If $\mathbf{v_k}$ is the velocity of a carrier in the $\mathbf{k}$ state, in a time interval t, the electron moves a distance equal to $t\mathbf{v_k}$. Thus the number of electrons in the neighbourhood of $\mathbf{r}$ at time t is equal to the number of carriers in the neighbourhood of $\mathbf{r} - t\mathbf{v_k}$ at time 0.

$$f_{\mathbf{k}}(\mathbf{r}, t) = f_{\mathbf{k}}(\mathbf{r} - t\mathbf{v_k}, 0). \tag{2.6.1}$$

This means that the rate of change of the DF due to diffusion is

$$\left.\frac{\partial f_{\mathbf{k}}}{\partial t}\right|_{\text{diff}} = -\frac{\partial f_{\mathbf{k}}}{\partial \mathbf{r}}.\mathbf{v_k}. \tag{2.6.2}$$

Second due to the presence of external forces $\mathbf{F}_{\text{ext}}$, electrons will be changing their momentum according to

$$\frac{\partial \mathbf{k}}{\partial t} = \frac{1}{\hbar}\mathbf{F}_{\text{ext}}, \tag{2.6.3}$$

for an electric and magnetic fields, the rate of change $\mathbf{k}$ is given by

$$\frac{\partial \mathbf{k}}{\partial t} = \frac{e}{\hbar}\left[\mathbf{E} + \frac{\mathbf{v_k} \times \mathbf{H}}{c}\right], \tag{2.6.4}$$

we can look upon this as the velocity of carrier in $\mathbf{k}$ space, so that, in analogy to the diffusion changes in equation (2.6.1), we can argue that particles at $t = 0$ with $\mathbf{k} - \dot{\mathbf{k}}t$

will have $\mathbf{k}$ at the time t, that is

$$f_{\mathbf{k}}(\mathbf{r},t) = f_{\mathbf{k}-\dot{\mathbf{k}}t}(\mathbf{r},0). \tag{2.6.5}$$

The distribution changes, because of the fields, at the rate,

$$\left.\frac{\partial f_{\mathbf{k}}}{\partial t}\right|_{\text{field}} = -\dot{\mathbf{k}}\frac{\partial f_{\mathbf{k}}}{\partial \mathbf{k}} = -\frac{e}{\hbar}\left[\mathbf{E} + \frac{\mathbf{v}_{\mathbf{k}} \times \mathbf{H}}{c}\right].\frac{\partial f_{\mathbf{k}}}{\partial \mathbf{k}}. \tag{2.6.6}$$

Third the rate of change of the distribution function $f_{\mathbf{k}}$ due to elastic scattering is

$$\left.\frac{\partial f_{\mathbf{k}}}{\partial t}\right|_{\text{scatt}} = \int \{f_{\mathbf{k}'}(1-f_{\mathbf{k}}) - f_{\mathbf{k}}(1-f_{\mathbf{k}'})\}Q(\mathbf{k},\mathbf{k}')d\mathbf{k}' \tag{2.6.7}$$

where $Q(\mathbf{k},\mathbf{k}')$ is the transition probability define the rate of transition from the state $\mathbf{k}$ to $\mathbf{k}'$ [114]. The first term in equation (2.6.7) represents the rate at which electrons are coming from an occupied $\mathbf{k}'$ state to a an unoccupied $\mathbf{k}$ state, and the second term represents the loss term [115].

Under steady-state conditions, the Boltzmann equation says that at any point, and for any value of $\mathbf{k}$, the net rate of change of $f_{\mathbf{k}}(\mathbf{r},t)$ is zero

$$\left.\frac{\partial f_{\mathbf{k}}}{\partial t}\right|_{\text{diff}} + \left.\frac{\partial f_{\mathbf{k}}}{\partial t}\right|_{\text{field}} + \left.\frac{\partial f_{\mathbf{k}}}{\partial t}\right|_{\text{scatt}} = 0, \tag{2.6.8}$$

where the subscripts diff, field and scatt stand for diffusion, external field and scattering respectively [114, 115]. Boltzmann equation is usually solved using two approximations: First, assuming that the steady state distribution function does not depart very far from equilibrium. Let us define

$$g_{\mathbf{k}} = f_{\mathbf{k}} - f^0_{\mathbf{k}}, \tag{2.6.9}$$

where $g_{\mathbf{k}}$ represents the deviation of the distribution function from equilibrium case $f^0_{\mathbf{k}}$. Second, using the relaxation time approximation (RTA) for the scattering term so that the system returns to equilibrium uniformly:

$$\left.\frac{\partial f_{\mathbf{k}}}{\partial t}\right|_{\text{scatt}} = -\frac{f_{\mathbf{k}} - f^0_{\mathbf{k}}}{\tau} = \frac{g_{\mathbf{k}}}{\tau}, \tag{2.6.10}$$

where τ denotes the relaxation time and in general is a function of momentum. The relaxation time measures how quickly the electrons are returns to the equilibrium distribution when the fields are turned off [114, 115].

With equation (2.6.9) in equation (2.6.8), and using equation (2.6.2) and equation (2.6.6), the Boltzmann equation becomes:

$$-\mathbf{v_k}.\nabla_{\mathbf{r}} f_{\mathbf{k}} - \frac{e}{\hbar}\left[\mathbf{E} + \frac{\mathbf{v_k}\times\mathbf{H}}{c}\right].\nabla_{\mathbf{k}} f_{\mathbf{k}} = -\frac{\partial f_{\mathbf{k}}}{\partial t}\bigg|_{\text{scatt}}. \tag{2.6.11}$$

Substituting equation (2.6.9) into (2.6.11), we get

$$-\mathbf{v_k}.\nabla_{\mathbf{r}} f^0_{\mathbf{k}} - \frac{e}{\hbar}\left[\mathbf{E} + \frac{\mathbf{v_k}\times\mathbf{H}}{c}\right].\nabla_{\mathbf{k}} f^0_{\mathbf{k}} = -\frac{\partial f_{\mathbf{k}}}{\partial t}\bigg|_{\text{scatt}} + \mathbf{v_k}.\nabla_{\mathbf{r}} g_{\mathbf{k}} + \frac{e}{\hbar}\left[\mathbf{E} + \frac{\mathbf{v_k}\times\mathbf{H}}{c}\right].\nabla_{\mathbf{k}} g_{\mathbf{k}}. \tag{2.6.12}$$

Using the equilibrium distribution function

$$f^0_{\mathbf{k}} = \frac{1}{e^{\left[\frac{E_{\mathbf{k}}-\mu}{k_B T}\right]}+1}, \tag{2.6.13}$$

where $E_{\mathbf{k}}$ is the particle energy, k_B is the Boltzmann's constant and μ is the chemical potential, in the present of an electric field and retaining terms only to second-order in electric field we get from equation (2.6.12) [114, 115]

$$-\frac{\partial f^0_{\mathbf{k}}}{\partial E_{\mathbf{k}}}.\mathbf{v_k}.\left[-\frac{(E_{\mathbf{k}}-\mu)}{T}\nabla T + e\mathbf{E} - \nabla\mu\right] = -\frac{\partial f_{\mathbf{k}}}{\partial t}\bigg|_{\text{scatt}} + \mathbf{v_k}.\nabla_{\mathbf{r}} g_{\mathbf{k}} + \frac{e}{\hbar}\left[\frac{\mathbf{v_k}\times\mathbf{H}}{c}\right].\nabla_{\mathbf{k}} g_{\mathbf{k}}. \tag{2.6.14}$$

This equation is the so-called linearised Boltzmann transport equation, for more details see ref. [114, 115]. Assuming that we have a temperature gradient as well as an electric field in the system, the Boltzmann equation becomes

$$\Big(-\frac{\partial f^0_{\mathbf{k}}}{\partial E_{\mathbf{k}}}\Big)\mathbf{v_k}.\left[-\frac{(E_{\mathbf{k}}-\mu)}{T}\nabla T + e\mathbf{E} - \nabla\mu\right] = -\frac{\partial f_{\mathbf{k}}}{\partial t}\bigg|_{\text{scatt}}. \tag{2.6.15}$$

Substituting equation (2.6.10) into equation (2.6.15) gives [114, 115]

$$f_{\mathbf{k}} = f^0_{\mathbf{k}} - \Big(\frac{\partial f^0_{\mathbf{k}}}{\partial E_{\mathbf{k}}}\Big)\tau\mathbf{v_k}.\left[-\frac{(E_{\mathbf{k}}-\mu)}{T}\nabla T + e\mathbf{E} - \nabla\mu\right]. \tag{2.6.16}$$

2.6.2 Transport Coefficients

The presence of temperature gradient ∇T or an electric field $\mathbf{E}$ induces thermal or electrical current in a material. The relations between the temperature gradient ∇T and the electric field $\mathbf{E}$ with their corresponding heat current density $\mathbf{J}_Q$ and electrical

current density $\mathbf{J}_e$ for a solid are

$$\begin{aligned}\mathbf{J}_e &= \sigma(\mathbf{E} - S\nabla T)\\ \mathbf{J}_Q &= T\sigma S\mathbf{E} - K\nabla T,\end{aligned} \tag{2.6.17}$$

where σ is the electrical conductivity, K is the thermal conductivity. The Seebeck coefficient S, is defined as the ratio of the electric field to the temperature gradient ∇T when the electric current is zero. The electronic contribution to the thermal conductivity κ_e, is defined as the heat current of temperature gradient when the electric current is zero [116],

$$\kappa_e = K - S^2\sigma T. \tag{2.6.18}$$

To calculate the electrical conductivity, we need to calculate the corresponding electric current density [114]

$$\mathbf{J}_e = e\sum_{\mathbf{k}} f_{\mathbf{k}}\mathbf{v}_{\mathbf{k}}, \tag{2.6.19}$$

where e is the charge of the carriers. In the absence of temperature gradient equation (2.6.16) takes the form

$$f_{\mathbf{k}} = f^0_{\mathbf{k}} + e\big(-\frac{\partial f^0_{\mathbf{k}}}{\partial E_{\mathbf{k}}}\big)\tau\mathbf{v}_{\mathbf{k}}.\mathbf{E}. \tag{2.6.20}$$

Using this expression to calculate the current, the electrical conductivity takes the form

$$\sigma = e^2\sum_{\mathbf{k}}\big(-\frac{\partial f^0_{\mathbf{k}}}{\partial E_{\mathbf{k}}}\big)\mathbf{v}_{\mathbf{k}}\mathbf{v}_{\mathbf{k}}\tau. \tag{2.6.21}$$

Seebeck coefficient S and electronic thermal conductivity κ_e can be derived using similar expression. The transport distribution (TD) $\sum_{\mathbf{k}}\mathbf{v}_{\mathbf{k}}\mathbf{v}_{\mathbf{k}}\tau$ is the kernel of all transport coefficients, once it is calculated, all transport coefficients necessary to determine the figure of merit ZT can be obtained using scalar coefficients, [117]

$$\sigma = e^2\int dE\big(-\frac{\partial f^0_{\mathbf{k}}}{\partial E_{\mathbf{k}}}\big)\sum_{\mathbf{k}}\mathbf{v}_{\mathbf{k}}\mathbf{v}_{\mathbf{k}}\tau \tag{2.6.22}$$

$$S = ek_B\sigma^{-1}\int dE\big(-\frac{\partial f^0_{\mathbf{k}}}{\partial E_{\mathbf{k}}}\big)\sum_{\mathbf{k}}\mathbf{v}_{\mathbf{k}}\mathbf{v}_{\mathbf{k}}\tau\frac{E_{\mathbf{k}}-\mu}{k_BT} \tag{2.6.23}$$

$$\kappa_e = k_B^2T\int dE\big(-\frac{\partial f^0_{\mathbf{k}}}{\partial E_{\mathbf{k}}}\big)\sum_{\mathbf{k}}\mathbf{v}_{\mathbf{k}}\mathbf{v}_{\mathbf{k}}\tau\big[\frac{E_{\mathbf{k}}-\mu}{k_BT}\big]^2 - T\sigma S^2. \tag{2.6.24}$$

2.7 Lattice Thermal Conductivity

The lattice thermal conductivity κ_L can be described through the BTE for phonons. The phonon distribution function (PDF) represents the average number of phonons with wave vector $\mathbf{q}$. In equilibrium, the PDF can be written as [118]

$$n^0_{\mathbf{q}} = \frac{1}{e^{\left[\frac{\hbar\omega_{\mathbf{q}}}{k_B T}\right]} - 1}. \tag{2.7.1}$$

The BTE for phonons with the contribution to the rate of change from diffusion and scattering mechanisms takes the form

$$\left.\frac{\partial n_{\mathbf{q}}}{\partial t}\right| = \left.\frac{\partial n_{\mathbf{q}}}{\partial t}\right|_{\text{diff}} + \left.\frac{\partial n_{\mathbf{q}}}{\partial t}\right|_{\text{scatt}}. \tag{2.7.2}$$

When the thermal gradient is present, phonons diffuse with a rate

$$\left.\frac{\partial n_{\mathbf{q}}}{\partial t}\right|_{\text{diff}} = -(\mathbf{v}_g.\nabla T)\frac{\partial n^0_{\mathbf{q}}}{\partial T}, \tag{2.7.3}$$

where $\mathbf{v}_g$ is the phonon group velocity. In the steady state, the scattering processes tend to restore PDF ($n_{\mathbf{q}}$) to its equilibrium from $n^0_{\mathbf{q}}$

$$-(\mathbf{v}_g.\nabla T)\frac{\partial n^0_{\mathbf{q}}}{\partial T} = \frac{n_{\mathbf{q}} - n^0_{\mathbf{q}}}{\tau_q}, \tag{2.7.4}$$

where τ_q is the phonon scattering relaxation time. From Fourier's law of heat conductivity one can derive an expansion for lattice thermal conductivity, that is

$$\mathbf{Q} = -\kappa_L \nabla T, \tag{2.7.5}$$

where Q is the heat flux and the proportional term κ_l is the lattice contribution to the thermal conductivity. The total heat flux from phonon can be given as [118, 119]

$$\mathbf{Q} = \sum_{\mathbf{q}} n_{\mathbf{q}} \hbar\omega_{\mathbf{q}} \mathbf{v}_g. \tag{2.7.6}$$

Substituting equation (2.7.4) into equation (2.7.6) reads

$$\begin{aligned} \mathbf{Q} &= -\sum_{\mathbf{q}} \hbar\omega_{\mathbf{q}} \mathbf{v}_g^2 \left\langle \cos^2\theta \right\rangle \tau_q \frac{\partial n_{\mathbf{q}}^0}{\partial T} \nabla T \\ &= -\frac{1}{3} \sum_{\mathbf{q}} \hbar\omega_{\mathbf{q}} \mathbf{v}_g^2 \tau_q \frac{\partial n_{\mathbf{q}}^0}{\partial T} \nabla T. \end{aligned} \tag{2.7.7}$$

Equating equations (2.7.5) and (2.7.7), the lattice thermal conductivity takes the form

$$\kappa_L = -\frac{\mathbf{Q}}{\nabla T} = \frac{1}{3} \sum_{\mathbf{q}} \hbar\omega_{\mathbf{q}} \mathbf{v}_g^2 \tau_q \frac{\partial n_{\mathbf{q}}^0}{\partial T}. \tag{2.7.8}$$

3

Computational Details

In this chapter, we focus on various physical and mathematical aspects involved in the calculation of ground state and excited state properties of materials using density functional theory (DFT) and many body perturbation theory calculations described in Chapter 2.

3.1 DFT Calculations

All calculations at the electronic structure level described here were performed using density functional theory as implemented in the Vienna Ab initio simulation package (VASP) (see Appendix C)based on pseudopotentials and a plane wave basis set. In VASP, the electron-ion interaction is described by the projector-augmented wave (PAW) method [86]. To describe electron exchange and correlation effects, we used four different functionals: the Generalized Gradient Approximation (GGA) as parametrized by Perdew, Burke and Ernzerhof PBE [92], PBEsol [93], the modified Becke Johnson (MBJ) [95] and the hybrid functional HSE06 [94]. For the HSE06, a default mixing parameter of 25% and 0.2 $\mathring{A}^{-1}$ screening parameter was used for all calculations. It is sufficient to say that the 25% fraction of exact Hartree-Fock exchange and $\mathring{A}^{-1}$ screening parameter were enough to predict a band gap of 1.21 eV (see Table (4.15)) for $CH_3NH_3SnI_3$, which is in agreement with the experimental results (1.21 eV and 1.35 eV) [30]. The energy convergence criteria was set to 10^{-8} eV. The cut-off energy for plane wave basis and self-consistent convergence criteria for structural optimization were

set to be 520 eV and 10^{-8} eV respectively. These parameters were found to be sufficient for energy convergence to within 1 meV/$\AA$. A **k**-mesh of $4 \times 4 \times 2$ and $4 \times 8 \times 2$ were used in the optimization for $CH_3NH_3XI_3$ (X= Pb or Sn) and a $CsPbI_3$ respectively.

The Crystal Structure

$CH_3NH_3XI_3$ (X = Pb or Sn)

The unit cell of $CH_3NH_3XI_3$ (X= Pb or Sn) contains of 48 atoms (24 H atoms, 4 Pb or Sn atoms, 4 C atoms, 12 I atoms, and 4 N atoms). The crystal structure of the orthorhombic phase (space group Pnma 62) of the halide perovskite and its corresponding Brillouin zone are shown in Figure (3.1).

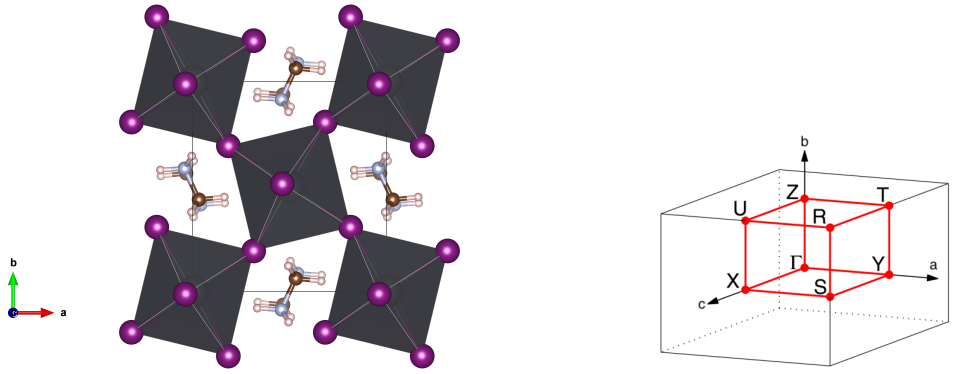


Figure 3.1: (Color online) The crystal structure of the $CH_3NH_3XI_3$ (X= Pb or Sn) orthorhombic phase with space group Pnma (No. 62) (left) the Brillouin zone of the orthorhombic lattice (right) [5].

Caesium Lead Triiodide Perovskite

The unit cell of $CsPbI_3$ contains of 48 atoms (4 Cs atoms, 4 Pb and 12 I atoms). The crystal structure of the orthorhombic phase (space group Pnma 62) of the halide perovskite is shown in Figure (3.2).

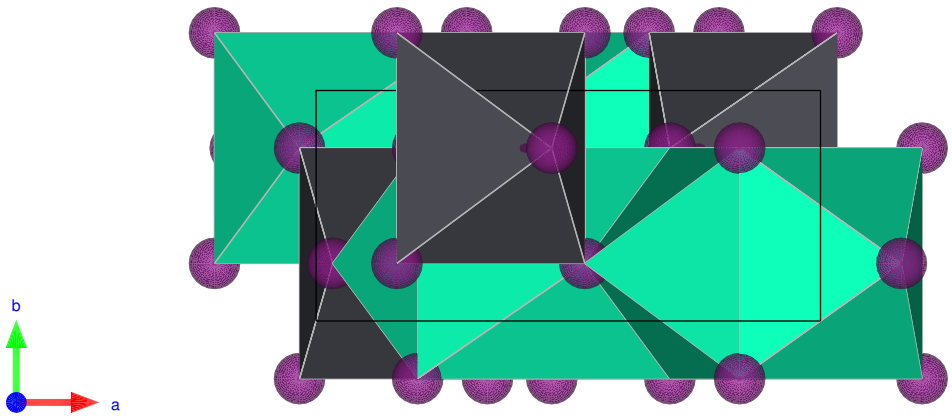


Figure 3.2: (Color online) The crystal structure of the $CsPbI_3$ orthorhombic phase with space group Pnma (No. 62).

3.2 Calculations of Structural Properties

3.2.1 Cohesive Energy

The cohesive energy E_{coh} is defined as the negative of the energy that must be supplied to the solid to separate its constituents into neutral free atoms at rest and at finite separation. Therefore, in ab-initio calculations, the cohesive energy is computed as the difference between the calculated total energy of a unit cell and total energy of its isolated atoms [105, 120, 121].

$$E_{\text{coh}} = E(\text{crystal}) - E(\text{atoms}) = E(\text{crystal}) - \sum_{\text{atom}} E_{\text{atom}}^{\text{isolated}}. \tag{3.2.1}$$

3.2.2 Bulk Modulus and its Pressure Derivative B′

The bulk modulus for any solid is defined as

$$B = -V\frac{\partial P}{\partial V} = V\frac{\partial^2 E}{\partial V^2}. \tag{3.2.2}$$

For given total binding energy E, the external pressure P on the unit cell can be calculated in the form

$$P = -\frac{\partial E}{\partial V}, \tag{3.2.3}$$

when the system is at equilibrium (*i.e.* $P = 0$). The equilibrium isotropic elastic properties of a bulk system are described by its compressibility K_0, so from equations (3.2.2) and (3.2.3), the equilibrium bulk modulus is given by [105, 122, 123]

$$\frac{1}{K_0} = B_0 = -V\frac{\partial P}{\partial V}\bigg|_{V=V_0} = -V\frac{\partial^2 E}{\partial V^2}\bigg|_{V=V_0}, \tag{3.2.4}$$

and its pressure derivative theoretically defined as

$$B_0' = \frac{\partial B}{\partial P}\bigg|_{P=0} = \frac{1}{B_0}\left(V\frac{\partial}{\partial V}(V\frac{\partial^2 E}{\partial V^2})\right)\bigg|_{V=V_0}. \tag{3.2.5}$$

3.2.3 Equation of State and Lattice Parameters

Knowledge of the equation of state (i.e. pressure (P), volume (V) and temperature (T) relationship), based on either calculation or measurement, is important in both basic and applied sciences. It depends on the nature of the interatomic interactions and therefore provides insight into the nature of fundamental solid state theories, and it can be used to determine thermodynamics parameters. There are many semi-empirical functional and theoretical description of equation of state (EOS) [124, 125]. In this work, isothermal third-order Birch-Murnghan equation of state [126] was utilized.

When the system is at equilibrium (i.e. its pressure is zero), energies in Birch-Murnghan equation of state are expressed as

$$E(V) = E_0 + \frac{9V_0B_0}{16}\left\{\left[\left(\frac{V_0}{V}\right)^{\frac{2}{3}} - 1\right]^3 B_0' + \left[(\frac{V_0}{V}\right)^{\frac{2}{3}} - 1\right]^2\left[6 - 4\left(\frac{V_0}{V}\right)^{\frac{2}{3}}\right]\right\}, \tag{3.2.6}$$

where E_0 and V_0 are equilibrium energy and volume at zero pressure. Using equation

(3.2.3), the pressure in isothermal Birch-Murnghan 3rd-order equation of state is [126, 127, 128]

$$P(V) = \frac{3B_0}{2}\left[\left(\frac{V_0}{V}\right)^{\frac{7}{3}} - \left(\frac{V_0}{V}\right)^{\frac{5}{3}}\right]\left\{1 + \frac{3}{4}\left(B_0^{'} - 4\right)\left[\left(\frac{V_0}{V}\right)^{\frac{2}{3}} - 1\right]\right\}. \tag{3.2.7}$$

The calculated quantity from DFT is the total energy at zero temperature. Therefore, $B_0^{'}$ and B_0 are related to energy-volume $E(V)$ curve and measure its curvature about the equilibrium volume V_0 [129].

To estimate the lattice parameters of the structure under study and to study its energy-volume equation of state curve , the calculations were performed in two steps. First: we relaxed the structural ions (using PBE and PBEsol functionals) and generate a guess equilibrium volume $V_0{}^*$. Second: we generate thirteen different volumes around the guessed equilibrium volume $V_0{}^*$, then we proceed and performed a static calculation (atomic positions fixed) using Blöchl tetrahedron correction. We then extract energy, and the obtained energies (E) as a function of volume (V) per atom (equation (3.2.6)) were fitted using least-squares method with a third-order Birch-Murnghan equation of state [126], where B_0, $B_0^{'}$, V_0 and E_0 are the fitting parameters.

3.3 Stability Properties

Relaxing a structure untill all the forces on the atoms are zero, does not mean that the structure will remain stable under the influence of external forces, and in the harmonic approximation, and to determine the stability of the structure, it is necessary to check its elastic and dynamical stabilities. In this section, we give the computational details on the elastic and dynamical stabilities.

3.3.1 Elastic Stability

The elastic constants are very important to study the information about the mechanical properties such as bulk moduli, shear moduli, Young's modulus, Poisson's ratio and anisotropy of material. In DFT calculations the elastic constants can be computed using two methods: the energy-strain approach and the stress-strain approach. In this research, the elastic constants are determined from linear fit of the calculated stress-strain functions according to Hooke's law. The elastic strain energy density is given

by $U = \frac{\Delta E}{V_0} = \frac{1}{2}\sum_i^6 \sum_j^6 C_{ij} e_i e_j$ [130], where ΔE is the energy difference between the deformed and equilibrium structures; V_0 is the equilibrium volume of cell; C_{ij} are the elastic constants; e_i and e_j are strains. For a stable orthorhombic structure, the nine independent elastic constants should satisfy the Born stability criteria [131]:

$$\begin{aligned} C_{ii} > 0; & C_{11}C_{22} > C_{12}^2; \\ & C_{11}C_{22}C_{33} + 2C_{12}C_{13}C_{23} - \\ & C_{11}C^2{}_{23} - C_{22}C^2{}_{13} - C_{33}C^2{}_{12} > 0. \end{aligned} \tag{3.3.1}$$

Bulk elastic properties: bulk modulus B and shear modulus G were calculated using Voigt-Reuss-Hill averaging schemes [132, 133, 134]. For an orthorhombic crystal, the Viogt bulk modulus B_V and the Viogt shear modulus G_V are defined as [135]

$$B_V = \frac{1}{9}\Big[C_{11} + C_{22} + C_{33}\Big] + \frac{2}{9}\Big[C_{12} + C_{13} + C_{23}\Big], \tag{3.3.2}$$

$$G_V = \frac{1}{15}\Big[C_{11} + C_{22} + C_{33} - C_{12} - C_{13} - C_{23}\Big] + \frac{1}{5}\Big[C_{44} + C_{55} + C_{66}\Big], \tag{3.3.3}$$

and the Reuss bulk modulus B_R and the Reuss shear modulus G_R are defined as

$$B_R = 1/[(s_{11} + s_{22} + s_{33}) + 2(s_{12} + s_{13} + s_{23})], \tag{3.3.4}$$

$$G_R = 15/[4(s_{11} + s_{22} + s_{33} - s_{12} - s_{13} - s_{23}) + 3(s_{44} + s_{55} + s_{66})], \tag{3.3.5}$$

where s_{ij} are elastic compliances which can be obtained through an inversion of the elastic constant matrix, $S = C^{-1}$. According to the Hill approximation [134], the bulk modulus and shear modulus are then given by:

$$B_H = \frac{1}{2}\big(B_R + B_V\big); G_H = \frac{1}{2}\big(G_R + G_V\big). \tag{3.3.6}$$

Young's modulus E and Poisson's ratio ν can be given by

$$\begin{aligned} E_H &= 9B_H G_H/(3B_H + G_H), \\ \nu &= (3B_H - 2G_H)/2(3B_H + G_H). \end{aligned} \tag{3.3.7}$$

A measure of the degree of anisotropy in the bonding between atoms in different planes can be provided by the shear anisotropic factors. The crystal shear anisotropy factors

A_1 in {100} planes between ⟨011⟩ and ⟨010⟩ directions, A_2 in {010} planes between ⟨101⟩ and ⟨001⟩ directions and A_3 in {001} planes between ⟨110⟩ and ⟨010⟩ directions are defined as [135, 136]

$$\begin{aligned} A_1 &= \frac{4C_{44}}{C_{11}+C_{33}-2C_{13}}; A_2 = \frac{4C_{55}}{C_{22}+C_{33}-2C_{23}}; \\ A_3 &= \frac{4C_{66}}{C_{11}+C_{22}-2C_{12}}. \end{aligned} \tag{3.3.8}$$

Under isotropic pressure P, the total energy E of the crystal at a volume V that results from a strained reference volume V^{ref} is given by [137, 138]

$$\begin{aligned} E(V,\epsilon) =& E(V^{\text{ref}},\epsilon=0) + V^{\text{ref}}\sum_{ij}\sigma_{ij}\epsilon_{ij} \\ &+ \frac{V^{\text{ref}}}{2}\sum_{ij}C_{ij}(V^{\text{ref}})\epsilon_i\epsilon_j + O(\epsilon^3), \end{aligned} \tag{3.3.9}$$

where σ_{ij} and ϵ_{ij} are the stress and strain tensors, respectively. In an orthorhombic lattice, the zero-pressure elastic constants C_{ij} and the non-zero-pressure elastic constants $\tilde{C}_{ij}$ evaluated at the current stressed state are related via [139] $\tilde{C}_{\alpha\alpha} = C_{\alpha\alpha} - P$; α=1,2,..,6; $\tilde{C}_{12} = C_{12} - P$; $\tilde{C}_{13} = C_{13} - P$; $\tilde{C}_{23} = C_{23} - P$, where P is the hydrostatic pressure. Note that at zero pressure, the C_{ij} and $\tilde{C}_{ij}$ are equal [140]. The well-known Born stability conditions [131] can be shown to be valid for both the zero-stress case (using C_{ij}) and the non-zero-stress case (using $\tilde{C}_{ij}$) [140]. For a stable orthorhombic structure, the nine independent elastic constants should satisfy the following Born criteria [131]:

$$\begin{aligned} &\tilde{C}_{ii} > 0; \tilde{C}_{11}\tilde{C}_{22} > \tilde{C}_{12}^2; \\ &\tilde{C}_{11}\tilde{C}_{22}\tilde{C}_{33} + 2\tilde{C}_{12}\tilde{C}_{13}\tilde{C}_{23} - \\ &\tilde{C}_{11}\tilde{C}_{23}^2 - \tilde{C}_{22}\tilde{C}_{13}^2 - \tilde{C}_{33}\tilde{C}_{12}^2 > 0. \end{aligned} \tag{3.3.10}$$

Bulk elastic properties: bulk modulus B and shear modulus G were calculated from the elastic constants using Voigt-Reuss-Hill averaging schemes [132, 133, 134], using the following formulas for an orthorhombic crystal

$$B_V = \frac{1}{9}\left[\tilde{C}_{11}+\tilde{C}_{22}+\tilde{C}_{33}\right] + \frac{2}{9}\left[\tilde{C}_{12}+\tilde{C}_{13}+\tilde{C}_{23}\right], \tag{3.3.11}$$

$$G_V = \frac{1}{15}\left[\tilde{C}_{11}+\tilde{C}_{22}+\tilde{C}_{33}-\tilde{C}_{12}-\tilde{C}_{13}-\tilde{C}_{23}\right] + \frac{1}{5}\left[\tilde{C}^*\right]. \tag{3.3.12}$$

The crystal shear anisotropy factors A_1 in $\{100\}$ planes between $\langle 011\rangle$ and $\langle 010\rangle$ directions, A_2 in $\{010\}$ planes between $\langle 101\rangle$ and $\langle 001\rangle$ directions and A_3 in $\{001\}$ planes between $\langle 110\rangle$ and $\langle 010\rangle$ directions are defined as [135, 136]

$$\begin{aligned} A_1 &= \frac{4\tilde{C}_{44}}{\tilde{C}_{11}+\tilde{C}_{33}-2\tilde{C}_{13}}; A_2 = \frac{4\tilde{C}_{55}}{\tilde{C}_{22}+\tilde{C}_{33}-2\tilde{C}_{23}}; \\ A_3 &= \frac{4\tilde{C}_{66}}{\tilde{C}_{11}+\tilde{C}_{22}-2\tilde{C}_{12}}. \end{aligned} \tag{3.3.13}$$

3.3.2 Dynamical Stability

Phonons play essential roles in dynamical behaviors and thermal properties of materials. During the vibration, the atoms move from their equilibrium positions $\mathbf{r}(lk)$ to a new position $\mathbf{R}(lk) = \mathbf{r}(lk) + \mathbf{u}(lk)$, where $\mathbf{u}(lk)$ is the displacement, l and k are the labels of unit cells and atoms in each unit cell, respectively. Crystal potential energy Φ is assumed to be an analytic function of the displacements of the atoms, and Φ can be expanded around the equilibrium position as

$$\Phi = \Phi_0 + \sum_{lk}\sum_{\alpha}\Phi_\alpha(lk)u_\alpha(lk) + \frac{1}{2}\sum_{ll'kk'}\sum_{\alpha\beta}\Phi_{\alpha\beta}(lk,l'k')u_\alpha(lk)u_\beta(l'k') + ..., \tag{3.3.14}$$

where α, β, ... are the Cartesian indices. The coefficients of the Taylor series expansion in equation (3.3.14) are the equilibrium, first and second-order force constants, respectively. If the atoms make small displacements at constant volume, the atomic vibrations problem is solved with the second-order terms as in the harmonic approximation, ignoring the higher terms in equation (3.3.14) [141].

In the harmonic approximation, the dynamical property of atoms is obtained by solving eigenvalue problem of dynamical matrix $D(\mathbf{q})$,

$$\sum_{\beta k'} D^{\alpha\beta}_{kk'}(\mathbf{q})e^{\beta k'}_{\mathbf{q}j} = \omega^2_{\mathbf{q}j}e^{\alpha k}_{\mathbf{q}j}, \tag{3.3.15}$$

with

$$D^{\alpha\beta}_{kk'}(\mathbf{q}) = \sum_{l'}\frac{\Phi_{\alpha\beta}(0k,l'k')}{\sqrt{m_k m_{k'}}}e^{i\mathbf{q}.[\mathbf{r}(l'k')-\mathbf{r}(0k)]}, \tag{3.3.16}$$

where m_k is the mass of the atom k, $\mathbf{q}$ is the wave vector, and j is the band index. $\omega_{\mathbf{q}j}$

and $e_{\mathbf{q}j}$ give the phonon frequency and polarization vector of the phonon mode labelled by a set $\{\mathbf{q}, j\}$, respectively. Solving equation (3.3.15) yields the phonon mode $\omega_{\mathbf{q}j}$. Under the harmonic approximation, the structure is said to be dynamically stable if its all phonon modes have positive frequencies for all wave vectors [131].

Once the phonon modes over Brillouin zone (BZ) are known, the energy of phonon system is given by

$$E^* = \sum_{\mathbf{q}j} \hbar\omega_{\mathbf{q}j} \left[\frac{1}{2} + \frac{1}{\exp(\omega_{\mathbf{q}j}/k_{\mathrm{B}}T) - 1}\right], \tag{3.3.17}$$

where k_{B}, $\hbar$ and T are the Boltzmann constant, the reduced Planck constant and the temperature, respectively. The phonon contributions to the thermal properties at constant volume such as heat capacity C_{v}, entropy S and Helmholtz free energy F can be computed as functions of temperature using thermodynamic relations [141, 142]:

$$C_{\mathrm{v}} = \sum_{\mathbf{q}j} k_{\mathrm{B}} \left(\frac{\hbar\omega_{\mathbf{q}j}}{k_{\mathrm{B}}T}\right)^2 \frac{\exp(\hbar\omega_{\mathbf{q}j}/k_{\mathrm{B}}T)}{\left[\exp(\hbar\omega_{\mathbf{q}j}/k_{\mathrm{B}}T) - 1\right]^2}, \tag{3.3.18}$$

$$S = \frac{1}{2T} \sum_{\mathbf{q}j} \hbar\omega_{\mathbf{q}j} \coth[\hbar\omega_{\mathbf{q}j}/2k_{\mathrm{B}}T] - k_{\mathrm{B}} \sum_{\mathbf{q}j} \ln[2\sinh(\hbar\omega_{\mathbf{q}j}/2k_{\mathrm{B}}T)], \tag{3.3.19}$$

and

$$F = \frac{1}{2} \sum_{\mathbf{q}j} \hbar\omega_{\mathbf{q}j} + k_{\mathrm{B}}T \sum_{\mathbf{q}j} \ln[1 - \exp(-\hbar\omega_{\mathbf{q}j}/k_{\mathrm{B}}T)]. \tag{3.3.20}$$

In first-principles calculations the phonon dispersion can be computed using finite displacement method (FDM) or the density functional perturbation theory (DFTP) [143, 144]. In this work, phonon properties were computed using a finite displacement method at the level of harmonic approximation. Initially, force constants (acting due to small displacements of the atoms) of $CH_3NH_3XI_3$ (X = Pb, Sn) ($CsPbI_3$) were calculated from a $2 \times 2 \times 2$ ($2 \times 4 \times 1$) supercell containing 384 (160) atoms using VASP code. Then, using the phonopy code [141], the elements of the dynamical matrix are constructed to solve the eigenvalue problem for phonon frequencies at high-symmetry k-points.

3.4 Electronic Density of States (DOS)

The electronic density of states (DOS) as a function of energy is a very useful concept in analyzing the band structure of solids [145]. It holds the properties of the band

structure for all possible positions in reciprocal space (k-points) into a simple form. The density of states $g(\varepsilon)$ is defined as the number of electronic states in a unit volume per unit energy. In the energy range (ε, $\varepsilon+d\varepsilon$), the density of states $g(\varepsilon)$ can be given by a sum over all states with energy in that range [105].

Generally, the density of states (DOS) can be expressed as following [145]

$$g(\varepsilon) = \frac{2}{(2\pi)^3} \sum_i \int \mathrm{d}\mathbf{k} \delta(\varepsilon - \varepsilon_{i,\mathbf{k}}), \tag{3.4.1}$$

where i is the band index. The integral is over all k-points in the Brillouin zone, while the factor of two accounts for spin up and spin down, and $\delta(\varepsilon - \varepsilon_{i,\mathbf{k}})$ is the step function. The Fermi energy is defined by $I(\varepsilon_F) = N$, where N represents the number of electrons per unit cell and $I(\varepsilon)$ is the number of states. The DOS can be defined as the energy derivative of $I(\varepsilon)$ as

$$g(\varepsilon) = \frac{\mathrm{d}I(\varepsilon)}{\mathrm{d}\varepsilon}, \tag{3.4.2}$$

with the normalization

$$N = \int_{-\infty}^{E_F} g(\varepsilon)\mathrm{d}\varepsilon. \tag{3.4.3}$$

Fermi energy ε_F can be obtained from equation (3.4.1) and (3.4.3) [146].

In VASP, it is easier to calculate density of states from equation (3.4.3) [105]

$$g(\varepsilon_i) = \frac{I(\varepsilon) - I(\varepsilon_{i-1})}{\Delta\varepsilon}, \tag{3.4.4}$$

where $\Delta\varepsilon$ is the energy difference between any two grid points. It is relevant to express the relative contribution of each atom to the total density of states (TDOS), this can be done by calculating the projected (or partial) density of states (PDOS) for each atom.

3.5 Electronic Transport Properties

The calculations of the electronic transport properties of the optimized structure (obtained from the above-mentioned DFT calculations) were performed using the Boltzmann transport theory [114] (described in Chapter 2 (Section 2.6)) within the constant relaxation time approximation as implemented in the BoltzWann code [116]. Fillippetti et al. [147] have obtained relaxation time of $\sim 10fs$ estimated using numerical method

at room temperature, based on this finding we assume τ=10fs in this work, which is commonly used for studying semiconductors [148]. The code uses a maximally-localized Wannier functions (MLWFs) [149] basis set to interpolate the bandstructure obtained from the above-mentioned DFT calculations. After using a $6 \times 4 \times 4$ **k**-points for the construction of the MLWFs, we have used a dense $(40 \times 40 \times 40)$ mesh of **k**-points for wave functions to reconstruct the density distribution of all electrons, which is required due to the steepness of Fermi-Dirac distribution near the Fermi energy [116]. Then we calculate the electronic transport properties such as Seebeck coefficient S, electrical conductivity σ, electronic thermal conductivity κ_e and the power factor $S^2\sigma$. The computation of MLWFs has been performed with WANNIER90 package [150]. The electronic transport properties of $CH_3NH_3PbI_3$ have computed for chemical potentials ranging from -2 eV to 3 eV (the Fermi level is set at 0 eV).

3.6 Lattice Thermal Conductivity

The lattice thermal conductivities κ_L were calculated within the single-mode relaxation-time (SMRT) approximation and linearized phonon Boltzmann equation (described in Chapter 2 (Section 2.7)) as implemented in Phono3py [151]. For the third-order interatomic force constants of $CH_3NH_3PbI_3$ ($CsPbI_3$) were calculated from a $2 \times 2 \times 2$ $(2 \times 4 \times 1)$ supercell containing 384 (160) atoms, and reciprocal spaces of the supercells were sampled by $2 \times 2 \times 2$ meshes. A supercell method and finite displacement method were used to calculate force constants. Phono3py code [151] generates the structures with a pair of displaced atoms in each displaced configuration in the supercell, and VASP code was used to calculate forces in supercells. When the VASP calculations are complete, phono3py software collects the forces and generates 2^{nd} and 3^{rd} order force constants. To compute lattice thermal conductivity, the reciprocal spaces of the primitive cells were sampled using $8 \times 8 \times 8$ and $8 \times 16 \times 4$ meshes for $CH_3NH_3PbI_3$ and $CsPbI_3$, respectively, which was sufficient for convergence of the lattice thermal conductivity.

3.7 GW and BSE Calculations Detail

The optical properties are in general evaluated with the help of the frequency-dependent complex dielectric function $\varepsilon(\omega) = \varepsilon_{\mathrm{re}}(\omega) + i\varepsilon_{\mathrm{im}}(\omega)$ (see appendix D). In order to obtain optical spectra, we carried out Bethe-Salpeter Equation (BSE) calculations beyond the Tamm Dancoff approximation [152] on top of non-self-consistent G_0W_0 [109, 153] calculations. For $CH_3NH_3PbI_3$ we use 2016 bands with an energy cut-off of 300 eV and an energy cut-off of 120 eV for the plane wave basis of the response function and 48 frequency grid points for the energy integration. For $CsPbI_3$ we use 2016 bands with an energy cut-off of 300 eV and an energy cut-off of 120 eV for the plane wave basis of the response function and 48 frequency grid points for the energy integration. For $CH_3NH_3SnI_3$ we use 4008 bands with an energy cut-off of 300 eV and an energy cut-off of 150 eV for the plane wave basis of the response function and 48 frequency grid points for the energy integration.

3.8 Microscopic Dielectric

The microscopic dielectric function ε can be obtained directly from ab-initio calculations. The macroscopic dielectric function $\varepsilon_{\mathrm{mac}}$ (can be measured experimentally) is therefore can be obtained by inverting the full microscopic dielectric matrix ε and taking the limit $\mathbf{q} \to 0$ of the resulting matrix:

$$\frac{1}{\varepsilon_{\mathrm{mac}}(\hat{\mathbf{q}}, \omega)} = \lim_{\mathbf{q}\to 0} \varepsilon^{-1}_{\mathbf{G}=0,\mathbf{G}'=0}(\mathbf{q}, \omega), \tag{3.8.1}$$

then invert this 3×3 tensor. Where $\varepsilon_{\mathbf{G}\mathbf{G}'}(\mathbf{q}, \omega) := \varepsilon(\mathbf{q} + \mathbf{G}, \mathbf{q} + \mathbf{G}', \omega)$ is the Fourier transform to reciprocal space of $\varepsilon(\mathbf{r}, \mathbf{r}')$, $\mathbf{G}$ is a reciprocal lattice vector and $\mathbf{q}$ belongs to the first Brillouin zone. If the off-diagonal elements of the dielectric matrix are vanished, that is, the local field effects, the macroscopic dielectric function can be approximated by taking the limit of the microscopic dielectric matrix [154]:

$$\varepsilon_{\mathrm{mac}(\hat{\mathbf{q}},\omega)} \approx \lim_{\mathbf{q}\to 0} \varepsilon_{00}(\mathbf{q}, \omega). \tag{3.8.2}$$

Once the macroscopic dielectric function $\varepsilon_{\mathrm{mac}}$ is known, we can derive all the desired frequency-dependent optical spectra as we can see in Section (3.9).

3.9 Optical Spectra Calculations

Using the real part $\varepsilon_{\rm re}(\omega)$ and the imaginary part $\varepsilon_{\rm im}(\omega)$ of the dielectric function $\varepsilon(\omega)$ we can derive all the desired frequency-dependent optical spectra such as absorption coefficient $\alpha(\omega)$, refractive index $n(\omega)$, reflectivity $R(\omega)$ and energy loss $L(\omega)$ using the following mathematical expressions [122, 155, 156].

$$\alpha(\omega) = \sqrt{2}\omega\left([\varepsilon_{\rm re}^2(\omega)+\varepsilon_{\rm im}^2(\omega)]^{\frac{1}{2}}-\varepsilon_{\rm re}(\omega)\right)^{\frac{1}{2}}, \tag{3.9.1}$$

$$n(\omega) = \frac{1}{\sqrt{2}}\left([\varepsilon_{\rm re}^2(\omega)+\varepsilon_{\rm im}^2(\omega)]^{\frac{1}{2}}+\varepsilon_{\rm re}(\omega)\right)^{\frac{1}{2}}, \tag{3.9.2}$$

$$R(\omega) = \left|\frac{[\varepsilon_{\rm re}(\omega)+j\varepsilon_{\rm im}(\omega)]^{\frac{1}{2}}-1}{[\varepsilon_{\rm re}(\omega)+j\varepsilon_{\rm im}(\omega)]^{\frac{1}{2}}+1}\right|^2, \tag{3.9.3}$$

$$L(\omega) = \frac{\varepsilon_{\rm im}(\omega)}{\varepsilon_{\rm re}^2(\omega)+\varepsilon_{\rm im}^2(\omega)}. \tag{3.9.4}$$

4

Results and Discussions

4.1 Methylammonium Lead Triiodide Perovskite

The focus of this section is to investigate the structural, mechanical and dynamical stabilities, electronic, lattice thermal conductivity, transport and optical properties of orthorhombic structure $CH_3NH_3PbI_3$ based on the theoretical methods (introduced in Chapter 2) and computational details (described in Chapter 3), our obtained results are presented and discussed. The results on this section have been published [1, 2, 3, 4].

4.1.1 Structural Properties

The experimental lattice constants are a = 8.836 $\mathring{A}$ b = 12.58 $\mathring{A}$ and c = 8.55 $\mathring{A}$. Its structure has been determined through single X-ray diffraction analysis [35]. We first present the calculated total binding energy against cell volume for the studied structure under the generalized gradient approximation PBE and PBEsol to find the most suitable method for this material. We obtained the equation of states by means of the Murnaghan equation of states (EOS) [126] as presented in Figure (4.1). The corresponding equilibrium lattice parameters, cohesive energy (E_{coh}) and cell volume (V_0) compared with the other theoretical and experimental results are summarized in Table (4.1), showing that the results of PBEsol have good agreement with the experimental results [35] as compared to the result obtained by PBE. The relative error with respect to the experimental value on the lattice parameters does not exceed 3%.

Table 4.1: Calculated and experimental equilibrium parameters of the orthorhombic $CH_3NH_3PbI_3$: Lattice constants (a(Å), b(Å), c(Å)), equilibrium volume V_0(Å^3) and cohesive energy $E_{\rm coh}$ (eV/atom).

Method/Functional	a(Å)	b(Å)	c(Å)	V_0(Å^3)	$E_{\rm coh}$(eV/atom)
PBE	9.346	12.908	8.581	1034	-3.07
PBEsol	9.062	12.632	8.364	957.44	-3.06
PBE+D2[a]	8.871	13.125	8.636	1005.5	-
vdWDF[b]	8.831	12.648	8.570	957.18	-
Experiment[c]	8.836	12.580	8.555	951.01	-
Experiment[d]	8.87	12.63	8.58	961.20	-

[a]Ref. [42] [b]Ref. [40] [c]Ref. [35] [d]Ref. [36]

The cohesive energy $E_{\rm coh}$ is defined as the negative of the energy that must be supplied to the solid to separate its constituents into neutral free atoms at rest and at infinite separation [105]. From Table (4.1), the calculated negative cohesive energies indicate that the $CH_3NH_3PbI_3$ compound in the orthorhombic phase is energetically stable. From Table (4.1), previously calculated lattice constants including van der Waals (vdW) interactions [40] and DFT+D2 implementation [42] are presented. We see that our present theoretical results are consistent with experimental results.

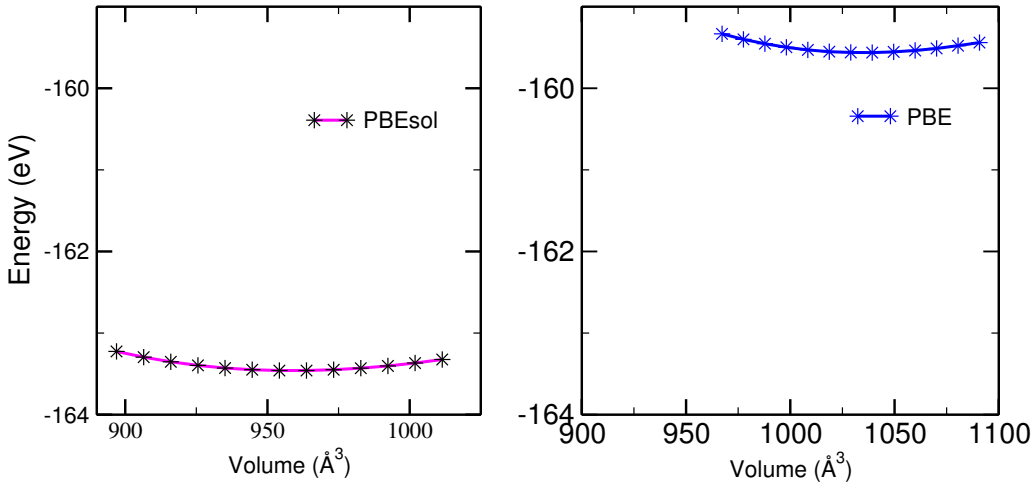


Figure 4.1: (Color online) Energy-volume equation of states using PBE and PBEsol for the orthorhombic $CH_3NH_3PbI_3$.

4.1.2 Mechanical Stability

The elastic constants of the orthorhombic $CH_3NH_3PbI_3$ were calculated using PBE and PBEsol functionals. The calculated values of the elastic constants along with available theoretical values are given in Table (4.2). The calculated elastic constants are comparable with the other theoretical values [42]. Our results show that the elastic constant C_{11} is smaller than C_{33} and larger than C_{22} for $CH_3NH_3PbI_3$ orthorhombic crystal, implying it is mechanically anisotropic. The mechanical stability for $CH_3NH_3PbI_3$ orthorhombic crystal was obtained by checking that all the elastic constants are positive and satisfy the Born conditions [131] for orthorhombic structures. From the obtained results, one can confirm that the structure is mechanically stable against the influence of external forces.

Table 4.2: PBE and PBEsol calculated independent elastic constants C_{ij} for the orthorhombic $CH_3NH_3PbI_3$ in (GPa) compared other theoretical study (PBE+D2).

Functional	C_{11}	C_{12}	C_{13}	C_{22}	C_{23}	C_{33}	C_{44}	C_{55}	C_{66}
PBE	23.14	11.52	10.18	22.64	09.78	31.13	05.13	04.32	10.31
PBEsol	28.37	12.63	11.35	21.00	09.73	37.67	05.37	04.95	11.16
PBE+D2 [42]	27.80	11.70	17.40	20.50	20.20	24.80	03.00	09.80	06.30

Table 4.3: The calculated bulk moduli (B_R, B_V, B_H in GPa), shear moduli (G_R, G_V, G_H in GPa), Young's modulus for the orthorhombic $CH_3NH_3PbI_3$ (E in GPa), and the other theoretical study.

Functional	B_R	B_V	B_H	G_R	G_V	G_H	E_H
PBE	15.36	15.54	15.45	06.20	06.98	06.59	17.31
PBEsol	16.36	17.16	16.76	06.79	07.85	07.32	19.17
PBE+D2 [42]	-	-	18.10	-	-	03.60	15.00

Table 4.4: The calculated B/G ratio, Poisson's ratio (ν), the shear anisotropic factors (A_1, A_2, A_3) for the orthorhombic $CH_3NH_3PbI_3$, with the corresponding theoretical study.

Functional	B/G	ν	A_1	A_2	A_3
PBE	02.34	0.31	0.60	0.59	1.81
PBEsol	02.29	0.31	0.50	0.51	1.84
PBE+D2 [42]	03.00	0.36	0.67	8.00	1.01

Under Voigt-Reuss approximation, the bulk modulus, shear modulus can be described by equations (3.3.3) and (3.3.5) for an anisotropic crystal according to Hill approximation, the bulk modulus, shear modulus are given by equation (3.3.6). From the calculated bulk modulus and shear modulus one can estimate the Young's modulus E, and Poisson's ratio, ν using equation (3.3.7). The calculated elastic moduli for $CH_3NH_3PbI_3$ orthorhombic crystal using Voigt-Reuss-Hill approximations with other reported theoretical values are listed in Table (4.3). The differences in the values presented in Table (4.2) and (4.3) can be attributed to the different exchange-correlation functional and pseudopotentials used.

The bulk modulus B_H is an average of bulk modulus B_V and bulk modulus B_R, will be used as a measure of the average atomic bond strength of materials because it has a strong correlation with binding energy of atoms in crystal [157]. It is obvious from Table (4.3), that the calculated bulk modulus of orthorhombic perovskite $CH_3NH_3PbI_3$ is about 15.45 GPa and 16.76 GPa using PBE and PBEsol functional respectively. Comparing the results calculated from Table (4.3), with the values calculated from other work [42]. The differences in the values presented in Table (4.3) are due to the different approximations used. The shear anisotropic factors obtained from equation (3.3.8) along with the other theoretical ones are given in Table (4.4). From the criterion for brittleness and ductility of materials based on the ratio B/G related to the critical value 1.75 [158], the ratio $B/G < 1.75$ indicates that the crystal is brittle and if the ratio $B/G > 1.75$ indicates that the crystal is ductile. The present B/G ratio 2.34 and 2.29 with PBE and PBEsol, respectively suggest that this material has ductile property. For an isotropic crystal, the A_1, A_2 and A_3, should be equal one, while any deviation from one indicates the degree of elastic anisotropy possessed by the crystal.

4.1.3 Dynamical Stability

As a further examination of the stability of the investigated structure, phonon modes of the optimized structure was calculated in the Brillouin zone using finite displacement method as implemented in Phonopy [141] package. The calculated phonon bandstructure of $CH_3NH_3PbI_3$ in an orthorhombic system is represented in Figure (4.2). It can be seen from this figure that all phonon modes are positive throughout the Brillouin zone of the structure, therefore, the relaxed system is dynamically stable under small distortions.

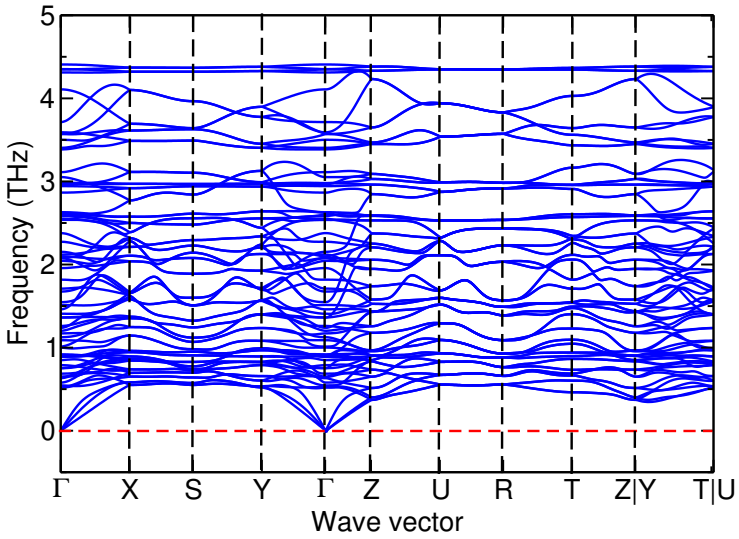


Figure 4.2: (Color online) Low-frequency regions of the calculated phonon dispersion relation of $CH_3NH_3PbI_3$ using PBEsol (the full vibrational frequency spectra spans up to 100 THz).

The heat capacity at constant volume C_v is calculated from the phonon contribution to the thermal properties as explained in Subsection (3.3.2). The heat capacity at constant volume C_v as a function of temperature is shown in Figure (4.3) in the temperature range from 0 K to 300 K. Since the orthorhombic phase $CH_3NH_3PbI_3$ is stable at low temperature, the inset graph shows heat capacity up to 150 K.

4.1.4 Electronic Properties

In this work, by using the optimized lattice constants, the Kohn-Sham band structure of the studied material was calculated using the PBEsol functional along high symmetry k-points, both the valence band maximum (VBM) and conduction band minimum (CBM) were found to be located at the gamma Γ point of the Brillouin zone (BZ), hence the investigated material has a direct band gap semiconductor character at the gamma Γ point. The calculated electronic band structure of $CH_3NH_3PbI_3$ orthorhombic phase along the high symmetry directions in the Brillouin zones between -4 eV and 6 eV is shown in Figure (4.4). The Fermi level is shifted to zero and is shown by the horizontal dashed line. Since the Fermi level is closer to the VBM this indicates $CH_3NH_3PbI_3$ is a *p*-type semiconductor. Our calculated, reported theoretical and experimental electronic band-gap of the $CH_3NH_3PbI_3$ orthorhombic phase are listed in Table (4.5). From this table we note that our calculated electronic gaps are 1.80 eV and 1.57 eV, at Γ point

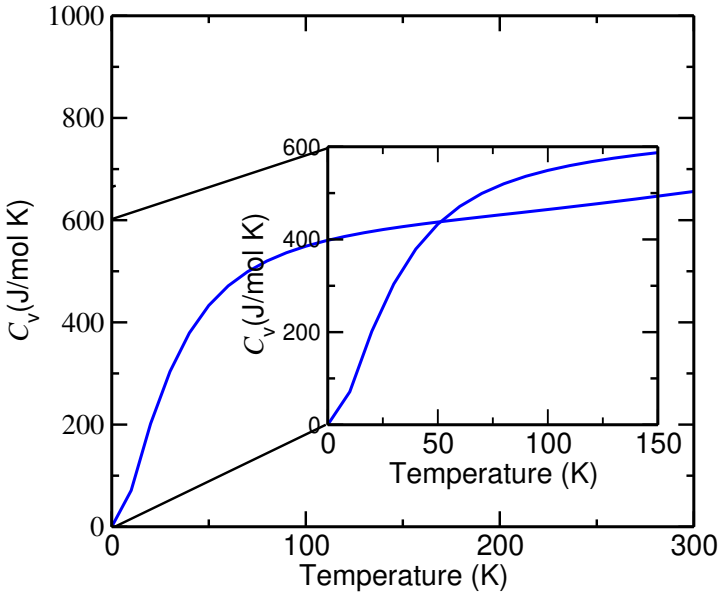


Figure 4.3: The heat capacity at constant volume as a function of temperature for the orthorhombic $CH_3NH_3PbI_3$. The inset shows specific heat C_v when temperature goes from 0 K up to 150 K.

by PBE and PBEsol, respectively. However, the experimental band gap is 1.61 eV [35], which indicates good agreement between our results with experiment, especially PBEsol calculations. It should also noted that the electronic gap obtained from PBEsol calculation deviate ~ 0.04 eV from the corresponding experimental [35]. It is well known that KS-DFT seriously underestimate the band gap. The solution to this problem are the use of hybrid functionals or many body approach, that with an increase of the computational demanding.

Density of states (DOS) describes the electron probability distribution in energy spectrum. Figure (4.4) shows the total density of states (TDOS) and the projected density of states (PDOS) for the investigated structure using the PBEsol functional. It can be seen that around the fundamental band gap, only iodine I and lead Pb contribute to the DOS. Also the organic cation $CH_3NH_3^+$ makes little contribution to the top valence band maximum (VBM) and bottom conduction band minimum (CBM), therefore, the contribution of organic cation $CH_3NH_3^+$ to the Fermi level region is very weak. This finding is consistent with the previous theoretical studies [159, 160].

Because of the presence of heavy metals, namely lead Pb and I iodine, in the structure of this material, spin-orbit coupling (SOC) can have an effect on the band gap by splitting

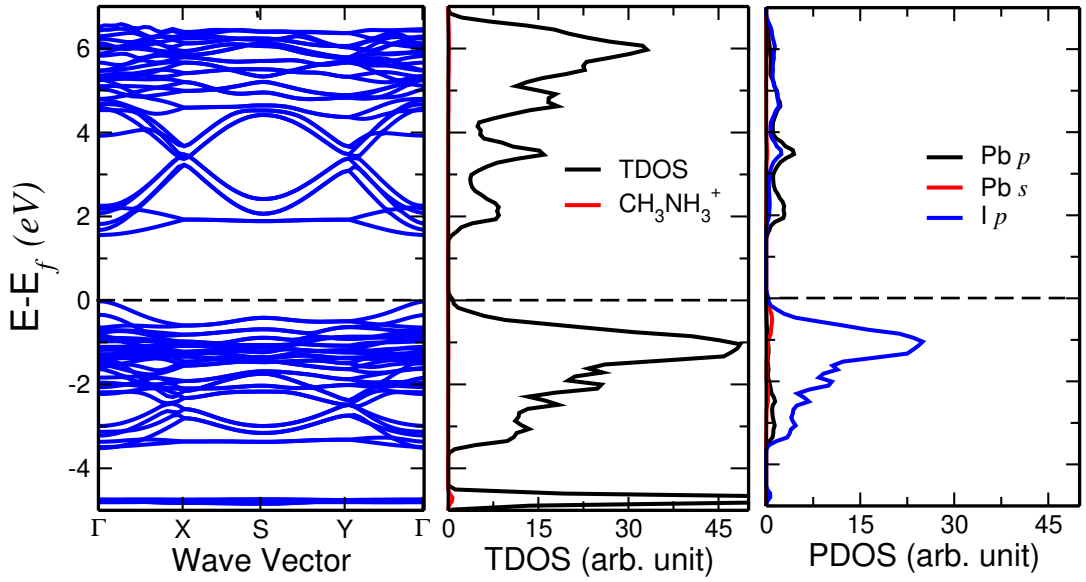


Figure 4.4: (Color online) DFT calculated electronic structure of the orthorhombic $CH_3NH_3PbI_3$: band structure (left), total density of states (TDOS) and $CH_3NH_3^+$ cation projected density of states PDOS (middle), and Pb and I atomic orbital PDOS.

Table 4.5: Our calculated, reported experimental electronic band gap of the orthorhombic $CH_3NH_3PbI_3$.

Method	PBE	PBEsol	SOC	GW	BSE			Exp.[35]	Theory [40]
					a	b	c		
Band gap (eV)	1.80	1.57	0.46	2.66	2.00	2.16	1.88	1.61	1.74

the energy levels, mainly in the conduction band; hence, closing the band gap [161]. On the other hand, the band gap opening in the GW approach is due to the Quasi-particle (QP) corrections. That is, due to the coulomb screening effect, which is only well described by the self-energy operator [109]. Both trends are well-known in the literature [41, 61, 162]. Therefore, the impact of the SOC on the electronic properties at the DFT level was also investigated. The band structure of $CH_3NH_3PbI_3$ structure with SOC is reported in Figure (4.5). At room temperature, the experimental band gap of such material was found to be 1.61 eV [35]. The PBEsol calculations without (with) SOC predict a band-gap of 1.57 (0.46) eV, while the GW approximation without SOC estimates the band gap to be 2.66 eV. Therefore, the effect of SOC in the PBEsol calculation reduces the band-gap by 1.11 eV, down to 0.46 eV, which is lower than the experimental value, while the GW approximation without SOC overestimates the band gap by about 1.05 eV. Our results of the effects of the SOC on the band gap at DFT level agree well with results reported [162, 41] for the cubic phase and [61] for the

tetragonal phase.

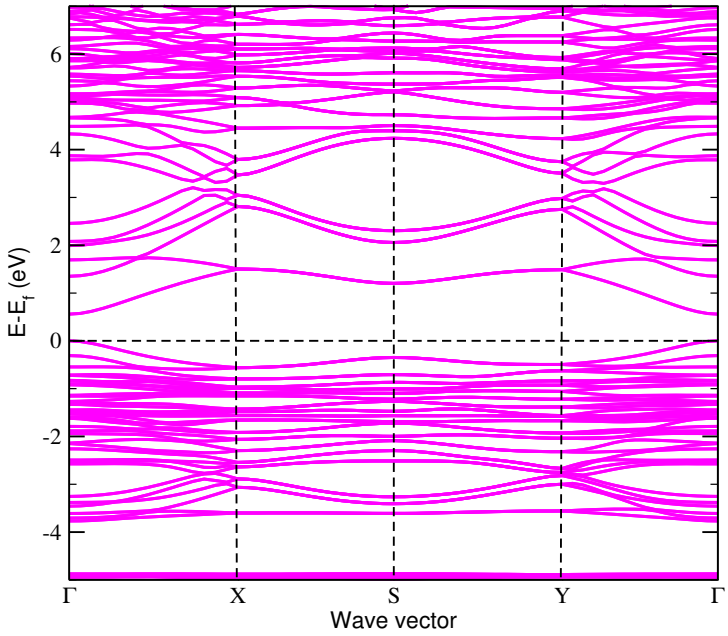


Figure 4.5: (Color online) DFT calculated band structure of the orthorhombic $CH_3NH_3PbI_3$ using PBEsol including spin orbit-coupling (SOC).

4.1.5 Lattice Thermal Conductivity

The lattice thermal conductivity κ_L is a very important quantity, which significantly affects thermoelectric material performance. A good thermoelectric material must have low thermal conductivity, as ZT is inversely depend on κ (κ is the total thermal conductivity). Using the phono3py code [151], the calculated lattice thermal conductivity κ_L for $CH_3NH_3PbI_3$ in an orthorhombic phase is shown as functions of temperature in Figure (4.6), where temperature goes from 0 K to 300 K. Moreover, the lattice thermal conductivity for $CH_3NH_3PbI_3$ in an orthorhombic phase is given in Table (4.6) between 50 K and 150 K. The calculated results show low lattice thermal conductivity, and the corresponding lattice thermal conductivity at 150 K was found to be 0.189, 0.138, and 0.530 $Wm^{-1}K^{-1}$ in the a-, b- and c-directions, respectively. The obtained value in the c-direction is significantly larger than those values in the a, b plane. At 150 K, the ratios $\kappa_L(c)/\kappa_L(b) = 3.84$ and $\kappa_L(c)/\kappa_L(a) = 2.80$, indicate high anisotropic behaviour of the structure. As can be seen from Table (4.6), the lattice thermal conductivities in the a-, b- and c-directions decrease with increase of temperature. Additionally, the

Table 4.6: The calculated lattice thermal conductivity ($Wm^{-1}K^{-1}$) in the a-, b- and c-directions with the corresponding average values for the orthorhombic $CH_3NH_3PbI_3$.

T (K)	$\kappa_L(a)$	$\kappa_L(b)$	$\kappa_L(c)$	κ_L(avg)
50	0.294	0.290	0.522	0.340
100	0.206	0.178	0.475	0.286
150	0.189	0.138	0.530	0.286

average lattice thermal conductivity $\kappa_L(\text{avg}) = [\kappa_L(a)+\kappa_L(b)+\kappa_L(c)]/3$ at different temperatures are also shown in Table (4.6). Andrea et al. [43], experimentally, reported ultra-low lattice thermal conductivity for single crystals and polycrystalline samples of $CH_3NH_3PbI_3$. They found the room temperature value of κ_L to be 0.5 $Wm^{-1}K^{-1}$ for single crystals and 0.3 $Wm^{-1}K^{-1}$ for polycrystalline. Our predictions for κ_L also show good agreement with these experimental results [43]. The theoretical study using density functional theory (DFT) by Xin Qian et al. [45] found a very low thermal conductivity (0.59 $Wm^{-1}K^{-1}$) for the tetragonal phase of $CH_3NH_3PbI_3$ at room temperature, and higher thermal conductivity for the pseudocubic phase of $CH_3NH_3PbI_3$ (1.80 $Wm^{-1}K^{-1}$) at 330 K. Also, theoretically, ultra-low lattice thermal conductivity in Pb based perovskites have been predicted, such as $CsPbI_3$ (0.25 $Wm^{-1}K^{-1}$) [32].

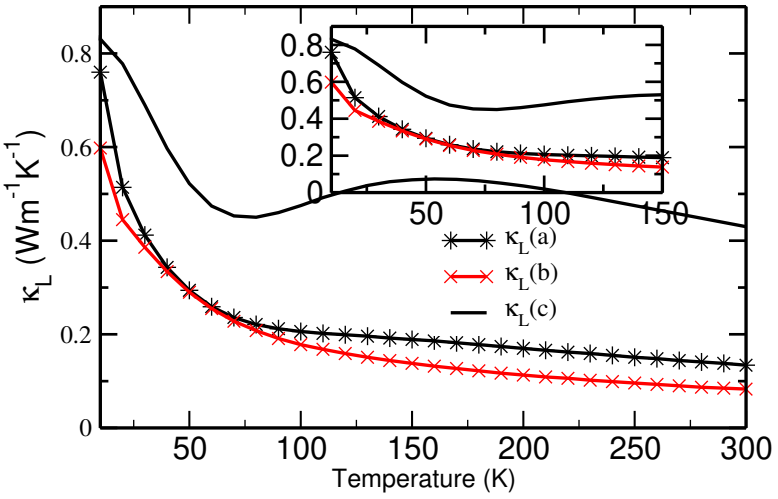


Figure 4.6: (Color online) The calculated lattice thermal conductivity ($Wm^{-1}K^{-1}$) in the a-, b- and c-directions for the orthorhombic $CH_3NH_3PbI_3$.

In order to understand the lattice thermal conductivity of $CH_3NH_3PbI_3$, we explore the phonon-related properties such as phonon group velocities and phonon lifetimes. The phonon group velocities and lifetimes are shown in Figure (4.7). To provide a reference point, we have performed the same calculations on the inorganic perovskite $CsPbI_3$ in an orthorhombic phase, with the results compared in Figure (4.20) in sub-section (4.2.5). For the orthorhombic $CH_3NH_3PbI_3$ our calculated phonon lifetimes at 150 K was found to be 6 ps, agree well with experimental results 5.4 ps reported for the orthorhombic phase at 140 K from inelastic neutron scattering [163].

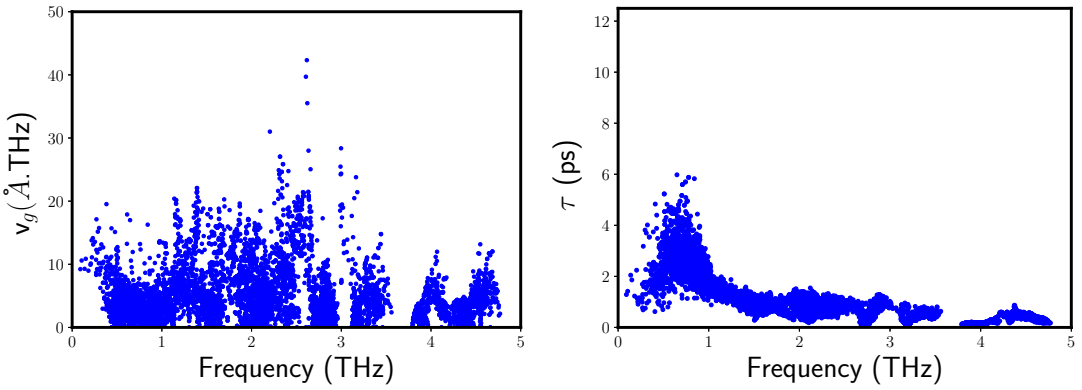


Figure 4.7: (Color online) The phonon group velocities (Left) and the phonon lifetimes (Right) for the orthorhombic $CH_3NH_3PbI_3$ at 150 K in the first Brillouin zone.

4.1.6 Electronic Transport Properties

For good thermoelectric material, figure of merit ZT is equal to or larger than unity [164]. To estimate the value of ZT for orthorhombic perovskite $CH_3NH_3PbI_3$, the thermoelectric (TE) properties of orthorhombic perovskite $CH_3NH_3PbI_3$ were calculated using the BoltzWann code in the constant relaxation time approximation at low temperature. The calculated properties were plotted in Figures (4.8) to (4.12) as a function of chemical potential (μ) at 50 K, 100 K and 150 K, for the calculation of ZT, we first investigate the Seebeck coefficient S, then the electrical conductivity σ and the electronic thermal conductivity κ_e are discussed. Followed by the power factor $S^2\sigma$, finally, calculated values of figure of merit ZT are given.

In the Seebeck effect the temperature difference between two different materials creates a potential difference. Free electrons move towards the lower temperature region from

the higher temperature region [165]. The variation in the calculated Seebeck coefficients with respect to the chemical potential (μ) in a-, b- and c-directions for $CH_3NH_3PbI_3$ compound at different temperatures are presented in Figure (4.8). From Figure (4.8) it is clear that the Seebeck coefficient has positive values at chemical potential $\mu = 0$ indicating that it is a p-type semiconductor. In the c-direction the Seebeck coefficient almost remained constant from 50 K to 150 K.

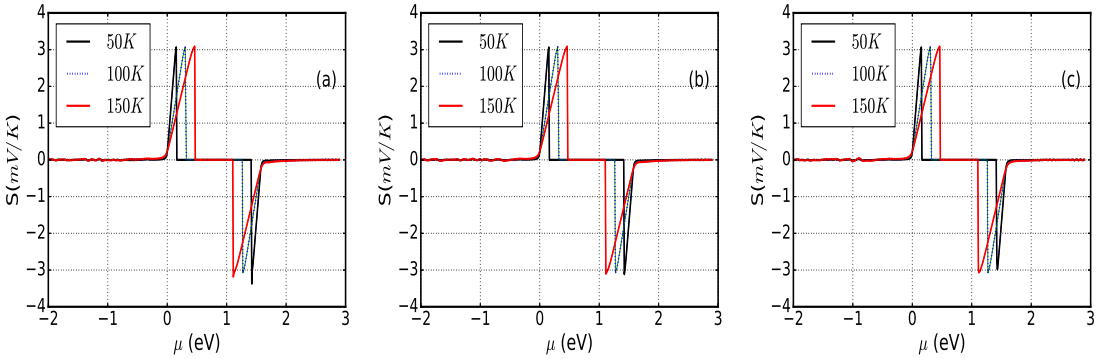


Figure 4.8: (Color online) Variation of Seebeck coefficient with respect to chemical potential μ for the orthorhombic $CH_3NH_3PbI_3$ at different temperatures in the (a) a-direction, (b) b-direction, and (c) c-direction.

The variation of the electrical conductivity σ with chemical potential μ at different temperatures given in Figure (4.9). The electrical conductivity exhibits similar trend at all temperatures. The value of electrical conductivity increases with increase in chemical potential μ at all temperatures with the highest value 4.58×10^6 $\Omega^{-1}\mathrm{m}^{-1}$ in the c-direction at chemical potential 2.84 eV. The value of electrical conductivity is high for positive chemical potential μ as compared to negative value of chemical potential μ.

Both electrons and phonons are heat carrier, so the thermal conductivity κ has two contributions, namely, the electronic thermal conductivity κ_e (electron contribution) and lattice thermal conductivity κ_L (phonon contribution). The electronic thermal conductivity κ_e as a function of chemical potential at different temperatures is plotted in Figure (4.10). At chemical potential 2.84 eV the maxima of the electronic thermal conductivity in c-direction increases from 5.8 $\mathrm{Wm}^{-1}\mathrm{K}^{-1}$ at 50 K to 17.3 $\mathrm{Wm}^{-1}\mathrm{K}^{-1}$ at 150 K.

The power factor $S^2\sigma$ reflects the ability of the thermoelectric material to produce useful electrical power, high $S^2\sigma$ is critical for good thermoelectric performance. The

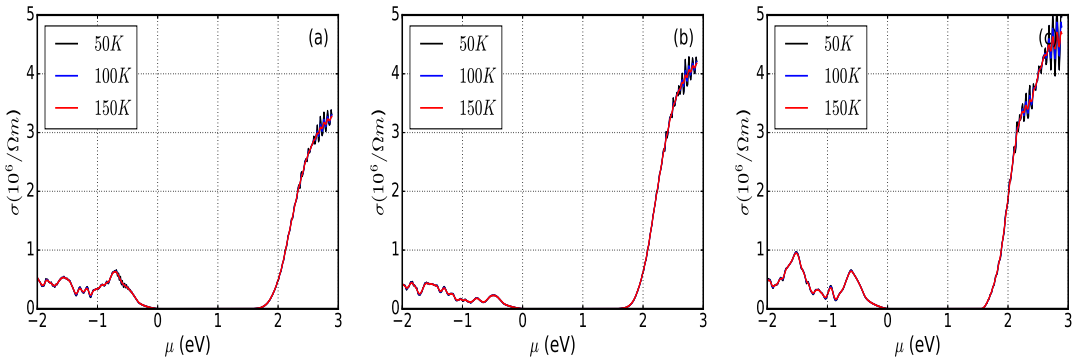


Figure 4.9: (Color online) Variation of electrical conductivity σ with respect to chemical potential μ for the orthorhombic $CH_3NH_3PbI_3$ at different temperatures in the (a) a-direction, (b) b-direction, and (c) c-direction.

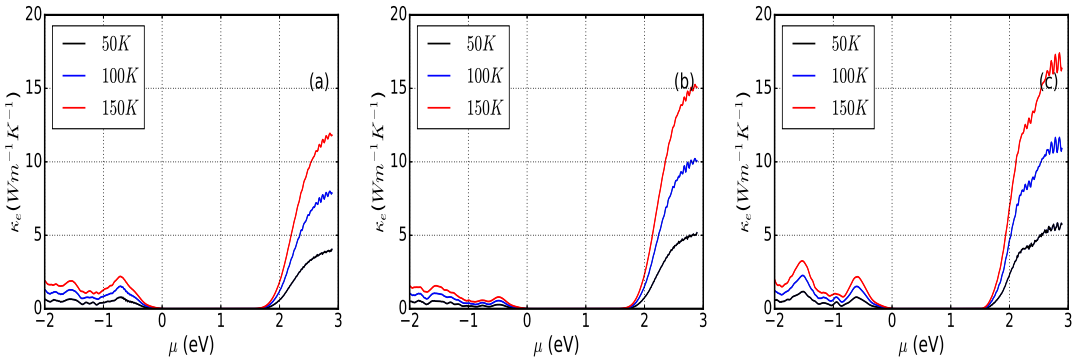


Figure 4.10: (Color online) Variation of electronic thermal conductivity κ_e with respect to chemical potential μ for the orthorhombic $CH_3NH_3PbI_3$ at different temperatures in the (a) a-direction, (b) b-direction, and (c) c-direction.

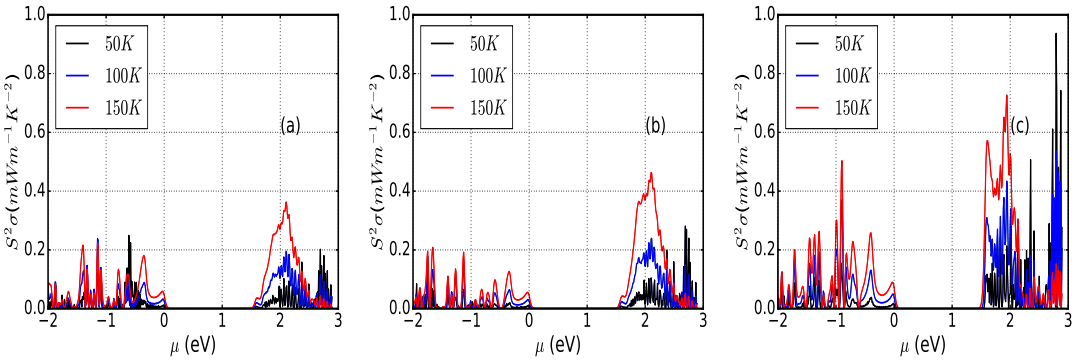


Figure 4.11: (Color online) Calculated power factor $S^2\sigma$ with respect to chemical potential μ for the orthorhombic $CH_3NH_3PbI_3$ at different temperatures in the (a) a-direction, (b) b-direction, and (c) c-direction.

calculated $S^2\sigma$ with respect to chemical potential at different temperatures are depicted in Figure (4.11). At chemical potential 1.96 eV in the c-direction the maximum values of $S^2\sigma$ were found to be 0.00042 $\mathrm{Wm^{-1}K^{-2}}$ and 0.00072 $\mathrm{Wm^{-1}K^{-2}}$ at 100 K and 150 K, respectively. Using the calculated transport coefficients, the figure of merit ZT as a function of chemical potential at low and room temperatures along a-, b- and c-directions is obtained as shown in Figure (4.12). We can see that the values of ZT increase with increasing temperature. The maxima of the ZT in the c-direction increases from 0.06 at 100 K to 0.122 at 150 K. This indicates that the orthorhombic $CH_3NH_3PbI_3$ is a poor candidate for thermoelectric applications.

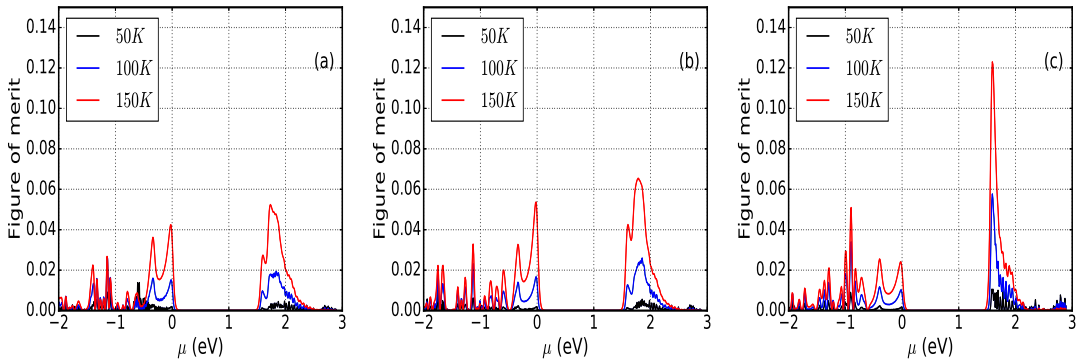


Figure 4.12: (Color online) Calculated figure of merit with respect to chemical potential μ for the orthorhombic $CH_3NH_3PbI_3$ at different temperatures in the (a) a-direction, (b) b-direction, and (c) c-direction.

4.1.7 Optical Properties

The investigation of the optical properties of $CH_3NH_3PbI_3$ perovskite is very important, because it is potentially good candidate for photo and optoelectronic applications. Our GW calculations were performed without including the effect of the spin orbit coupling. Using the real part $\varepsilon_{\mathrm{re}}(\omega)$ and the imaginary part $\varepsilon_{\mathrm{im}}(\omega)$ of the dielectric tensor $\varepsilon(\omega)$, we computed the absorption spectra $\alpha(\omega)$, refractive index $n(\omega)$, and reflectivity $R(\omega)$. From the absorption coefficient $\alpha(\omega)$ spectrum, the highest absorption peaks occur in the optical region (1.65-3.26) eV.

The real $\varepsilon_{\mathrm{re}}(\omega)$ and the imaginary $\varepsilon_{\mathrm{im}}(\omega)$ parts of the complex frequency-dependent dielectric tensor are presented in sub-figure (4.13) (a), where we can see that the dielectric tensors show a significant anisotropy from a-, b-, and c-directions. The calculated

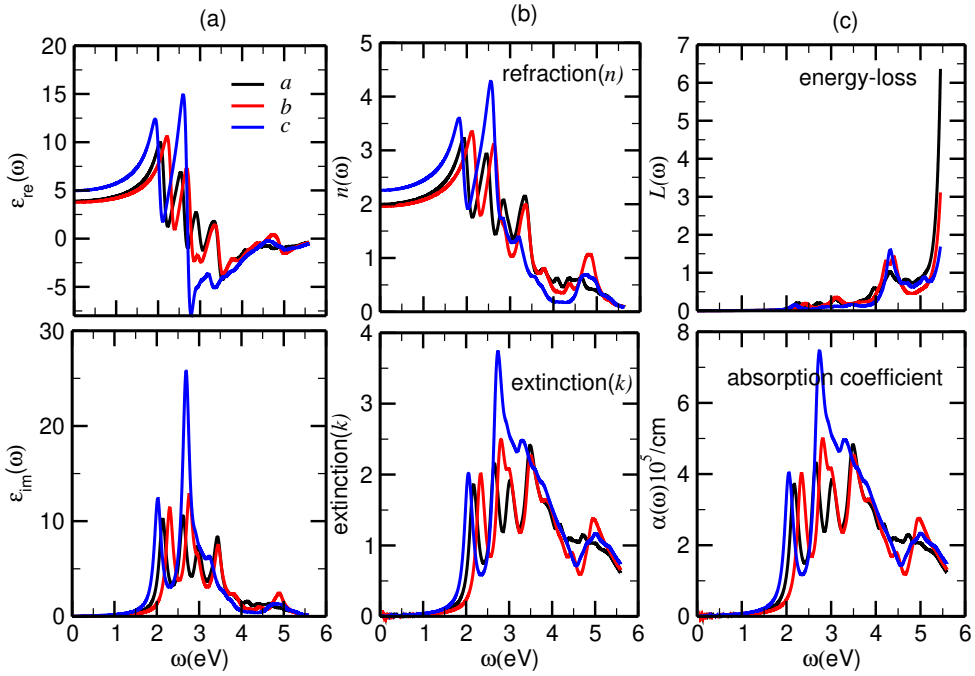


Figure 4.13: (Color online) Optical spectra for the orthorhombic $CH_3NH_3PbI_3$ calculated using PBEsol: (a) real $\varepsilon_{\rm re}(\omega)$ and the imaginary $\varepsilon_{\rm im}(\omega)$ parts of the dielectric function, (b) Refraction $n(\omega)$ and extinction coefficient $k(\omega)$, (c) Energy loss $L(\omega)$ and absorption coefficient $\alpha(\omega)$.

static dielectric constants $\varepsilon_{\rm re}(0)$ are found to be 3.87, 3.73 and 5.01 in the a-, b-, and c-directions, respectively.

The calculated spectrum of refractive index $n(\omega)$ and extinction coefficient $k(\omega)$ are displayed in sub-figure (4.13) (b). The calculated static refractive indices are 1.97, 1.95 and 2.24 in the a-, b-, and c-directions, respectively. The static refractive index $n(0)$ is related to $\varepsilon_{\rm re}(0)$ by the relation $n(0) = \sqrt{\varepsilon_{\rm re}(0)}$. The maximum value of refractive index for the orthorhombic $CH_3NH_3PbI_3$ structure is obtained to be 4.3 in c-direction at optical frequency of 2.56 eV, while the maximum value of the refractive index in the a- and b-directions are observed at 2.08 eV and 2.25 eV optical frequency with magnitude of 3.29 and 3.4 respectively.

Sub-figure (4.13) (c) shows the calculated absorption spectrum $\alpha(\omega)$ and energy loss $L(\omega)$ in the a-, b-, and c-directions. From the absorption coefficient spectrum, the highest absorption peak $\alpha_c(\omega)$ components is higher than that of $\alpha_a(\omega)$ and $\alpha_b(\omega)$. Moreover, the anisotropy of the phase is evident from the clear differences between the three spectra. In Figure (4.14), the absorption coefficient $\alpha(\omega)$ is plotted in Tauc

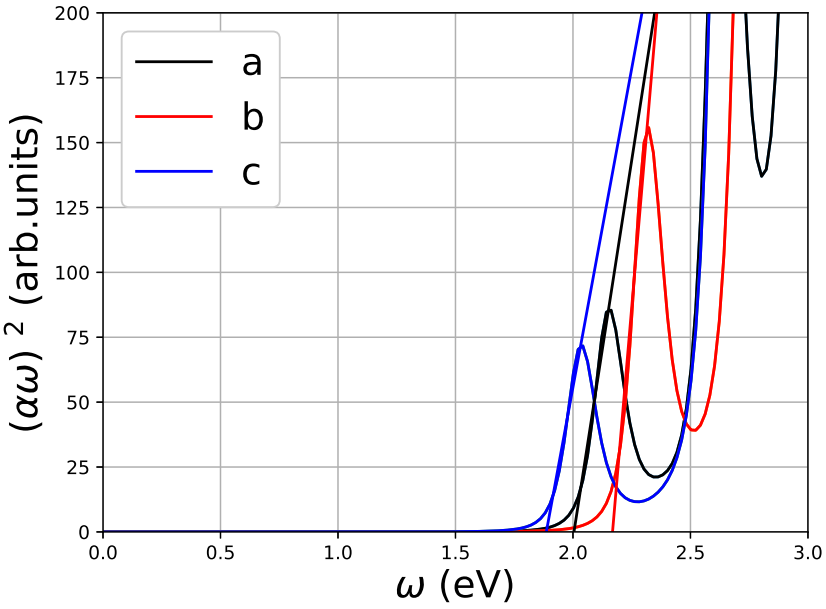


Figure 4.14: (Color online) Tauc plot of the absorption coefficient, showing the polarization-dependent onsets for the orthorhombic $CH_3NH_3PbI_3$.

form with exponent 2. The edge of the absorption is obtained by linear extrapolation of $(\alpha\omega)^2$ to zero absorption. From Figure (4.14), we can see that there are clear absorption edges as function of polarization as a result of the structural anisotropy. In the a-, b- and c-directions, the onsets are found to be 2.00 eV, 2.16 eV and 1.88 eV, respectively. From the obtained band gap, we calculate the solar cell efficiency limits using Shockley-Queisser (SQ) model. The orthorhombic $CH_3NH_3PbI_3$ efficiency was estimated to be 28.8% (see appendix E). This suggest that the orthorhombic $CH_3NH_3PbI_3$ may be potential material for photovoltaic applications.

4.2 Caesium Lead Triiodide Perovskite

The focus of this section is to investigate the structural, mechanical and dynamical stabilities, electronic, lattice thermal conductivity and optical properties of orthorhombic structure $CsPbI_3$ based on the theoretical methods (introduced in Chapter 2) and computational details (described in Chapter 3), our obtained results are presented and discussed.

4.2.1 Structural Properties

At higher temperature (634 K), $CsPbI_3$ possesses a cubic phase (space group $Pm\bar{3}m$) [49]. As temperature decreases, the cubic phase is transformed to a tetragonal phase [50]. At low temperatures (i.e. 293 K [30] and 298 K [49]), CsPbI3 possesses an orthorhombic phase (space group Pnma) known as yellow phase. The orthorhombic $CsPbI_3$ system investigated here has space group Pnma (No. 62) at 293 K [30], with experimental lattice constants are a = 10.4342 $\mathring{A}$, b = 4.7905 $\mathring{A}$ and c = 17.610 $\mathring{A}$ [30]. Structural properties can be determined from calculations of the ground state energy E(eV) as a function of cell volume V($\mathring{A}^3$). We optimized the lattice parameters and ionic positions using PBE and PBEsol approximations to find the most suitable method for this material. The calculated total binding energy against cell volume were least-squares-fitted using the Murnaghan and Birch equations of state (EOS) [126, 127] as shown in Figure (4.15). The corresponding optimized lattice parameters, cohesive energy and equilibrium volume are summarized in Table (4.7). Experimental and reported theoretical results are also presented for comparison. The cohesive energy E_{coh} is defined as the negative of the energy that must be supplied to the solid to separate its constituents into neutral free atoms at rest and at infinite separation [105]. From Table (4.7), the calculated negative cohesive energies indicate that the $CsPbI_3$ compound in the orthorhombic phase is energetically stable.

Table 4.7: Calculated equilibrium parameters of the orthorhombic $CsPbI_3$: Lattice constants (a(Å), b(Å), c(Å)), equilibrium volume V_0(Å^3) and cohesive energy E_{coh}(eV/atom) compared with the other experimental (Exp.) and theoretical study (PBE).

Method/Functional	a(Å)	b(Å)	c(Å)	V_0($\mathring{A}^3$)	E_{coh}(eV/atom)
PBE	10.8668	4.8914	18.2425	969.65	-2.57
PBEsol	10.4175	4.7561	17.6599	874.99	-2.78
Exp. [30]	10.4342	4.7905	17.6100	887.78	-
Exp. [49]	10.4581	4.8017	17.7761	892.66	-
PBE [166]	10.0280	4.8530	18.1640	883.97	-

It is well known that the density functional theory calculations are performed at 0 K temperature. In contrast the experimental results [30] and [49] which were obtained at 293 K and 298 K, respectively. It can be seen clearly that our calculated lattice constants and volume with PBEsol (874.99 $\mathring{A}$) agree with experimental results (887.78 $\mathring{A}$) [30] better than those calculated with PBE (969.65 $\mathring{A}$). This is consistent with the

general rule of thumb that PBEsol provides superior structural parameters (relative to experimental data) when compared to PBE [93]. Therefore, the other structural properties are investigated based on the optimized structure using the PBEsol functional. The calculated lattice constants are comparable with the other theoretical result [166]. The differences in the values presented in Table (4.7) can be attributed to the different exchange-correlation functional and pseudopotentials used.

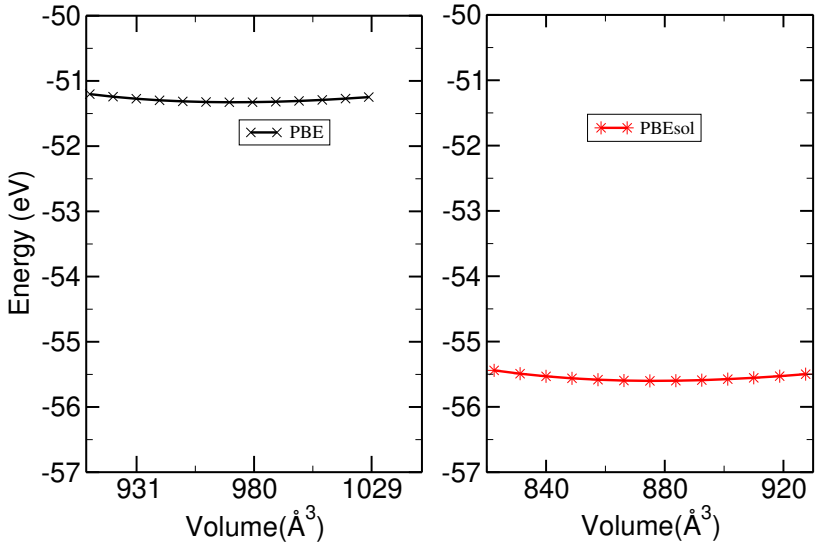


Figure 4.15: Calculated total binding energy versus volume using PBE and PBEsol of the orthorhombic $CsPbI_3$.

4.2.2 Mechanical Stability

In order to determine stability of a given material or structure, it is crucial to examine its elastic constants and phonon band structure. The elastic constants and the phonon dispersion relation were calculated using PBEsol approximations.

The elastic constants obtained are given in Table (4.8), but no experimental values are available fo comparison. The mechanical stability for the orthorhombic $CsPbI_3$ system was obtained by checking that all the elastic constants are positive and satisfy the Born conditions (Eq. 3.3.1). From the obtained results, one can confirm that the structure is mechanically stable against the influence of external forces. Bulk modulus B, shear modulus G and Young's modulus E_H were calculated by the Voigt-Reuss-Hill method (VRH) for an orthorhombic crystal as discussed in Subsection (3.3.1). The calculated bulk moduli (B_R, B_V and B_H), shear moduli (G_R, G_V and G_H), Young's modulus E_H

Table 4.8: Calculated independent elastic constants in (GPa) for the orthorhombic $CsPbI_3$.

Functional	C_{11}	C_{12}	C_{13}	C_{22}	C_{23}	C_{33}	C_{44}	C_{55}	C_{66}
PBEsol	11.31	07.32	09.43	21.81	12.91	27.49	07.02	06.29	10.28

Table 4.9: The calculated bulk moduli (B_R, B_V, B_H in GPa), shear moduli (G_R, G_V, G_H in GPa), Young's modulus (E in GPa) of the orthorhombic $CsPbI_3$.

Functional	B_R	B_V	B_H	G_R	G_V	G_H	E_H
PBEsol	10.45	13.33	11.89	05.85	06.78	06.32	16.10

in GPa are listed in Table (4.9). The bulk modulus B_H (an average of bulk modulus B_V and bulk modulus B_R) will be used as a measure of the average atomic bond strength of materials because it has a strong correlation with binding energy of atoms in crystal [157]. From the criterion for brittleness and ductility of materials based on the ratio B/G related to the critical value 1.75 [158], the ratio $B/G < 1.75$ indicates that the crystal is brittle and if the ratio $B/G > 1.75$ indicates that the crystal is ductile. The present B/G ratio 1.88, suggest that this material has ductile property.

4.2.3 Dynamical Stability

In this work, phonon properties were computed using a finite displacement method as implemented in Phonopy package at the level of harmonic approximation. The force constants (acting due to small displacements of the atoms) of $CsPbI_3$ were calculated from a $2 \times 4 \times 1$ supercell containing 160 atoms. The phonon band structure of $CsPbI_3$ in an orthorhombic system along the high symmetry paths is depicted in Figure (4.16). It can be seen from Figure (4.16) that all phonon modes are positive throughout the Brillouin zone, therefore, the orthorhombic $CsPbI_3$ is dynamically stable under small atomic displacements.

The heat capacity at constant volume C_{v} is calculated from the phonon contribution to the thermal properties as explained in subsection (3.3.2). C_{v} as a function of temperature is shown in Figure (4.17) in the temperature range from 0 K to 300 K. Since the orthorhombic phase $CsPbI_3$ is stable at room temperature, the inset graph shows heat capacity up to 150 K for comparison with the orthorhombic phase $CH_3NH_3PbI_3$.

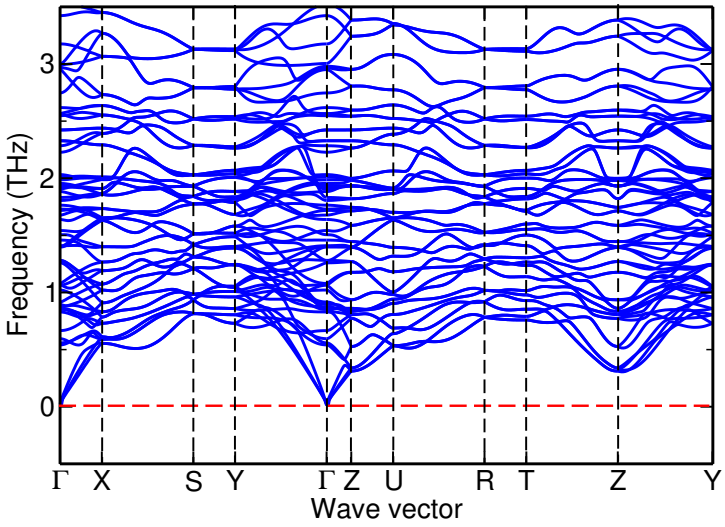


Figure 4.16: (Color online) Phonon dispersion relation graph of the orthorhombic $CsPbI_3$ calculated using PBEsol.

4.2.4 Electronic Properties

The calculated band structure for the orthorhombic phase $CsPbI_3$ along the high symmetry directions of the Brillouin zone is shown in Figure (4.18). The Fermi level is shifted to zero and is shown by the horizontal dashed line. Since the Fermi level is closer to the VBM this indicates $CsPbI_3$ is a *p*-type semiconductor. The calculated band gap is 2.52 eV and 2.38 eV by PBE and PBEsol, respectively. Our calculated band gap using PBE functional is in agreement to that reported bay Murad et al. [50] which is also based on PBE functional. Our calculated, reported theoretical and experimental electronic band-gap of the $CsPbI_3$ orthorhombic phase are listed in Table (4.10). It is well known that GGA approximation underestimates the calculated band gaps. Thus, our calculated values above can serve as the lower estimates of the experimental band gap 2.82 eV reported by Ref. [51]. It can be seen that, $CsPbI_3$ in an orthorhombic system is an indirect band gap material since the conduction band minimum (CBM) is at the X point in the Brillouin zone, whereas the valence band maximum (VBM) is in the segment between Y and Γ points in the Brillouin zone. Previous theoretical work by Murad et al. [50] show that the orthorhombic $CsPbI_3$ is a direct band gap with the corresponding value 1.68 eV based nTmBJ exchange potential, which is underestimated compared to the experimental one 2.82 eV [51]. However, the effect of spin orbit coupling on the PBEsol calculation reduces the band gap by 0.99 eV, down to 1.83 eV, which is lower than the experimental value. Moreover, other calculations [52] predicted

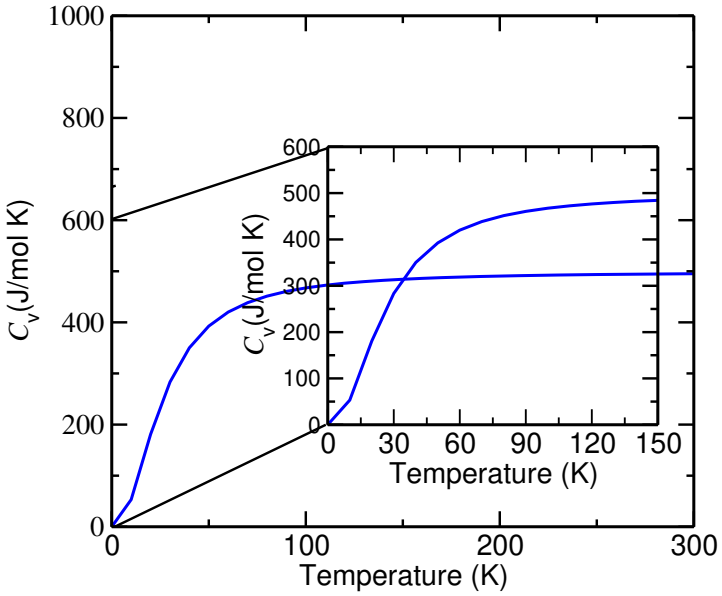


Figure 4.17: The heat capacity at constant volume as a function of temperature for the orthorhombic $CsPbI_3$. The inset shows specific heat C_v when temperature goes from 0 K up to 150 K.

an energy band gap of 2.64 eV.

Table 4.10: Our calculated, reported experimental electronic band gap of the orthorhombic $CsPbI_3$.

Method	PBE	PBEsol	SOC	GW	BSE			Exp.[51]	HSE+SOC [52]
					a	*b*	*c*		
Band gap (eV)	2.52	2.38	1.83	3.67	2.59	2.39	2.49	2.82	2.64

The total density of states (TDOS) and its corresponding partial density of states (PDOS) of $CsPbI_3$ have been calculated and analyzed to further understand the bonding mechanisms between atoms. Figure (4.18) shows the total density of states (TDOS) and the partial density of states (PDOS) for the investigated structure using the PBEsol functional. Similar to $CH_3NH_3PbI_3$ (see Figure (4.4)), it can be seen that around the fundamental band gap, only iodine I and lead Pb contribute to the DOS. Also the cation Cs^+ makes little contribution to the top valence band maximum (VBM) and bottom conduction band minimum (CBM). Therefore, the contribution of cation Cs^+ to the Fermi level region is very weak.

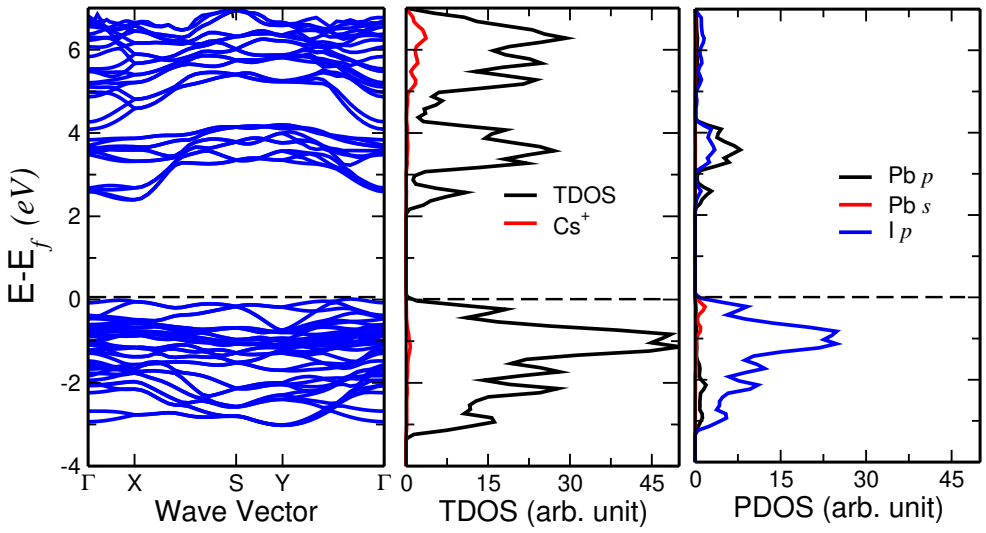


Figure 4.18: (Color online) DFT calculated electronic structure of the orthorhombic $CsPbI_3$: band structure (left), total density of states (TDOS) and Cs^+ cation projected density of states PDOS (middle), and Pb and I atomic orbital PDOS.

4.2.5 Lattice Thermal Conductivity

The lattice thermal conductivity κ_L can be calculated through the Boltzmann transport equation for phonons as described in Section (2.7). Using the phono3py code [151], the calculated lattice thermal conductivity κ_L for $CsPbI_3$ in an orthorhombic phase is shown as functions of temperature in Figure (4.19), where temperature goes from 0 K to 300 K. The calculated lattice thermal conductivities at 300 K were found to be 0.153, 0.354 and 0.106 $Wm^{-1}K^{-1}$ in the a-, b- and c-directions, respectively. Because, a good thermoelectric material must have low thermal conductivity κ, ZT is inversely depend on κ. This low lattice thermal conductivity of the orthorhombic $CsPbI_3$ is desirable for thermoelectric applications. The average lattice thermal conductivity at 150 K and 300 K are 0.406 and 0.204 $Wm^{-1}K^{-1}$, respectively. Our calculated average value at 300 K is in the same range as the calculated value in Ref. [32] for the cubic $CsPbI_3$.

Figure (4.19), shows the trend $\kappa_L(b) > \kappa_L(a) > \kappa_L(c)$ in the entire temperature range. At 300K, the ratios $\kappa_L(b)/\kappa_L(a) = 2.31$ and $\kappa_L(b)/\kappa_L(c) = 3.31$, indicate high anisotropic behaviour of the structure.

In order to understand the lattice thermal conductivity of $CsPbI_3$, we explore the phonon-related properties such as phonon group velocities and phonon lifetimes. The phonon group velocities and phonon lifetimes are shown in Figure (4.20). As we can

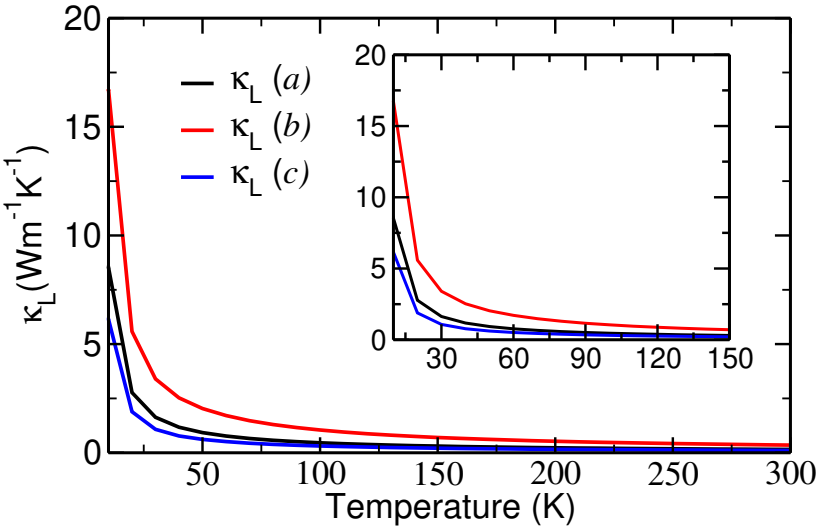


Figure 4.19: (Color online) The calculated lattice thermal conductivity ($Wm^{-1}K^{-1}$) in the a-, b- and c-directions for the orthorhombic $CsPbI_3$.

see, the most of group velocities of acoustic modes of $CsPbI_3$ are larger than those of $CH_3NH_3PbI_3$. Due to dominated contribution to total lattice thermal conductivity from acoustic modes, group velocities can partially explain higher lattice thermal conductivity for $CsPbI_3$ than $CH_3NH_3PbI_3$. Moreover, it is clearly seen from Figure (4.20) and Figure (4.7) that phonon lifetimes of $CsPbI_3$ are higher than that of $CH_3NH_3PbI_3$.

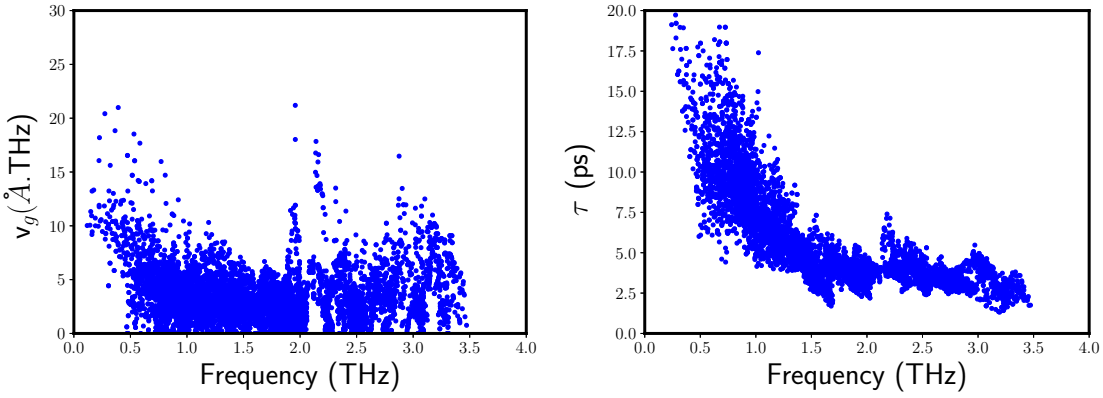


Figure 4.20: (Color online) The phonon group velocities (Left) and the phonon lifetimes (Right) for the orthorhombic $CsPbI_3$ at 150 K in the first Brillouin zone.

4.2.6 Optical Properties

The investigation of the optical properties of $CsPbI_3$ perovskite is very important because it is potentially good candidate for photo- and optoelectronic applications. The optical properties are in general evaluated with the help of the frequency-dependent complex dielectric function $\varepsilon(\omega) = \varepsilon_{\rm re}(\omega) + i\varepsilon_{\rm im}(\omega)$. In order to obtain optical spectra, we carried out Bethe-Salpeter Equation (BSE) calculations on top of non-self-consistent G_0W_0 calculations. Our GW calculations were performed without including the effect of the spin orbit coupling. For $CsPbI_3$ we use 2016 bands with an energy cut-off of 300 eV and an energy cut-off of 120 eV for the plane wave basis of the response function and 48 frequency grid points for the energy integration. Using the real part $\varepsilon_{\rm re}(\omega)$ and the imaginary part $\varepsilon_{\rm im}(\omega)$ of the dielectric tensor $\varepsilon(\omega)$, we computed the absorption spectra $\alpha(\omega)$, energy loss $L(\omega)$, refractive index $n(\omega)$, and extinction coefficient $k(\omega)$. To the best of our knowledge, this is first attempt to study the optical properties of $CsPbI_3$ at the BSE level of approximation.

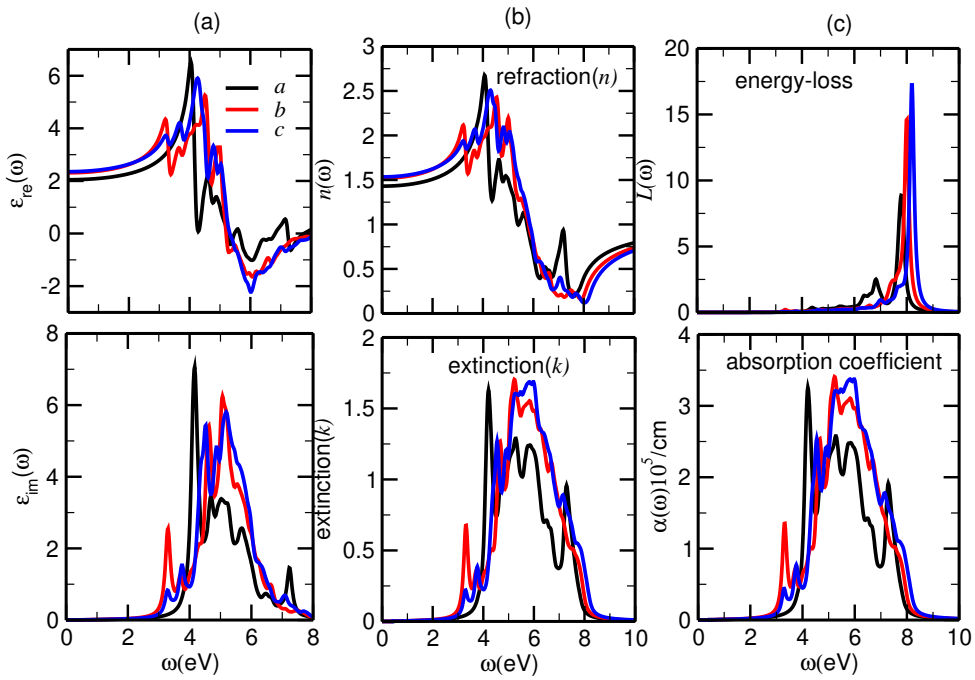


Figure 4.21: (Color online) Optical spectra of the orthorhombic $CsPbI_3$ calculated using PBEsol: (a) real $\varepsilon_{\rm re}(\omega)$ and the imaginary $\varepsilon_{\rm im}(\omega)$ parts of the dielectric function, (b) Refraction $n(\omega)$ and extinction coefficient $k(\omega)$, (c) Energy loss $L(\omega)$ and absorption coefficient $\alpha(\omega)$.

The real $\varepsilon_{\rm re}(\omega)$ and the imaginary $\varepsilon_{\rm im}(\omega)$ parts of the complex frequency-dependent

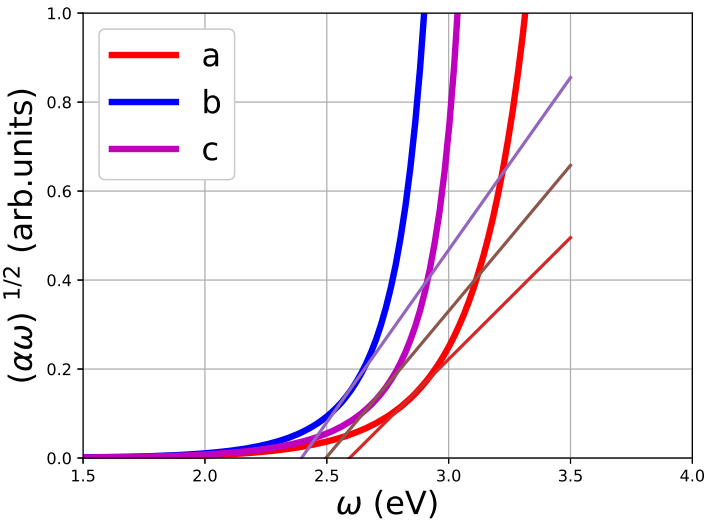


Figure 4.22: (Color online) Tauc plot of the absorption coefficient, showing the polarization-dependent onsets of the orthorhombic $CsPbI_3$.

dielectric tensor are presented in (sub-figure (4.21) (a) top) from 0 to 8 eV, where we can see that the dielectric tensors show a significant anisotropy from a-, b-, and c-directions. The calculated static dielectric constants $\varepsilon_{\text{re}}(0)$ are found to be 2.04, 2.34 and 2.40 in a-, b-, and c-directions, respectively. The main peaks in the real part $\varepsilon_{\text{re}}(\omega)$ are located in the visible region of the spectrum and ultraviolet (UV) region. As we can see in (sub-figure (4.21) a top) the negative value of the real part $\varepsilon_{\text{re}}(\omega)$ (in the UV region), indicate that incident photons are totally reflected. The imaginary part $\varepsilon_{\text{im}}(\omega)$ in (sub-figure (4.21) a bottom) shows an upward trend before $\sim$ 3 eV and its main peaks are located in the optical region and UV region.

The calculated spectrum of refractive index $n(\omega)$ and extinction coefficient $k(\omega)$ are displayed in sub-figure (4.21) (b). The calculated static refractive indices are 1.43, 1.53 and 1.55 in the a-, b-, and c-directions, respectively. The static refractive index $n(0)$ is related to $\varepsilon_{\text{re}}(0)$ by the relation $n(0) = \sqrt{\varepsilon_{\text{re}}(0)}$. The maximum value of refractive index for $CsPbI_3$ structure is obtained to be 2.66 in a-direction at optical frequency of 4.10 eV, while the maximum value of the refractive index for b- and c-directions are observed at 4.54 eV and 4.32 eV optical frequency located in the UV region, with magnitude of 2.42 and 2.49 respectively.

Sub-figure (4.21) (c) shows the calculated absorption spectrum $\alpha(\omega)$ and energy loss $L(\omega)$ in the a, b, and c directions. The highest absorption peaks for $CsPbI_3$ occur in

the optical region and ultraviolet region. From the absorption coefficient spectrum, the highest absorption peak $\alpha_c(\omega)$ components is higher than that of $\alpha_a(\omega)$ and $\alpha_b(\omega)$. Moreover, the anisotropy of the phase is evident from the clear differences between the three spectra. In Figure (4.22), the absorption coefficient $\alpha(\omega)$ is plotted in Tauc form with exponent 2. The edge of the absorption is obtained by linear extrapolation of $(\alpha\omega)^2$ to zero absorption. From Figure (4.22), we can see that there are clear absorption edges as function of polarization as a result of the structural anisotropy. In the a-, b- and c-directions, the onsets are found to be 2.59 eV, 2.39 eV and 2.49 eV, respectively. From the obtained band gap, we calculate the solar cell efficiency limits using Shockley-Queisser (SQ) model. The orthorhombic $CsPbI_3$ efficiency was estimated to be 16.25% (see appendix E). Therefore, $CsPbI_3$ may be potential material for optoelectronic devices applications.

4.3 Methylammonium Tin Triiodide Perovskite

$CH_3NH_3PbX_3$ (X = Cl, Br or I) is considered as a promising material for solar cell application with an expected photo conversion efficiency 20.1% [38, 53]. However, this progress in efficiency, is hindered by many challenges such as the instability of many its phases [54] and the toxicity of lead [55]. Therefore, it is necessary to find an alternative stable material that does not contain toxic lead. A possible candidate is methylammonium tin iodide perovskite, $CH_3NH_3SnI_3$. The focus of this section is to investigate the structural, mechanical and dynamical stabilities, electronic and optical properties of orthorhombic structure $CH_3NH_3SnI_3$ under pressure based on the theoretical methods (introduced in Chapter 2) and computational details (described in Chapter 3), our obtained results are presented and discussed. The results on this section have been submitted to the journal for publication. The crystal structure of the orthorhombic phase (space group Pnma 62) of the halide perovskite is shown in Figure (4.23).

4.3.1 Structural Properties

The unit cell of $CH_3NH_3SnI_3$ contains of 48 atoms (24 H atoms, 4 Pb atoms, 4 C atoms, 12 I atoms, and 4 N atoms). We have performed structural optimization of the orthorhombic phase of $CH_3NH_3SnI_3$ under pressure, with all the structural parameters relaxed. Our calculated lattice parameters, cohesive energy (E_{coh}) and initial volume

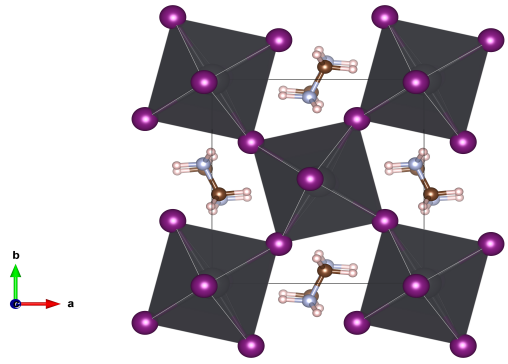


Figure 4.23: (Color online) The crystal structure of the $CH_3NH_3SnI_3$ orthorhombic phase with space group Pnma (No. 62).

(V^{ref}) obtained from our calculations compared with other theoretical and experimental results are summarized in Table (4.11). The cohesive energy E_{coh} is defined as the negative of the energy that must be supplied to the solid to separate it into its neutral free atoms at rest and at infinite separation [105]. From Table (4.11), the calculated negative cohesive energies indicate that the $CH_3NH_3SnI_3$ compound in the orthorhombic phase is energetically stable.

Table 4.11: Calculated parameters of the orthorhombic $CH_3NH_3SnI_3$: Lattice constants (a(Å), b(Å), c(Å)), initial volume V_0(Å^3) and cohesive energy E_{coh} (eV/atom) at 0.7 GPa compared with the other experimental and theoretical study at zero-pressure.

Functional/Method	a(Å)	b(Å)	c(Å)	V_0(Å^3)	E_{coh}(eV/atom)
PBE (0.7 GPa)	9.059	12.496	8.394	950.32	-3.13
Experiment [58]	8.745	12.353	8.526	921.04	-
PBE (0.0 GPa) [42]	8.556	12.428	8.351	888.1	-

4.3.2 Mechanical Stability

The mechanical stability for $CH_3NH_3SnI_3$ system was obtained by checking that all the elastic constants are positive and satisfy the Born conditions for mechanical stability [131]. The computed elastic constants are shown in Table (4.12) together with the available calculated results for $CH_3NH_3SnI_3$ at zero-pressure [42]. The calculated elastic constants are comparable with the other theoretical values [42]. The differences in the values presented in Table (4.12) can be attributed to the different in pressure (applied stress). The mechanical stability for $CH_3NH_3SnI_3$ system was obtained by checking

that all the elastic constants are positive and satisfy the Born conditions (Eq. 3.3.10) for mechanical stability.

Table 4.12: Calculated independent elastic constants for the orthorhombic $CH_3NH_3SnI_3$ in GPa (Cal.) at 0.7 GPa compared with the other theoretical study (PBE+D2) at zero-pressure.

Functional	$\tilde{C}_{11}$	$\tilde{C}_{12}$	$\tilde{C}_{13}$	$\tilde{C}_{22}$	$\tilde{C}_{23}$	$\tilde{C}_{33}$	$\tilde{C}_{44}$	$\tilde{C}_{55}$	$\tilde{C}_{66}$
Cal.	30.48	14.69	11.08	26.08	10.51	39.67	06.04	04.85	13.70
PBE+D2 [42]	46.10	12.10	26.70	21.20	06.80	16.70	13.30	0.50	08.30

The calculated elastic moduli for the $CH_3NH_3SnI_3$ orthorhombic crystal using the Voigt-Reuss-Hill approximations with other reported theoretical values are listed in Table (4.13). Since, the orthorhombic $CH_3NH_3SnI_3$ is not dynamically stable at zero-pressure, the bulk moduli were only reported at 0.7 GPa. The differences in the values presented in Table (4.13) are due to the different in pressure (applied stress). The shear anisotropic factors obtained from equations (3.3.5) and (3.3.12) along with the other theoretical ones are given in Table (4.14). From the criterion for brittleness and ductility of materials based on the ratio B/G related to the critical value 1.75 [158], the ratio $B/G < 1.75$ indicates that the crystal is brittle and if the ratio $B/G > 1.75$ indicates that the crystal is ductile. The present B/G ratio 2.27 at 0.7 GPa, suggest that this material has ductile property. For an isotropic crystal, the factors A_1, A_2 and A_3 should be equal to unity, while any value smaller (as A_1 and A_2) or greater (as A_3) than unity indicates the degree of elastic anisotropy possessed by the crystal.

Table 4.13: The calculated bulk moduli B in GPa, shear moduli G in GPa and Young's modulus E_H in GPa (Cal.) for the orthorhombic $CH_3NH_3SnI_3$ at 0.7 GPa compared with the other theoretical study (PBE+D2) at zero-pressure.

Functional	B_R	B_V	B_H	G_R	G_V	G_H	E_H
Cal.	18.49	18.76	18.62	07.47	08.92	08.19	21.43
PBE+D2 [42]	-	-	18.50	-	-	04.10	16.70

4.3.3 Dynamical Stability

We have calculated the phonon dispersion curves at two different pressures along the high symmetry directions in the Brillouin zone. The calculated phonon band structure of $CH_3NH_3SnI_3$ in an orthorhombic system at 0 and 0.7 GPa are presented in Figure

Table 4.14: The calculated B/G ratio, Poisson's ratio (ν), the shear anisotropic factors (A_1, A_2, A_3) (Cal.) for the orthorhombic $CH_3NH_3SnI_3$ at 0.7 GPa, with the corresponding theoretical study (PBE+D2) at zero-pressure.

Functional	B/G	ν	A_1	A_2	A_3
Cal.	2.27	0.31	0.53	0.43	2.02
Theory [42]	2.99	0.35	5.66	0.07	0.77

(4.24), respectively. The phonon frequencies are in the range of (0-5) THz (the full phonon dispersion span to 100 THz). It can be seen from sub-figure (4.24) (a) that the orthorhombic phase has phonon modes with imaginary frequencies around the Γ point at zero-pressure, which indicates a structural instability. sub-figure (4.24) (b) shows that as a pressure increased to 0.7 GPa, all phonon modes are become positive throughout the Brillouin zone, therefore, the relaxed system is dynamically stable at 0.7 GPa, which agrees with the experimental work [62].

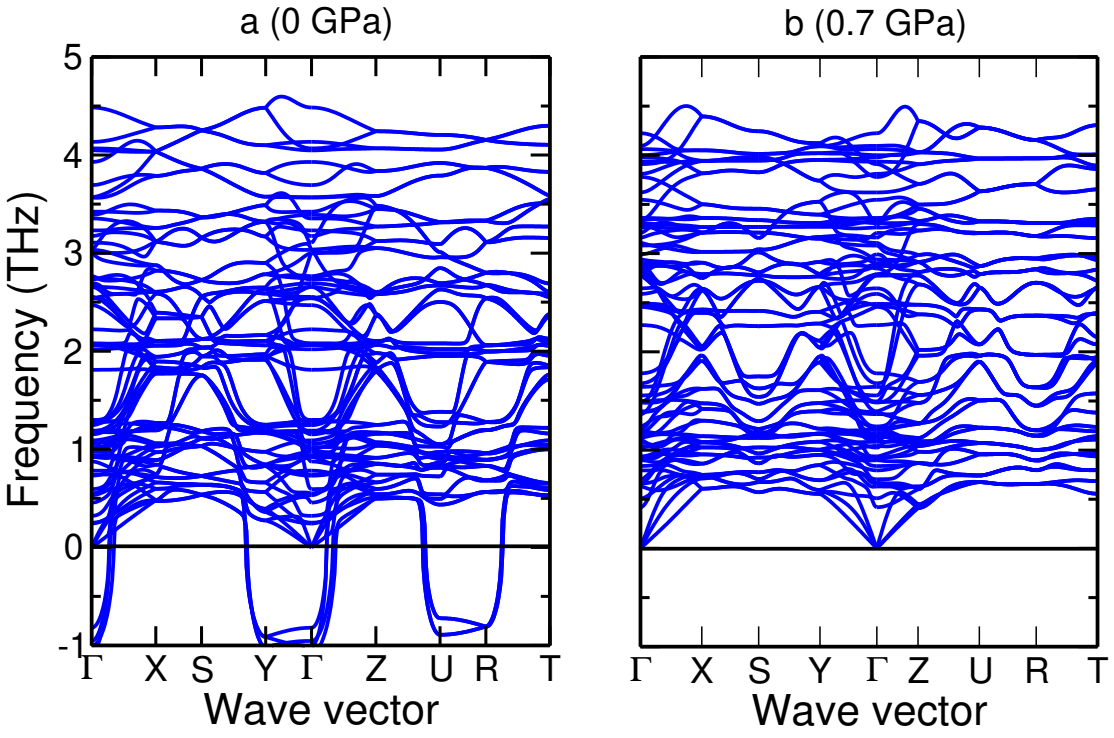


Figure 4.24: Phonon dispersion curves at (a) 0 GPa and (b) 0.7 GPa for the orthorhombic $CH_3NH_3SnI_3$.

4.3.4 Electronic Properties

The calculated band structure for the orthorhombic phase is shown in Figure (4.25). The so-called Fermi level is shifted to zero and is shown by the horizontal dashed line. Since the Fermi level is closer to the VBM this indicates $CH_3NH_3SnI_3$ is a p-type semiconductor. As can be seen in Figure (4.25), the valence band maximum (VBM) and the conduction band minimum (CBM) were found to be located at the gamma point of the Brillouin zone, hence the investigated material has a direct band gap semiconductor character at the gamma point.

The MBJ and HSE06 calculations are done at the PBE lattice parameters at 0.7 GPa. Our calculated and the experimental band gap of the orthorhombic phase are listed in Table (4.3). The PBE functional predicted a band gap of 0.73 eV at 0.7 GPa. This value is small when compared with the experimental result (1.21 eV and 1.35 eV) [30]. It is well known that the GGA-PBE functional tends to underestimate band gaps due to the discontinuity of the functional derivative of the exchange correlation in the Kohn-Sham density functional formalism [167]. To overcome this problem the band gap was estimated by using the hybrid functional HSE06 and meta-GGA MBJ functional, known for their ability to improve the accuracy of the semilocal functional PBE. The predicted band gaps using MBJ and HSE06 at 0.7 GPa are 1.12 eV and 1.21 eV, respectively.

Table 4.15: Calculated electronic band gap of the orthorhombic $CH_3NH_3SnI_3$ perovskite at 0.7 GPa compared to experimentally reported ones at zero-pressure (Exp.) and to previous theoretical study using HSE06 at zero-pressure (Theory).

Functional/Method	PBE	MBJ	HSE06	GW	BSE			Exp.[30]	Theory [56]
					a	b	c		
Band gap (eV)	0.73	1.12	1.21	1.51	1.11	1.21	1.05	1.21-1.35	1.7

Figure (4.25) shows the total density of states (TDOS) and the projected density of states (PDOS) for the investigated structure using the PBE functional at 0.7 GPa. It can be seen that around the fundamental band gap, only I and Sn contribute to the DOS. Also the organic cation $CH_3NH_3^+$ makes little contribution to the VBM and CBM, therefore, the contribution of organic cation $CH_3NH_3^+$ to the Fermi level region is very weak. This finding is consistent with the previous theoretical studies on lead based perovskite [1, 2, 159, 160] at zero-pressure.

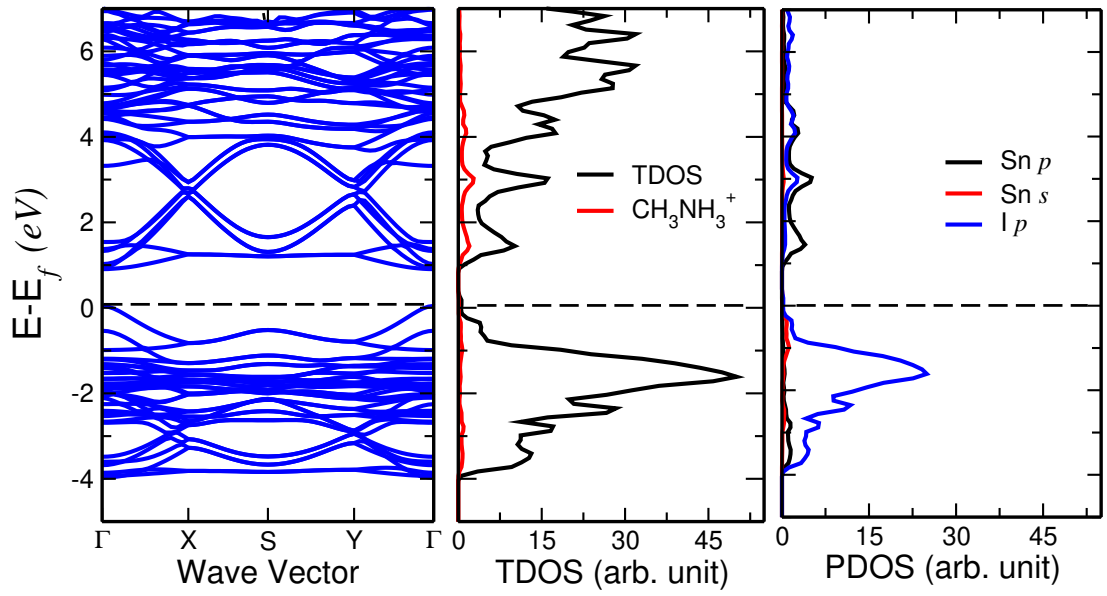


Figure 4.25: (Color online)DFT calculated electronic structure of the orthorhombic $CH_3NH_3SnI_3$ at 0.7 GPa: band structure (left), total density of states (TDOS) and $CH_3NH_3^+$ cation projected density of states PDOS (middle), and Sn and I atomic orbital PDOS.

4.3.5 Optical Properties

The real $\varepsilon_{\rm re}(\omega)$ and the imaginary $\varepsilon_{\rm im}(\omega)$ parts of the complex frequency-dependent dielectric tensor are presented in Figure (4.26), where we can see that the dielectric tensors show a significant anisotropy from a-, b-, and c-directions. The calculated static dielectric constants $\varepsilon_{\rm re}(0)$ are found to be 7.36, 7.18 and 10.95 in a-, b-, and c-directions, respectively.

The calculated spectra of refractive index and reflectivity are displayed in Figure (4.27). The calculated static refractive indices are 2.71, 2.69 and 3.31 in the a-, b-, and c-directions, respectively. The static refractive index $n(0)$ is related to $\varepsilon_{\rm re}(0)$ by the relation $n(0) = \sqrt{\varepsilon_{\rm re}(0)}$. The refractive index is found to have the value 5.54 in c-direction at 1.24 eV and decreases with increasing energy, while the maximum value of the refractive index for a- and b-directions are observed at 1.31 eV and 1.41 eV, respectively.

Figure (4.28) shows the calculated absorption spectrum $\alpha(\omega)$ and energy loss $L(\omega)$ in the a-, b-, and c-directions. From the absorption coefficient spectrum, the highest absorption peak α_c components is higher than that of α_a and α_b. Moreover, the anisotropy of the

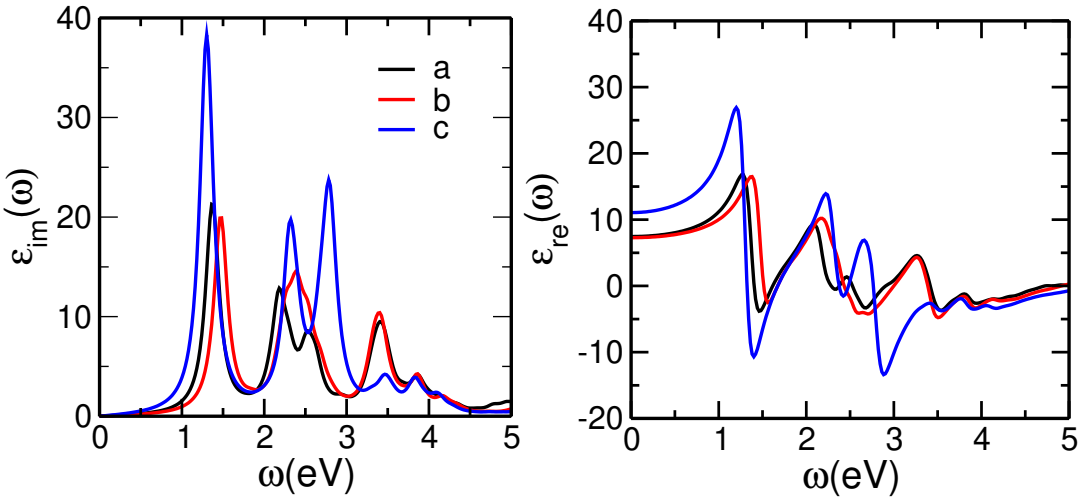


Figure 4.26: (Color online) The calculated real parts $\varepsilon_{\rm re}(\omega)$ and imaginary parts $\varepsilon_{\rm im}(\omega)$ of the dielectric tensor for polarization vectors a, b, and c for the orthorhombic $CH_3NH_3SnI_3$.

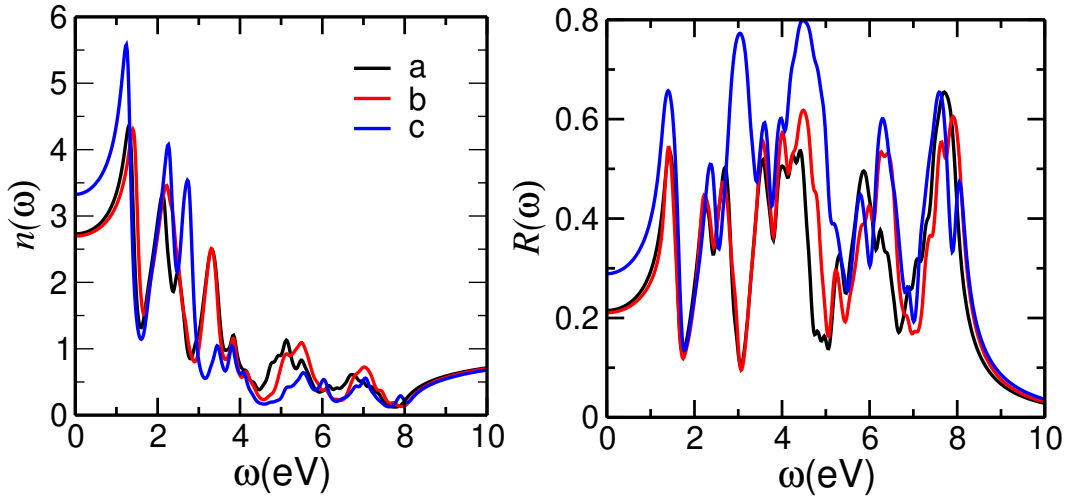


Figure 4.27: (Color online) The calculated refractive index $n(\omega)$ and reflectivity $R(\omega)$ for polarization vectors a, b, and c for the orthorhombic $CH_3NH_3SnI_3$.

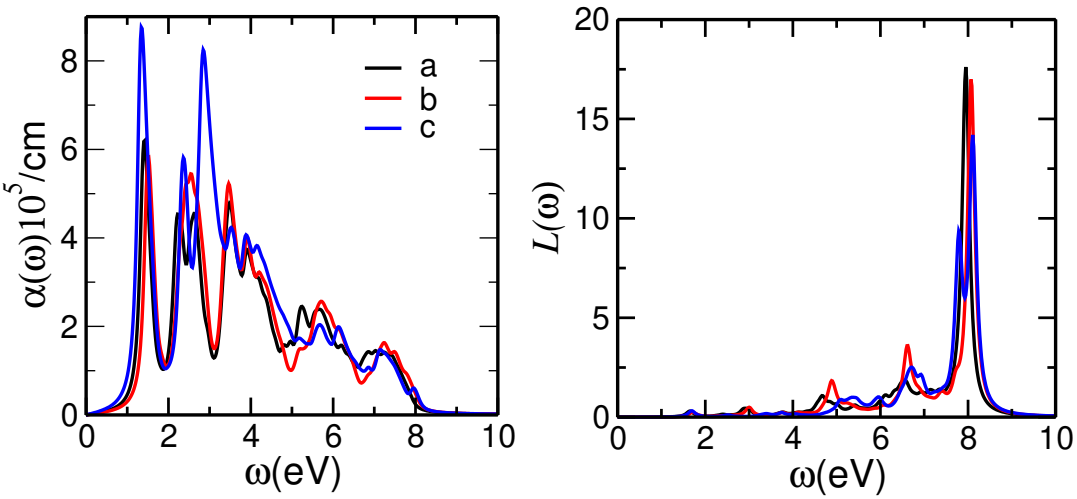


Figure 4.28: (Color online) The calculated absorption coefficient $\alpha(\omega)$, energy loss $L(\omega)$ and the Tauc plot of the absorption coefficient for polarization vectors a, b, and c for the orthorhombic $CH_3NH_3SnI_3$.

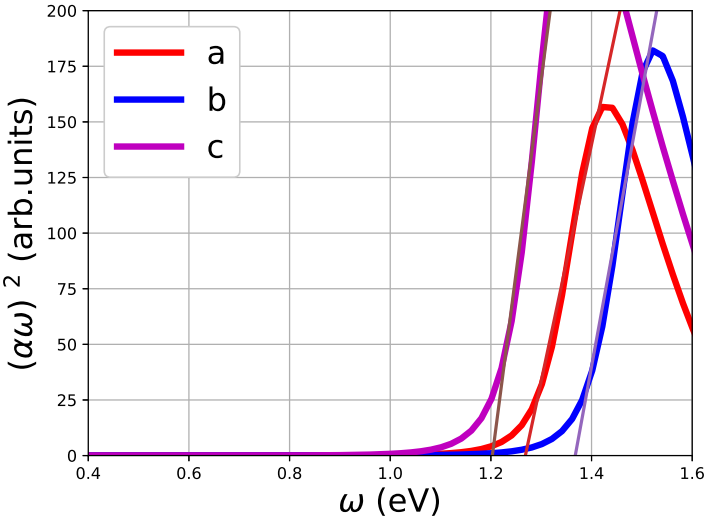


Figure 4.29: (Color online) Tauc plot of the absorption coefficient for the orthorhombic $CH_3NH_3SnI_3$, showing the polarization-dependent onsets.

phase is evident from the clear differences between the three spectra.

In Figure (4.29), the absorption coefficient $\alpha(\omega)$ is plotted in Tauc form with exponent 2. The edge of the absorption is obtained by linear extrapolation of $(\alpha\omega)^2$ to zero absorption. From Figure (4.29), we can see that there are clear absorption edges as function of polarization as a result of the structural anisotropy. In the *a*-, *b*- and *c*-directions, the onsets are found to be 1.27 eV, 1.36 eV and 1.20 eV, respectively. This anisotropy seen in the BSE absorption edges are in good agreement with the experimental results 1.21 eV and 1.35 eV. From the obtained band gap, we calculate the solar cell efficiency limits using Shockley-Queisser (SQ) model. The orthorhombic $CH_3NH_3SnI_3$ efficiency was estimated to be 41.96% (see appendix E). Therefore, $CH_3NH_3SnI_3$ may be potential material for solar cell, especially its potential in low band gap solar cell application.

5

Conclusions and Future Work

5.1 Conclusions

In this thesis we performed first-principles calculations on the structural, mechanical, dynamical stabilities, lattice thermal conductivity, electronic, transport and optical properties of the orthorhombic perovskites of hybrid methylammonium lead triiodide ($CH_3NH_3PbI_3$), hybrid methylammonium tin triiodide ($CH_3NH_3SnI_3$), and all-inorganic caesium lead triiodide ($CsPbI_3$) using density functional theory and many-body perturbation theory calculations in order to provide useful information for their applications as solar cell materials. All electronic structure calculations were performed using the Vienna Ab-inintio Simulation Package (VASP) code. Our results are consistent in most cases with the available experimental data. We hope that the present investigation would be helpful in providing a better theoretical knowledge of the properties of these materials.

5.1.1 $APbI_3$ (A = CH_3NH_3 or Cs)

We investigated the structural, mechanical and dynamical stabilities, electronic, lattice thermal conductivities and optical properties of the orthorhombic halide perovskite $APbI_3$ (A = CH_3NH_3 or Cs) and estimated their solar cells efficiency using the Shockley-Queisser model. The structures were relaxed using PBE and PBEsol. For the structural study, we found that the PBEsol functional predicted structural lattice parameters and

volume are in a better agreement with experimental values in comparison with PBE functional. This is consistent with the general rule of thumb that PBEsol provides superior structural parameters (relative to experimental data) when compared to PBE [93]. The calculated negative cohesive energies predicted that $CH_3NH_3PbI_3$ is the most energetically stable structure than $CsPbI_3$ structure.

The structural stability, elastic constants and vibrational properties and lattice thermal conductivity of the orthorhombic $APbI_3$ (A = CH_3NH_3 or Cs) have been calculated using PBEsol functionals. Since there is no negative phonon frequencies along the high symmetry k-paths in the Brillouin zone. Therefore, the relaxed system is dynamically stable. The equilibrium elastic constants satisfy all the mechanical stability criteria for an orthorhombic crystal, showing stability against the influence of external force.

Electronic properties were investigated by calculating the band structure, partial density of states (PDOS), and the total density of states (TDOS) using the PBEsol functional. For the structural study, around the fundamental band gap, only iodine I and lead Pb contribute to the density of states. Electronic structure calculations show that $CH_3NH_3PbI_3$ ($CsPbI_3$) has a direct (indirect) band gap of about 1.57 eV (2.38 eV). However, the effect of spin orbit coupling on the PBEsol calculation reduces the band gap by 1.11 eV, down to 0.46 eV, for $CH_3NH_3PbI_3$ and by 0.99 eV, down to 1.83 eV for $CsPbI_3$.

The lattice thermal conductivity κ_L is a very important quantity, which significantly affects thermoelectric (TE) material performance. The orthorhombic phase $CH_3NH_3PbI_3$ is only stable at low temperature (T $<$ 165 K). The calculated average lattice thermal conductivities at 150 K for $CH_3NH_3PbI_3$ and $CsPbI_3$ were found to be 0.28 $Wm^{-1}K^{-1}$ 0.407 $Wm^{-1}K^{-1}$, respectively. Our results confirmed the very low thermal conductivity at low temperature. This can be attributed to low group velocities and more importantly to the extremely short phonon lifetimes.

The thermal conductivities of $CH_3NH_3PbI_3$ and $CsPbI_3$ were found to be very low from 0 K to 150 K, with $CsPbI_3$ larger than $CH_3NH_3PbI_3$. To gain insight into the difference between the lattice thermal conductivities of $CH_3NH_3PbI_3$ and that of $CsPbI_3$, we computed the group velocities as well as phonon lifetimes for each compound. Our results show that the most of group velocities of acoustic modes of $CsPbI_3$ are larger than those of $CH_3NH_3PbI_3$. Due to dominate contribution to total lattice thermal conductivity from acoustic modes, group velocities can partially explain higher lattice

thermal conductivity for $CsPbI_3$ than $CH_3NH_3PbI_3$. Moreover, the phonon lifetimes of $CsPbI_3$ are higher than those of $CH_3NH_3PbI_3$; another evidence explain higher lattice thermal conductivity for $CsPbI_3$.

Also, we have carried out a detailed theoretical study of the thermoelectric properties of the most energetically stable structure $CH_3NH_3PbI_3$ based on density functional theory combined with the Boltzmann transport theory within the constant relaxation time approximation as implemented in BoltzWann code. We show that the optimum figure of merit ZT values of the orthorhombic $CH_3NH_3PbI_3$ were found to be 0.06 at 100 K and 0.122 at 150 K in the c-direction. This indicates that the orthorhombic $CH_3NH_3PbI_3$ is a poor candidate for thermoelectric applications.

With the help of the real part $\varepsilon_{\mathrm{re}}(\omega)$ and the imaginary part $\varepsilon_{\mathrm{im}}(\omega)$ of the dielectric tensor $\varepsilon(\omega)$ we derived all the desired frequency-dependent optical spectra at BSE level of approximation. For $CH_3NH_3PbI_3$, the BSE absorption edges, using the Tauc, form were found to be 2.00 eV, 2.16 eV and 1.88 eV in the a-, b- and c-directions, respectively. For $CsPbI_3$, the BSE absorption edges using the Tauc form are found to be 2.59 eV, 2.39 eV and 2.49 eV in the a-, b- and c-directions, respectively. It is well known that the DFT and GW gaps are approximate fundamental gaps, while the BSE gap is approximate optical gaps. More important the highest absorption peaks occur in the optical region (1.65 - 3.26) eV. This suggest that $APbI_3$ (A = CH_3NH_3 or Cs) in the orthorhombic structure may be potential material for solar photovoltaic applications. From the obtained band gap, we calculate the solar cell efficiency limits using Shockley-Queisser model. We found $CH_3NH_3PbI_3$ as the most efficient structure with an efficiency of 28.8%. $CsPbI_3$ efficiency was estimated to be 16.25%. Our results show that $CH_3NH_3PbI_3$ has potential applications in single or multi-junction solar cells. Whereas $CsPbI_3$ has potential applications in multi-junction solar cell as wide band gap semiconductor.

5.1.2 Methylammonium Tin Triiodide Perovskite

In summary, we have systematically investigated the structural, mechanical and dynamical stabilities, electronic and optical properties of strained orthorhombic $CH_3NH_3SnI_3$ using density functional theory and many body perturbation theory calculations.

The calculated negative cohesive energies indicate that $CH_3NH_3SnI_3$ compound in the

orthorhombic phase is energetically stable. The dynamical stability has been studied at two different pressures 0 and 0.7 GPa. The relaxed system at zero pressure is dynamically unstable, while, at P= 0.7 GPa the orthorhombic $CH_3NH_3SnI_3$ perovskite is dynamically stable. This result is in agreement with experimental phase transition from tetragonal to orthorhombic phase reported by Xujie et al. [62] at 0.7 GPa. The equilibrium calculated elastic constants at 0.7 GPa satisfy all the mechanical stability criteria for an orthorhombic crystal, showing stability against the influence of external force.

The electronic properties were investigated by calculating the band structure, total density of states (TDOS) and partial density of states (PDOS), around the fundamental band gap, only iodine I and lead Sn contribute to the density of states. The organic cation $CH_3NH_3^+$ makes little contribution to the top valence band maximum and the bottom conduction band minimum. Therefore, the contribution of organic cation $CH_3NH_3^+$ to the Fermi level region is very weak. Our calculations showed that $CH_3NH_3SnI_3$ is a direct band gap semiconductor with an approximate density functional fundamental gap in the range of 0.73 eV to 1.21 eV, depending on the exchange-correlation approximation used.

Finally, with the help of the real part $\varepsilon_{\mathrm{re}}(\omega)$ and the imaginary part $\varepsilon_{\mathrm{im}}(\omega)$ of the dielectric tensor $\varepsilon(\omega)$ we derived all the desired frequency-dependent optical spectra such as absorption coefficient, refractive index, reflectivity and energy loss at BSE level of approximation. Moreover, the BSE absorption edges, using the Tauc plot, are found to be 1.27 eV, 1.36 eV and 1.20 eV in the a-, b and c-directions, respectively. This anisotropy seen in the BSE absorption edges are in good agreement with the experimental results 1.21 eV and 1.35 eV. It is well known that the DFT and GW gaps are approximate fundamental gaps, while the BSE gaps are approximate optical gaps. All these spectra revealed significant optical anisotropy. From the obtained band gap, we calculate the solar cell efficiency limits using Shockley-Queisser (SQ) model. The orthorhombic $CH_3NH_3SnI_3$ efficiency was estimated to be 40.08%. Therefore, $CH_3NH_3SnI_3$ may be potential material for solar cell, especially its potential in low band gap solar cell application. Although the solar efficiency of $CH_3NH_3SnI_3$ is high than that of $CH_3NH_3PbI_3$, we found that $CH_3NH_3SnI_3$ is only stable at 0.7 GPa.

5.2 Future Work

1. The orthorhombic $CH_3NH_3PbI_3$ optical properties are based on GW and BSE level of approximations. Our GW calculations were performed without including the effect of spin orbit coupling (SOC). Therefore, in order to compare the calculated optical spectra with experimental spectra, it is necessary to include the SOC. This requires a lot of computational resources.

2. Investigate the thermoelectric transport properties of the orthorhombic $CsPbI_3$ from a combination of first-principle calculations and semiclassical Boltzmann transport theory.

3. Study the lattice thermal conductivities and transport properties of the orthorhombic $CH_3NH_3SnI_3$ under pressure and this requires a lot of computational resources and time.

Appendix A

Hartree-Fock Approximation

The HartreeFock (HF) approximation method can be viewed as a variational method in which the wave functions of the many-electron system have the form of an antisymmetrised (fermion character of the electrons) product of one-electron wave functions. This limitation leads to an effective Schrödinger equation for the individual one-electron wave functions called orbitals with a potential determined by the orbitals occupied by the other electrons. Which causes the resulting equations to become non-linear in the orbitals, and the solution must be found iteratively in a self-consistency procedure [168]. The simplest approach is to assume a specific form for the many-body wave function which would be appropriate if the electrons were non-interacting particles, that is

$$\Psi^H(\mathbf{r}_i) = \Phi_1(\mathbf{r}_1)\Phi_2(\mathbf{r}_2)...\Phi(\mathbf{r}_N), \tag{A.0.1}$$

where the index i running over all electrons, $\Phi_i(\mathbf{r}_i)$ are states in which the individual electrons would be if this were a realistic approximation.These are single-particle states, normalized to unity. This is known as the Hartree approximation, and the total energy of the system turn into

$$E^H = < \Psi^H|\hat{H}|\Psi^H >. \tag{A.0.2}$$

From equation (2.2.4) we get

$$E^H = \sum_i \langle\Phi_i|\frac{\hbar^2}{2m_e}\sum_{i=1}^{N}\nabla_i^2 + \hat{V}_{\text{ion}}(\mathbf{r}_i)|\Phi_i\rangle + \frac{e^2}{2}\sum_{i\neq j}^{N}\sum_{i=1}^{N}\langle\Phi_i(\mathbf{r}_i)\Phi_j(\mathbf{r}_j)|\frac{1}{|\mathbf{r}_i-\mathbf{r}_j|}|\Phi_i(\mathbf{r}_i)\Phi_j(\mathbf{r}_j)\rangle. \tag{A.0.3}$$

By using a variational principle, one can obtain the Hartree single-particle equation

$$\left[-\frac{\hbar^2}{2m_e}\nabla_i^2+\hat{V}_{\text{ion}}(\mathbf{r}_i)+e^2\sum_{j\neq i}\langle\Phi_j(\mathbf{r}_j)|\frac{1}{|\mathbf{r}_i-\mathbf{r}_j|}|\Phi_j(\mathbf{r}_j)\rangle\right]\Phi_i(\mathbf{r}_i)=\epsilon_i\Phi_i(\mathbf{r}_i), \quad \text{(A.0.4)}$$

where ϵ_i are Lagrange multipliers, and the Hartree potential (includes only the Coulomb repulsion between electrons) is given by

$$V_i^{\text{H}}(\mathbf{r})=e^2\sum_{j\neq i}\langle\Phi_j(\mathbf{r}_j)|\frac{1}{|\mathbf{r}_i-\mathbf{r}_j|}|\Phi_j(\mathbf{r}_j)\rangle. \quad \text{(A.0.5)}$$

The next level of sophistication is to try to combine the fermionic nature of electrons in the many-body wave function $\Psi(\{\mathbf{r}_i\})$. For this purpose, we can nominate a wave function which is a properly anti-symmetrized version of the Hartree wave function. This is known as the HartreeFock (HF) approximation [145]. It consists of approximating the N-electron wave functions by an anti-symmetrized product of N-electron wave functions of the systems this product is usually referred to as a Slater determinant [68]. For simplicity we will neglect the spin of electrons and keep only the spatial degrees of freedom. Then the Hartree Fock (HF) wave function can be expressed as

$$\Psi(\{\mathbf{r}_i\sigma_i\})=\frac{1}{\sqrt{N!}}\begin{bmatrix}\Phi_1(\mathbf{r}_1\sigma_i) & \Phi_1(\mathbf{r}_2\sigma_i) & \dots & \Phi_1(\mathbf{r}_N\sigma_i)\\ \Phi_2(\mathbf{r}_1\sigma_i) & \Phi_2(\mathbf{r}_2\sigma_i) & \dots & \Phi_2(\mathbf{r}_N\sigma_i)\\ \vdots & \vdots & \ddots & \vdots\\ \Phi_N(\mathbf{r}_1\sigma_i) & \Phi_N(\mathbf{r}_2\sigma_i) & \dots & \Phi_N(\mathbf{r}_N\sigma_i)\end{bmatrix}, \quad \text{(A.0.6)}$$

where N is the total number of electrons, and the total energy with the HartreeFock wave function given by

$$E^{\text{HF}}=<\Psi^{\text{HF}}|\hat{\text{H}}|\Psi^{\text{HF}}> \quad \text{(A.0.7)}$$

$$\begin{aligned}E^{\text{HF}}=&\sum_i<\Phi_i|-\frac{\hbar^2}{2m_e}\nabla_i^2+\hat{V}_{\text{ion}}(\mathbf{r}_i)|\Phi_i>+\frac{e^2}{2}\sum_{ij(j\neq i)}<\Phi_i\Phi_j|\frac{1}{|\mathbf{r}_i-\mathbf{r}_j|}|\Phi_i\Phi_j>\\&-\frac{e^2}{2}\sum_{ij(j\neq i)}<\Phi_i\Phi_j|\frac{1}{|\mathbf{r}_i-\mathbf{r}_j|}|\Phi_j\Phi_i>.\end{aligned} \quad \text{(A.0.8)}$$

Using a variational calculation, one can obtain the single-particle HartreeFock equations

$$\left[-\frac{\hbar^2}{2m_e}\nabla_i^2 + \hat{V}_{\rm ion}(\mathbf{r}_i) + V_i^{\rm H}(\mathbf{r})\right]\Phi_i(\mathbf{r}) - e^2\sum_{j\neq i} < \Phi_j|\frac{1}{|\mathbf{r}_i - \mathbf{r}_j|}|\Phi_i > \phi_j(\mathbf{r}) = \epsilon_i\Phi_i(\mathbf{r}). \tag{A.0.9}$$

These equations differ from the Hartree equation (A.0.4) by additional term, this term is known as the exchange term which describes the effects of exchange between electrons. One can construct a single-electron exchange density as

$$\rho_i(\mathbf{r}) = |\Phi_i(\mathbf{r})|^2 \tag{A.0.10}$$

$$\rho(\mathbf{r}) = \sum_i \rho_i(\mathbf{r}). \tag{A.0.11}$$

The Hartree potential in equation (A.0.5) can be written in a different way

$$V_i^{\rm H}(\mathbf{r}) = e^2\sum_{j\neq i}\int\frac{\rho_j(\mathbf{r}')}{|\mathbf{r}-\mathbf{r}'|}d\mathbf{r}' \tag{A.0.12}$$

$$V_i^{\rm H}(\mathbf{r}) = e^2\sum_{j\neq i}\int\frac{\rho(\mathbf{r}') - \rho_j(\mathbf{r}')}{|\mathbf{r}-\mathbf{r}'|}d\mathbf{r}'. \tag{A.0.13}$$

The single-particle exchange density can be constructed as

$$\rho_i(\mathbf{r},\mathbf{r}')^X = \sum_{j\neq i}\frac{\Phi_i(\mathbf{r}')\Phi_i^*(\mathbf{r})\Phi_j(\mathbf{r})\Phi_j^*(\mathbf{r}')}{\Phi_i(\mathbf{r})\Phi_i^*(\mathbf{r})}, \tag{A.0.14}$$

so the single-particle Hartree-Fock equations can be written as

$$\left[-\frac{\hbar^2}{2m_e}\nabla_i^2 + \hat{V}_{\rm ion}(\mathbf{r}_i) + V_i^{\rm H}(\mathbf{r}) + V_i^{\rm X}(\mathbf{r})\right]\Phi_i(\mathbf{r}) = \epsilon_i\Phi_i(\mathbf{r}), \tag{A.0.15}$$

where $V_i^X(\mathbf{r})$ is the exchange potential

$$V_i^{\rm X}(\mathbf{r}) = -e^2\int\frac{\rho_i^{\rm X}(\mathbf{r}),(\mathbf{r}')}{|\mathbf{r}-\mathbf{r}'|}d\mathbf{r}'. \tag{A.0.16}$$

The Hartree and exchange potentials give the potential for electronelectron interaction in the Hartree Fock approximation (HF)

$$V_i^{\rm HF}(\mathbf{r}) = e^2\int\frac{\rho_i(\mathbf{r}')}{|\mathbf{r}-\mathbf{r}'|}d\mathbf{r}' - e^2\int\frac{\rho_i(\mathbf{r}') - \rho_i^{\rm HF}(\mathbf{r},\mathbf{r}')}{|\mathbf{r}-\mathbf{r}'|}d\mathbf{r}', \tag{A.0.17}$$

where the first term is the total Coulomb repulsion potential of electrons, and the second term is the effect of fermionic exchange.The next expression for the total electronelectron interaction potential [145]

$$V_i^{\mathrm{HF}}(\mathbf{r}) = e^2 \int \frac{\rho_i(\mathbf{r}') - \rho_i^{\mathrm{HF}}(\mathbf{r}, \mathbf{r}')}{|\mathbf{r} - \mathbf{r}'|} d\mathbf{r}'. \tag{A.0.18}$$

Appendix B

Green's Function

Quasi-particle properties, and expectation values of single-particle operators of a many-body system are determined by the single-particle Green function G [104]. Mathematically, the Green function of a linear operator $\mathcal{L}$ can be defined as

$$[z - \mathcal{L}(r)]G(x, x^{'}; z) = \delta(x - x^{'}), \tag{B.0.1}$$

where $\delta(x - x^{'})$ is Dirac's delta function. For a single quantum particle in an external potential $v_{\text{ext}}(r)$ one has [169]

$$\left[-\frac{\hbar}{2m}\nabla^2 + v_{\text{ext}}(\mathbf{r}) - E \right] G^o(\mathbf{r}, \mathbf{r}^{'}; E) = -\delta(\mathbf{r} - \mathbf{r}^{'}). \tag{B.0.2}$$

The one-particle Green function $G(\mathbf{r}, \mathbf{r}^{'}; t, t^{'})$, describes the probability of finding an electron at position $\mathbf{r}$ at time t, if another electron is added (or removed) at position $\mathbf{r}^{'}$ at time t'. In the energy domain, the Green's function is the solution of the Schrödinger equation

$$\left[-\frac{\hbar}{2m}\nabla^2 + v_{\text{ext}}(\mathbf{r}) - E \right] G(\mathbf{r}, \mathbf{r}^{'}; E) + \int \Sigma(\mathbf{r}, \mathbf{r}^{''}; E) G(\mathbf{r}^{''}, \mathbf{r}^{'}; E) d\mathbf{r}^{''} = -\delta(\mathbf{r} - \mathbf{r}^{'}), \tag{B.0.3}$$

where $\Sigma(\mathbf{r}, \mathbf{r}^{''}; \mathbf{E})$ is the self-energy operator,it is energy-dependent, non-local and non-Hermitian operator.

If the exact Green function $G_o(\mathbf{r}, \mathbf{r}^{'}; \mathbf{E})$ of a related reference system is known exactly, then $G(\mathbf{r}, \mathbf{r}^{'}; \mathbf{E})$ of the real system can be calculated using many-body perturbation

theory through Dyson's equation

$$G(\mathbf{r},\mathbf{r}^{'};E) = G_o(\mathbf{r},\mathbf{r}^{'};E) + \int\int G_o(\mathbf{r},\mathbf{r}_1;E)\Sigma(\mathbf{r}_1,\mathbf{r}_2;E)G(\mathbf{r}_2,\mathbf{r}^{'};E)d\mathbf{r}_1 d\mathbf{r}_2, \quad \text{(B.0.4)}$$

If one takes the Kohn-Sham system as the reference system, the Greens function assumes the form

$$G_o(\mathbf{r},\mathbf{r}^{'};E) = \sum_n \frac{\Psi_n^{\mathrm{QP}}(\mathbf{r})\Psi_n^{\mathrm{QP}*}(\mathbf{r}^{'})}{E-E_n}, \quad \text{(B.0.5)}$$

where $\Psi_n(\mathbf{r})$, E_n are the solution of the single-particle equation and eigenvalues, respectively. The problem is how to calculate the self-energy, which contains all the exchange and correlation effects [64]. If $|N,|0\rangle$ stands for the ground state of the N-electron system, the one-particle Green's function is defined as

$$\begin{aligned} G(\mathbf{r},\mathbf{r}^{'};t,t^{'}) &= -i\left\langle N,0\right| T[\hat{\Psi}(\mathbf{r}t)\hat{\Psi}^*(\mathbf{r}^{'}t^{'})]\left|N,0\right\rangle \\ &= \begin{cases} -i\left\langle N,0\right| T[\hat{\Psi}(\mathbf{r}t)\hat{\Psi}^*(\mathbf{r}^{'}t^{'})]\left|N,0\right\rangle & \text{if } t > t' \\ i\left\langle N,0\right| T[\hat{\Psi}^*(\mathbf{r}^{'}t^{'})\hat{\Psi}(\mathbf{r}t)]\left|N,0\right\rangle & \text{if } t^{'} > t \end{cases}. \end{aligned} \quad \text{(B.0.6)}$$

Starting from the equation of motion for the fermion creation and annihilation operators in the Heisenberg representation and the representation of one-particle Greens function in equation (B.0.6), one gets the differential form of Dyson's equation

$$\left[i\frac{\partial}{\partial t} - \left(-\frac{\nabla^2}{2} + V_{\mathrm{H}}(\mathbf{r}) + V_{\mathrm{ext}}(\mathbf{r})\right)\right]G(12) - \int d3\Sigma(13)G(32) = \delta(12). \quad \text{(B.0.7)}$$

Here, 1, 2 and 3 are short notation for a combined space and time coordinates, e.g., (1)=($\mathbf{r}$,t) [107].

Appendix C

Vienna Ab-initio Simulation Package (VASP)

Vienna Ab-initio Simulation Package (VASP) is a complex package for performing ab-initio simulations for quantum mechanical molecular dynamics (MD) using either pseudopotentials, or the projector-augmented wave method and a plane wave basis set [170, 171]. The approach implemented in VASP is based on the local-density approximation where the variation quantity is the free energy here, and the exact evaluation of the instantaneous electronic ground state at each molecular dynamic time step.

In VASP, the electron-ion interaction was described by Vanderbilt pseudopotentials or by the projector-augmented wave (PAW) method with plane wave basis functionals. For transition metals, the Vanderbilt pseudopotential and the PAW method allow for considerable reduction in the number of plane-waves per atom. Using VASP code, forces and stress tensor can be calculated which can used the relax atoms into their ground-state.

VASP computes an approximate solution to the many-body Schrödinger equation, either by using density functional theory (DFT) (solving Kohn-Sham equation), or within the HF approximation (solving the Roothaan equations), hybrid functionals. Furthermore, Green's function methods and many-body perturbation theory (MBPT).

As minimal setup, VASP package requires input files and the calculation will be done in a work directory, where the input files must be created. The four most basic and important

input files in VASP are the INCAR, POSCAR, POTCAR and KPOINTS files. All VASP calculations require (at least) these files to perform the DFT calculations. While the files are described briefly in the following, no specific examples are given. Following are the most important input files in all VASP calculations.

INCAR file

In general, the INCAR file is the central input file of VASP where the user can define the starting options for a calculation. *It determines what to do and how to do it.* It contains large number of options define the size, scope and all details of the calculations. Options that are not included in the INCAR file manually are automatically set to default values, where the choice of many of these options depends on the structure under study or the computer resources to be used.

POTCAR file

The POTCAR file defines the pseudopotentials to be used for each element in the system used in the calculation. It is also contains information about the functionals used, the atoms mass, valence, the energy of the atomic reference configuration for which the pseudopotential was created and other features. The order of pseudopotentials in the POTCAR file should match those in the POSCAR and INCAR files.

POSCAR file

The POSCAR file gives the position of each atom, length and direction of the lattice vectors on the unit cell or supercell.

KPOINTS file

The KPOINTS file contains k-point coordinates and weights or mesh size for creating the k-point grid. While one can explicitly defined the k-point mesh, it is usually calculated by the Monkhorst and Pack method.

Appendix D

Dielectric Function

The complex dielectric function $\varepsilon(\omega)$ is the fundamental quantity used to determine optical properties of a material. It describes the response of the material to electromagnetic radiation. For a periodic system and at a coarse scale, response function is homogeneous, while the total macroscopic electric field $\mathbf{E}$ follows the periodicity of the external perturbation $\mathbf{E}_{\text{ext}}$, but the total microscopic electric field $\mathbf{e}$ oscillates on the scale of a primitive cell. Therefore, it is crucial to differentiate between the macroscopic and microscopic dielectric functions. The $\mathbf{E}$ and $\mathbf{E}_{\text{ext}}$ are connected by the macroscopic dielectric function ε_{mac} via

$$\mathbf{E}(\mathbf{r},\omega) = \int d\mathbf{r}^{'} \varepsilon^{-1}_{\text{mac}}(\mathbf{r}-\mathbf{r}^{'},\omega)\mathbf{E}_{\text{ext}}(\mathbf{r}^{'},\omega). \tag{D.0.1}$$

Because the material is homogeneous, the macroscopic dielectric function depends only on the difference $\mathbf{r}-\mathbf{r}^{'}$. Similar to equation (D.0.1), the microscopic dielectric function ε fulfils [105, 110]:

$$\mathbf{e}(\mathbf{r},\omega) = \int d\mathbf{r}^{'} \varepsilon^{-1}(\mathbf{r}-\mathbf{r}^{'},\omega)\mathbf{E}_{\text{ext}}(\mathbf{r}^{'},\omega). \tag{D.0.2}$$

The macroscopic dielectric function ε_{mac} couples the total electric field $\mathbf{E}$ in a material to the external field $\mathbf{E}_{\text{ext}}$. The response to change in electric field $\mathbf{E}$ is given by

$$\mathbf{E} = \varepsilon^{-1}_{\text{mac}}\mathbf{E}_{\text{ext}}, \tag{D.0.3}$$

where ε_{mac} (3×3 Cartesian tensor) is the macroscopic dielectric function. In a macroscopic system, the solution of equation (D.0.3) is a product of momentum and frequency

space. The total potential v_{tot} on the system is divided into external potential v_{ext} (generated due to the external charge density ρ_{ext}) and induced potential v_{ind} (generated due to the induced charge density ρ_{ind}) [110], that is

$$v_{\text{tot}} = v_{\text{ext}} + v_{\text{ind}}. \tag{D.0.4}$$

Therefore, in momentum space (in the long-wavelength) equation (D.0.3) takes the form

$$v_{\text{tot}} = \varepsilon^{-1} v_{\text{ext}}. \tag{D.0.5}$$

Within the linear response regime (weak external fields) the response function (reducible polarizability) χ and the screened response function (irreducible polarizability) P take the form

$$\begin{aligned} \rho_{\text{ind}} &= \chi v_{\text{ext}} \\ v_{\text{ind}} &= P v_{\text{tot}}. \end{aligned} \tag{D.0.6}$$

Moreover, we can write the connection between the dielectric function ε and its inverse ε^{-1} as

$$\varepsilon = 1 - vP, \tag{D.0.7}$$

$$\varepsilon^{-1} = 1 + v\chi, \tag{D.0.8}$$

where χ and P are related by

$$\chi = P + Pv\chi. \tag{D.0.9}$$

Equation (D.0.9) has the form of a Dyson equation. From the above discussion, one can conclude that the dielectric function ε can be computed if the response of the system to the change in either the total potential v_{tot} (equation D.0.7) or the external potential v_{ext} (equation D.0.8) is known [105, 110].

The microscopic dielectric function ε is invariant only by a translation of lattice vector $\mathbf{R}$, i.e.

$$\varepsilon(\mathbf{r}; \mathbf{r}', \omega) = \varepsilon(\mathbf{r} + \mathbf{R}; \mathbf{r}' + \mathbf{R}, \omega). \tag{D.0.10}$$

Using the invariant property in equation (D.0.10), it is straightforward to show that

[110]

$$\mathbf{e}(\mathbf{q}+\mathbf{G},\omega)=\sum_{\mathbf{G}'}\varepsilon^{-1}_{\mathbf{G},\mathbf{G}'}(\mathbf{q},\omega)\mathbf{E}_{\text{ext}}(\mathbf{q}+\mathbf{G}',\omega). \tag{D.0.11}$$

To study the relation between the macroscopic and microscopic dielectric function, we link the macroscopic electric field to the microscopic one

$$\mathbf{E}(\mathbf{R},\omega)=\frac{1}{V}\int_{V(\mathbf{R})}\mathrm{d}\mathbf{r}\mathbf{e}(\mathbf{r},\omega), \tag{D.0.12}$$

where $V(\mathbf{R})$ indicates integration over the unit cell around position $\mathbf{R}$. Using Fourier transform of the microscopic dielectric field $\mathbf{e}(\mathbf{r},\omega)$ [105, 172], one can write the macroscopic electric field $\mathbf{E}(\mathbf{R},\omega)$ as

$$\mathbf{E}(\mathbf{R},\omega)=\sum_{\mathbf{G}}\int_{BZ}\frac{\mathrm{d}\mathbf{q}}{(2\pi)^3}\mathbf{e}(\mathbf{q}+\mathbf{G},\omega)\frac{1}{V}\int_{V(\mathbf{R})}\mathrm{d}\mathbf{r}e^{i(\mathbf{q}+\mathbf{G})\mathbf{r}}. \tag{D.0.13}$$

Assuming that ($\mathbf{q}\ll\mathbf{G}$),

$$\mathbf{E}(\mathbf{R},\omega)=\int_{BZ}\frac{\mathrm{d}\mathbf{q}}{(2\pi)^3}e^{i\mathbf{q}\mathbf{R}}\mathbf{e}(\mathbf{q},\omega). \tag{D.0.14}$$

The Fourier transform of the macroscopic electric field is

$$\mathbf{E}(\mathbf{R},\omega)=\sum_{\mathbf{G}}\int_{BZ}\frac{\mathrm{d}\mathbf{q}}{(2\pi)^3}\mathbf{E}(\mathbf{q}+\mathbf{G},\omega)e^{i(\mathbf{q}+\mathbf{G})\mathbf{R}}. \tag{D.0.15}$$

Comparing equation (D.0.14) and (D.0.15), yields the relation between macroscopic and microscopic fields

$$\mathbf{E}(\mathbf{q}+\mathbf{G},\omega)=\mathbf{e}(\mathbf{q},\omega)\delta_{\mathbf{G},0}. \tag{D.0.16}$$

Since the external field $\mathbf{E}_{\text{ext}}$ is macroscopic, it can be written as

$$\mathbf{E}_{\text{ext}}(\mathbf{q}+\mathbf{G},\omega)=\mathbf{E}_{\text{ext}}(\mathbf{q},\omega)\delta_{\mathbf{G},0}. \tag{D.0.17}$$

Therefore,

$$\mathbf{E}(\mathbf{q},\omega)=\mathbf{e}(\mathbf{q},\omega)=\sum_{\mathbf{G}'}\varepsilon^{-1}_{0\mathbf{G}'}(\mathbf{q},\omega)\mathbf{E}_{\text{ext}}(\mathbf{q},\omega)\delta_{\mathbf{G}',0}=\varepsilon^{-1}_{00}\mathbf{E}_{\text{ext}}(\mathbf{q},\omega). \tag{D.0.18}$$

Comparing equation (D.0.3) and equation (D.0.18), the relation between macroscopic

and microscopic dielectric function is given as:

$$\varepsilon^{-1}_{\mathrm{mac}}(\mathbf{q},\omega) = \varepsilon^{-1}_{00}(\mathbf{q},\omega), \tag{D.0.19}$$

$$\varepsilon_{\mathrm{mac}}(\mathbf{q},\omega) = \frac{1}{\varepsilon^{-1}_{00}(\mathbf{q},\omega)}. \tag{D.0.20}$$

The macroscopic dielectric function is therefore obtained by inverting the microscopic dielectric function with respect to $\mathtt{G}$, $\mathtt{G}'$, taking the head ($\mathtt{G}$=$\mathtt{G}'$=0) of the resulting matrix and inverting 3×3 tensor. In a real solid, the microscopic electric field often varies rapidly over the unit cell compared to the external field. This is known as the local field effect. Only for materials that are also homogeneous on the microscopic scale (like the homogeneous electron gas), the off-diagonal elements of $\varepsilon^{-1}_{\mathtt{G},\mathtt{G}'}$ are zero and no local field effects are present:

$$\varepsilon_{\mathrm{mac}}(\mathbf{q},\omega) = \varepsilon_{00}(\mathbf{q},\omega). \tag{D.0.21}$$

This approximation is usually referred to as neglect of local field effects.

Appendix E

Efficiency of Halide Perovskites

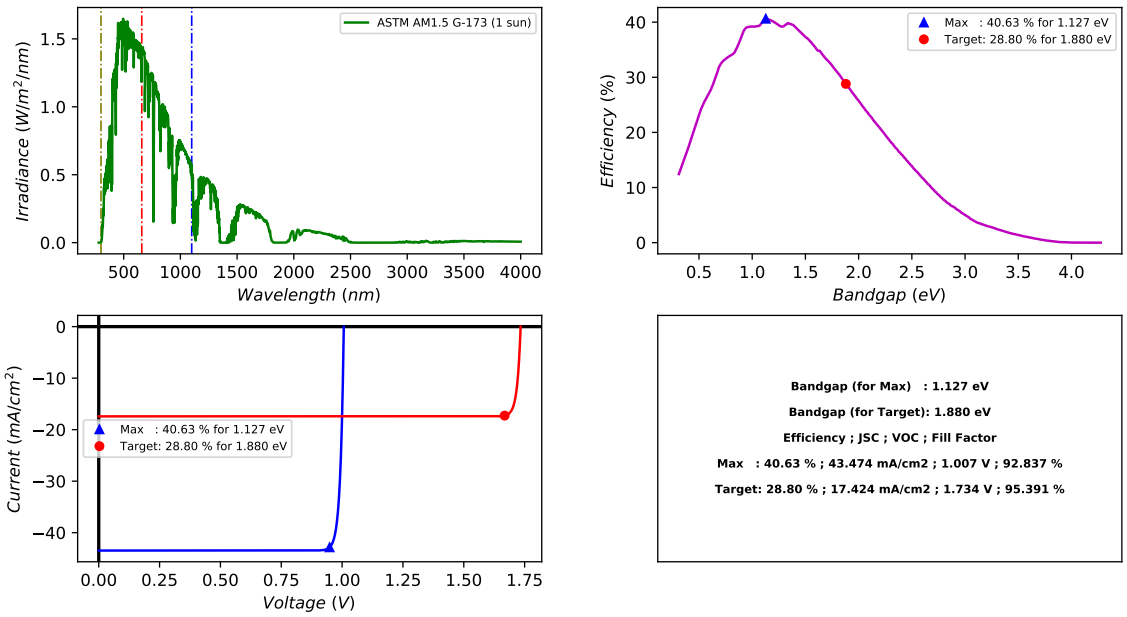


Figure E.1: Estimated efficiency of $CH_3NH_3PbI_3$ (red point) using Shockley-Queisser model.

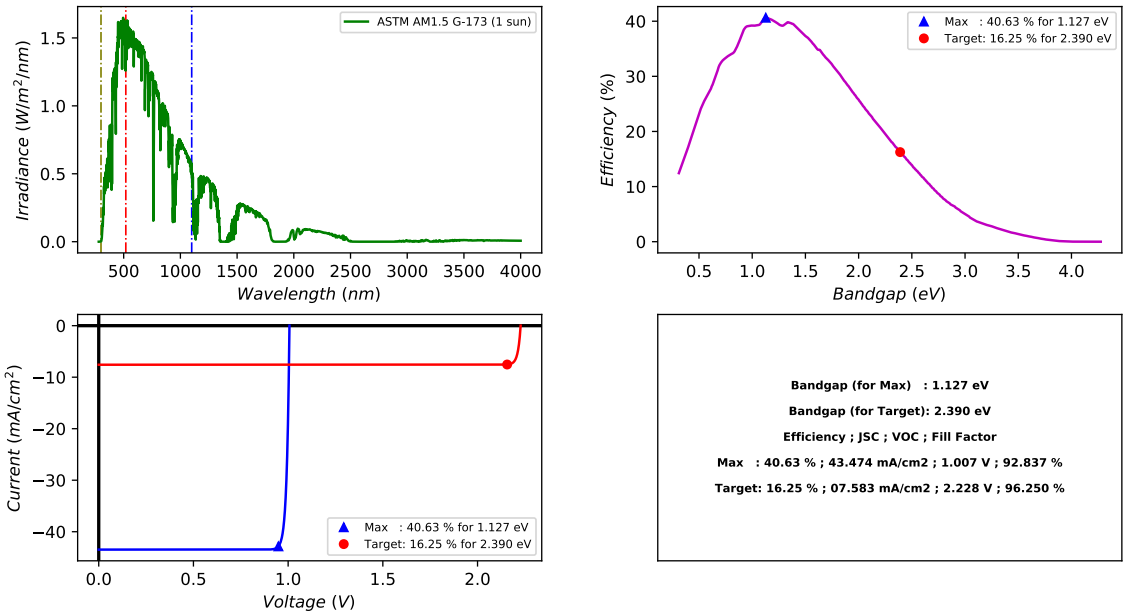


Figure E.2: Estimated efficiency of $CsPbI_3$ (red point) using Shockley-Queisser model.

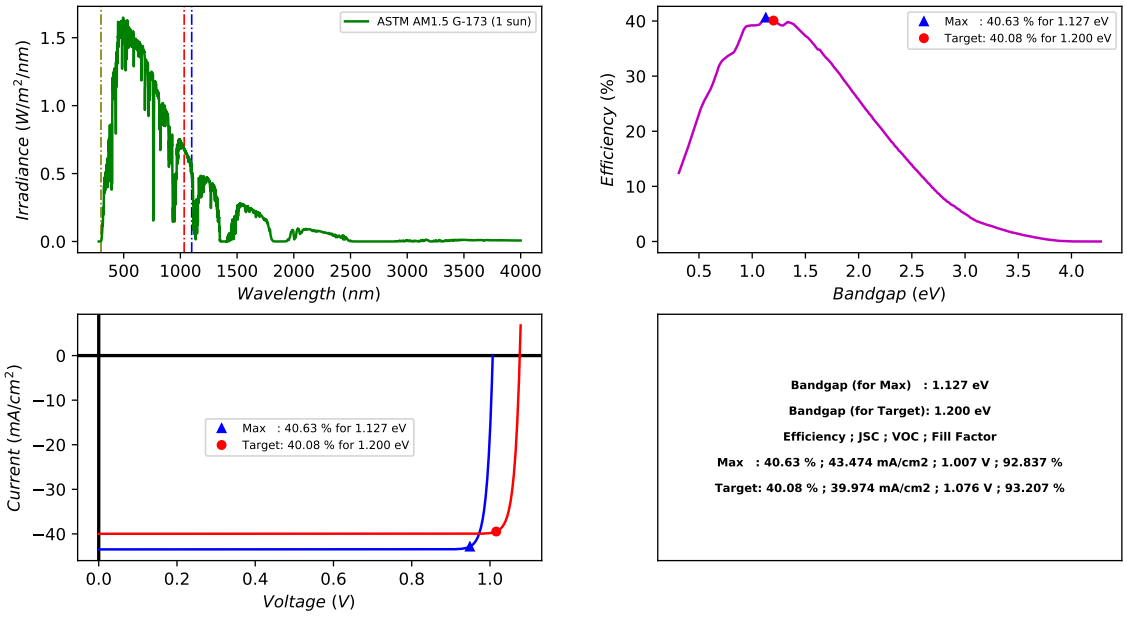


Figure E.3: Estimated efficiency of $CH_3NH_3SnI_3$ (red point) using Shockley-Queisser model.

References

[1] Ibrahim Omer A. Ali, Daniel P. Joubert, and Mohamed S. H. Suleiman. First-principles calculations of the electronic and optical properties of $CH_3NH_3PbI_3$ for photovoltaic applications. *Materials Today: Proceedings*, 5(4):10570–10576, 2018.

[2] Ibrahim Omer A. Ali, Daniel P. Joubert, and Mohammed S. H. Suleiman. A theoretical investigation of structural, mechanical, electronic and thermoelectric properties of orthorhombic $CH_3NH_3PbI_3$. *The European Physical Journal B*, 91(10):263, Oct 2018.

[3] Ibrahim Omer Abdallah, Daniel P Joubert, and Mohammed SH Suleiman. First-principles investigation of lattice thermal conductivity and structural stability of $CH_3NH_3PbI_3$. In *the 62nd Annual Conference of the South African Institute of Physics*. edited by Prof. Japie Engelbrecht (SU/2017), pp. 2–7. ISBN = 978-0-620-82077-6.

[4] Ibrahim Omer Abdallah, Daniel P Joubert, and Mohammed SH Suleiman. Investigation of thermoelectric properties of $CH_3NH_3PbI_3$: Density functional theory and boltzmann transport calculations. In *the 62nd Annual Conference of the South African Institute of Physics*. edited by Prof. Japie Engelbrecht (SU/2017), pp. 8–13. ISBN = 978-0-620-82077-6.

[5] Wahyu Setyawan and Stefano Curtarolo. High-throughput electronic band structure calculations: Challenges and tools. *Computational Materials Science*, 49(2):299–312, 2010.

[6] M. Salim, M. D. Shahadat Hussain Chowdhury, M. S. Hossain, and M. A. Islam. A micro-review on prospects and challenges of perovskite materials in organic-inorganic hybrid solar cell applications. *Digest Journal of Nanomaterials and Biostructures*, 10(4):1289–1302, 2015.

[7] Gavin Conibeer. Third-generation photovoltaics. *Materials Today*, 10(11):42–50, 2007.

[8] Martin A. Green, Anita Ho-Baillie, and Henry J. Snaith. The emergence of perovskite solar cells. *Nature Photonics*, 8(7):506–514, 2014.

[9] Qi Chen, Nicholas De Marco, Yang Michael Yang, Tze-Bin Song, Chun-Chao Chen, Hongxiang Zhao, Ziruo Hong, Huanping Zhou, and Yang Yang. Under the spotlight: The organic–inorganic hybrid halide perovskite for optoelectronic applications. *Nano Today*, 10(3):355–396, 2015.

[10] Zhang Yue-Yu, Chen Shiyou, Xu Peng, Xiang Hongjun, Gong Xin-Gao, Walsh Aron, and Wei Su-Huai. Intrinsic instability of the hybrid halide perovskite semiconductor $CH_3NH_3PbI_3$. *Chinese Physics Letters*, 35(3):36104–036104, 2018.

[11] Paul Hersch and Kenneth Zweibel. Basic photovoltaic principles and methods. Technical report, Solar Energy Research Inst., Golden, CO (USA), 1982.

[12] Jenny Nelson. *The physics of solar cells*. World Scientific Publishing Company, 2003.

[13] Christiana Honsberg and Stuart Bowden. Pv education. *ORG.(access April-June 2013) http://pveducation. org/pvcdrom/properties-of-sunlight/sun-position-calculator*, 2014.

[14] William Shockley and Hans J Queisser. Detailed balance limit of efficiency of p-n junction solar cells. *Journal of applied physics*, 32(3):510–519, 1961.

[15] Abderrahmane Belghachi. Theoretical calculation of the efficiency limit for solar cells. In *Solar Cells-New Approaches and Reviews*. IntechOpen, 2015.

[16] MC Hanna and AJ Nozik. Solar conversion efficiency of photovoltaic and photoelectrolysis cells with carrier multiplication absorbers. *Journal of Applied Physics*, 100(7):074510, 2006.

[17] Albert Polman, Mark Knight, Erik C Garnett, Bruno Ehrler, and Wim C Sinke. Photovoltaic materials: Present efficiencies and future challenges. *Science*, 352(6283):aad4424, 2016.

[18] Thomas Johann Seebeck. Ueber die magnetische polarisation der metalle und erze durch temperaturdifferenz. *Annalen der Physik*, 82(3):253–286, 1826.

[19] JCA Peltier. Investigation of the heat developed by electric currents in homogeneous materials and at the junction of two different conductors. *Ann. Chim. Phys*, 56(1834):371, 1834.

[20] Terry M. Tritt and M. A. Subramanian. Thermoelectric materials, phenomena, and applications: A bird's eye view. *MRS Bulletin*, 31(3):188198, 2006.

[21] SP Beeby, Z Cao, and A Almussallam. Kinetic, thermoelectric and solar energy harvesting technologies for smart textiles. In *Multidisciplinary Know-How for Smart-Textiles Developers*, pages 306–328. Elsevier, 2013.

[22] H.J. Goldsmid. *Introduction to Thermoelectricity*. Springer Series in Materials Science. Springer Berlin Heidelberg, 2016.

[23] A.V. Da Rosa. *Fundamentals of Renewable Energy Processes*. Elsevier Science, 2012.

[24] Xiao Zhang and Li-Dong Zhao. Thermoelectric materials: Energy conversion between heat and electricity. *Journal of Materiomics*, 1(2):92 – 105, 2015.

[25] Gustav Rose. Beschreibung einiger neuen mineralien des urals. *Annalen der Physik*, 124(12):551–573, 1839.

[26] A. Navrotsky and D.J. Weidner. *Perovskite: a structure of great interest to geophysics and materials science*. Geophysical monograph. American Geophysical Union, 1989.

[27] Andrew B. Wong Dandan Zhang Minliang Lai Yi Yu Qiao Kong Elbert Lin Jeffrey J. Urban Jeffrey C. Grossman Woochul Lee, Huashan Li and Peidong Yang. Ultralow thermal conductivity in all-inorganic halide perovskites. *Proceedings of the National Academy of Sciences*, 114(33):8693–8697, 2017.

[28] Robert D Shannon. Revised effective ionic radii and systematic studies of interatomic distances in halides and chalcogenides. *Acta Crystallographica section A:*

Crystal Physics, Diffraction, Theoretical and General Crystallography, 32(5):751–767, 1976.

[29] Victor Moritz Goldschmidt. Die gesetze der krystallochemie. *Naturwissenschaften*, 14(21):477–485, 1926.

[30] Constantinos C. Stoumpos, Christos D. Malliakas, and Mercouri G. Kanatzidis. Semiconducting tin and lead iodide perovskites with organic cations: phase transitions, high mobilities, and near-infrared photoluminescent properties. *Inorganic Chemistry*, 52(15):9019–9038, 2013.

[31] Edoardo Mosconi, Paolo Umari, and Filippo De Angelis. Electronic and optical properties of mixed Sn–Pb organohalide perovskites: a first principles investigation. *Journal of Materials Chemistry A*, 3(17):9208–9215, 2015.

[32] San-Dong Guo and Jian-Li Wang. Potential thermoelectric materials $CsMI_3$ (M= Sn and Pb) in perovskite structures from first-principles calculations. *RSC Advances*, 6(103):101552–101559, 2016.

[33] C. Møller, C.K. Møller, and Kongelige Danske videnskabernes selskab. *The structure of cæsium plumbo iodide CsPbI3*. Number v. 32 in Mathematisk-fysiske meddelelser. Munksgaard, 1959.

[34] Dieter Weber. $CH_3NH_3PbX_3$, ein Pb(II)-system mit kubischer perowskitstruktur / $CH_3NH_3PbX_3$ a Pb(II)-system with cubic perovskite structure. *Zeitschrift für Naturforschung B*, 33(12):1443–1445, 1978.

[35] Tom Baikie, Yanan Fang, Jeannette M. Kadro, Martin Schreyer, Fengxia Wei, Subodh G. Mhaisalkar, Michael Graetzel, and Tim J. White. Synthesis and crystal chemistry of the hybrid perovskite $(CH_3NH_3)PbI_3$ for solid-state sensitised solar cell applications. *Journal of Materials Chemistry A*, 1(18):5628–5641, 2013.

[36] Mark T. Weller, Oliver J. Weber, Paul F. Henry, Antonietta M. Di Pumpo, and Thomas C. Hansen. Complete structure and cation orientation in the perovskite photovoltaic methylammonium lead iodide between 100 and 352 K. *Chemical Communications*, 51(20):4180–4183, 2015.

[37] Mingzhen Liu, Michael B. Johnston, and Henry J. Snaith. Efficient planar heterojunction perovskite solar cells by vapour deposition. *Nature*, 501(7467):395–398, 2013.

[38] Wan-Jian Yin, Ji-Hui Yang, Joongoo Kang, Yanfa Yan, and Su-Huai Wei. Halide perovskite materials for solar cells: a theoretical review. *Journal of Materials Chemistry A*, 3(17):8926–8942, 2015.

[39] Y. H. Chang, C. H. Park, and K. Matsuishi. First-principles study of the structural and the electronic properties of the lead-halide-based inorganic-organic perovskites $(CH_3NH_3)PbX_3$ and $CsPbX_3$ (X= Cl, Br, I). *Journal of the Korean Physical Society*, 44:889–893, 2004.

[40] Yun Wang, Tim Gould, John F. Dobson, Haimin Zhang, Huagui Yang, Xiangdong Yao, and Huijun Zhao. Density functional theory analysis of structural and electronic properties of orthorhombic perovskite $CH_3NH_3PbI_3$. *Physical Chemistry Chemical Physics*, 16(4):1424–1429, 2014.

[41] Federico Brivio, Keith T. Butler, Aron Walsh, and Mark Van Schilfgaarde. Relativistic quasiparticle self-consistent electronic structure of hybrid halide perovskite photovoltaic absorbers. *Physical Review B*, 89(15):155204, 2014.

[42] Jing Feng. Mechanical properties of hybrid organic-inorganic $CH_3NH_3BX_3$ (B= Sn, Pb; X= Br, I) perovskites for solar cell absorbers. *APL Materials*, 2(8):081801, 2014.

[43] Andrea Pisoni, Jacim Jacimovic, Osor S. Barisic, Massimo Spina, Richard Gaál, László Forró, and Endre Horváth. Ultra-low thermal conductivity in organic–inorganic hybrid perovskite $CH_3NH_3PbI_3$. *The Journal of Physical Chemistry Letters*, 5(14):2488–2492, 2014.

[44] Xavier Mettan, Riccardo Pisoni, Péter Matus, Andrea Pisoni, Jacim Jacimovic, Bálint Náfrádi, Massimo Spina, Davor Pavuna, László Forró, and Endre Horváth. Tuning of the thermoelectric figure of merit of $CH_3NH_3MI_3$ (M= Pb, Sn) photovoltaic perovskites. *The Journal of Physical Chemistry C*, 119(21):11506–11510, 2015.

[45] Xiaokun Gu Qian, Xin and Ronggui Yang. Lattice thermal conductivity of organic-inorganic hybrid perovskite $CH_3NH_3PbI_3$. *Applied Physics Letters*, 108(6):063902, 2016.

[46] Tianqi Zhao, Dong Wang, and Zhigang Shuai. Doping optimization of organic-inorganic hybrid perovskite $CH_3NH_3PbI_3$ for high thermoelectric efficiency. *Syn-*

thetic Metals, 225:108–114, 2017.

[47] Yuping He and Giulia Galli. Perovskites for solar thermoelectric applications: A first principle study of $CH_3NH_3AI_3$ (A= Pb and Sn). *Chemistry of Materials*, 26(18):5394–5400, 2014.

[48] Changhoon Lee, Jisook Hong, Alessandro Stroppa, Myung-Hwan Whangbo, and Ji Hoon Shim. Organic–inorganic hybrid perovskites ABI_3 (A=CH_3NH_3, NH_2CHNH_2; B=Sn, Pb) as potential thermoelectric materials: a density functional evaluation. *Rsc Advances*, 5(96):78701–78707, 2015.

[49] D. M. Trots and S. V. Myagkota. High-temperature structural evolution of caesium and rubidium triiodoplumbates. *Journal of Physics and Chemistry of Solids*, 69(10):2520–2526, 2008.

[50] Murad Ahmad, Gul Rehman, Liaqat Ali, M. Shafiq, R. Iqbal, Rashid Ahmad, Tahirzeb Khan, S. Jalali-Asadabadi, Muhammad Maqbool, and Iftikhar Ahmad. Structural, electronic and optical properties of $CsPbX_3$ (X= Cl, Br, I) for energy storage and hybrid solar cell applications. *Journal of Alloys and Compounds*, 705:828–839, 2017.

[51] Giles E Eperon, Giuseppe M Paterno, Rebecca J Sutton, Andrea Zampetti, Amir Abbas Haghighirad, Franco Cacialli, and Henry J Snaith. Inorganic caesium lead iodide perovskite solar cells. *Journal of Materials Chemistry A*, 3(39):19688–19695, 2015.

[52] Jakoah Brgoch, Anna J Lehner, Michael Chabinyc, and Ram Seshadri. Ab initio calculations of band gaps and absolute band positions of polymorphs of $RbPbI_3$ and $CsPbI_3$: implications for main-group halide perovskite photovoltaics. *The Journal of Physical Chemistry C*, 118(48):27721–27727, 2014.

[53] Woon Seok Yang, Jun Hong Noh, Nam Joong Jeon, Young Chan Kim, Seungchan Ryu, Jangwon Seo, and Sang Il Seok. High-performance photovoltaic perovskite layers fabricated through intramolecular exchange. *Science*, 348(6240):1234–1237, 2015.

[54] Yue-Yu Zhang, Shiyou Chen, Peng Xu, Hongjun Xiang, Xin-Gao Gong, Aron Walsh, and Su-Huai Wei. Intrinsic instability of the hybrid halide perovskite semiconductor $CH_3NH_3PbI_3$. *Chinese Physics Letters*, 35(3):036104, 2018.

[55] Nakita K. Noel, Samuel D. Stranks, Antonio Abate, Christian Wehrenfennig, Simone Guarnera, Amir-Abbas Haghighirad, Aditya Sadhanala, Giles E. Eperon, Sandeep K. Pathak, Annamaria Petrozza Laura M. Herz Johnston, Michael B. Johnston, and Henry J. Snaith. Lead-free organic–inorganic tin halide perovskites for photovoltaic applications. *Energy & Environmental Science*, 7(9):3061–3068, 2014.

[56] Jing Feng and Bing Xiao. Effective masses and electronic and optical properties of nontoxic $MASnX_3$ (X= Cl, Br, and I) perovskite structures as solar cell absorber: A theoretical study using HSE06. *The Journal of Physical Chemistry C*, 118(34):19655–19660, 2014.

[57] Elizabeth S Parrott, Rebecca L Milot, Thomas Stergiopoulos, Henry J Snaith, Michael B Johnston, and Laura M Herz. Effect of structural phase transition on charge-carrier lifetimes and defects in $CH_3NH_3PbI_3$ perovskite. *The Journal of Physical Chemistry Letters*, 7(7):1321–1326, 2016.

[58] Yukari Takahashi, Rena Obara, Zheng-Zhong Lin, Yukihiro Takahashi, Toshio Naito, Tamotsu Inabe, Shoji Ishibashi, and Kiyoyuki Terakura. Charge-transport in tin-iodide perovskite $(CH_3NH_3)PbI_3$: origin of high conductivity. *Dalton Transactions*, 40(20):5563–5568, 2011.

[59] Feng Hao, Constantinos C. Stoumpos, Duyen Hanh Cao, Robert PH Chang, and Mercouri G. Kanatzidis. Lead-free solid-state organic-inorganic halide perovskite solar cells. *Nature Photonics*, 8(6):489–494, 2014.

[60] Giles E. Eperon, Samuel D. Stranks, Christopher Menelaou, Michael B. Johnston, Laura M. Herz, and Henry J. Snaith. Formamidinium lead trihalide: a broadly tunable perovskite for efficient planar heterojunction solar cells. *Energy & Environmental Science*, 7(3):982–988, 2014.

[61] Paolo Umari, Edoardo Mosconi, and Filippo De Angelis. Relativistic GW calculations on $CH_3NH_3PbI_3$ and $CH_3NH_3SnI_3$ perovskites for solar cell applications. *Scientific Reports*, 4:4467, 2014.

[62] Xujie Lü, Yonggang Wang, Constantinos C Stoumpos, Qingyang Hu, Xiaofeng Guo, Haijie Chen, Liuxiang Yang, Jesse S Smith, Wenge Yang, Yusheng Zhao, et al. Enhanced structural stability and photo responsiveness of $CH_3NH_3SnI_3$

perovskite via pressure-induced amorphization and recrystallization. *Advanced Materials*, 28(39):8663–8668, 2016.

[63] Eberhard Engel and Reiner M. Dreizler. *Density Functional Theory: An Advanced Course*. Springer Science & Business Media, 2011.

[64] J. Kohanoff. *Electronic Structure Calculations for Solids and Molecules: Theory and Computational Methods*. Cambridge University Press, 2006.

[65] D.J. Griffiths. *Introduction to Quantum Mechanics*. Pearson international edition. Pearson Prentice Hall, 2005.

[66] Richard M. Martin. *Electronic Structure: Basic Theory and Practical Methods*. Cambridge University Press, 2004.

[67] John C. Inkson. *Many-Body Theory of Solids: An Introduction*. Springer Science & Business Media, 2012.

[68] W. Koch and M.C. Holthausen. *A Chemist's Guide to Density Functional Theory*. Wiley, 2001.

[69] P. Ehrenfest. Bemerkung über die angenäherte gültigkeit der klassischen mechanik innerhalb der quantenmechanik. *Zeitschrift für Physik*, 45(7):455–457, Jul 1927.

[70] P. Güttinger. Das verhalten von atomen im magnetischen drehfeld. *Zeitschrift für Physik*, 73(3):169–184, Mar 1932.

[71] H. Hellmann. *Einführung in die Quantenchemie*. Franz Deuticke, 1937.

[72] R. P. Feynman. Forces in molecules. *Phys. Rev.*, 56:340–343, Aug 1939.

[73] John P. Perdew and Stefan Kurth. Density functionals for non-relativistic John Perdew Coulomb systems in the new century. In C. Fiolhais, F. Nogueira, and M.A.L. Marques, editors, *A Primer in Density Functional Theory*, Lecture Notes in Physics, pages 1–55. Springer Berlin Heidelberg, 2003.

[74] Pierre Hohenberg and Walter Kohn. Inhomogeneous electron gas. *Physical Review*, 136(3B):B864, 1964.

[75] Walter Kohn and Lu Jeu Sham. Self-consistent equations including exchange and correlation effects. *Physical Review*, 140(4A):A1133, 1965.

[76] R.G. Parr and Y. Weitao. *Density-Functional Theory of Atoms and Molecules*. International Series of Monographs on Chemistry. Oxford University Press, 1994.

[77] Mel Levy. Universal variational functionals of electron densities, first-order density matrices, and natural spin-orbitals and solution of the v-representability problem. *Proceedings of the National Academy of Sciences*, 76(12):6062–6065, 1979.

[78] Olle Gunnarsson and Bengt I Lundqvist. Exchange and correlation in atoms, molecules, and solids by the spin-density-functional formalism. *Physical Review B*, 13(10):4274, 1976.

[79] C. Kittel. *Introduction to Solid State Physics*. Wiley, 1996.

[80] Hendrik J. Monkhorst and James D. Pack. Special points for brillouin-zone integrations. *Phys. Rev. B*, 13:5188–5192, Jun 1976.

[81] Fernando Nogueira, Alberto Castro, and Miguel A. L. Marques. *A Tutorial on Density Functional Theory*, pages 218–256. Springer Berlin Heidelberg, Berlin, Heidelberg, 2003.

[82] M. C. Payne, M. P. Teter, D. C. Allan, T. A. Arias, and J. D. Joannopoulos. Iterative minimization techniques forab initiototal-energy calculations: molecular dynamics and conjugate gradients. *Reviews of Modern Physics*, 64(4):1045–1097, oct 1992.

[83] N. Troullier and José Luís Martins. Efficient pseudopotentials for plane-wave calculations. *Phys. Rev. B*, 43:1993–2006, Jan 1991.

[84] David Vanderbilt. Soft self-consistent pseudopotentials in a generalized eigenvalue formalism. *Phys. Rev. B*, 41:7892–7895, Apr 1990.

[85] Peter E. Blöchl. Projector augmented-wave method. *Physical Review B*, 50(24):17953, 1994.

[86] Georg Kresse and D. Joubert. From ultrasoft pseudopotentials to the projector augmented-wave method. *Physical Review B*, 59(3):1758, 1999.

[87] DR Hamann, M Schlüter, and C Chiang. Norm-conserving pseudopotentials. *Physical Review Letters*, 43(20):1494, 1979.

[88] NAW Holzwarth, GE Matthews, RB Dunning, AR Tackett, and Y Zeng. Comparison of the projector augmented-wave, pseudopotential, and linearized augmented-

plane-wave formalisms for density-functional calculations of solids. *Physical Review B*, 55(4):2005, 1997.

[89] John P Perdew and Karla Schmidt. Jacobs ladder of density functional approximations for the exchange-correlation energy. In *AIP Conference Proceedings*, volume 577, pages 1–20. AIP, 2001.

[90] Viktor N Staroverov, Gustavo E Scuseria, Jianmin Tao, and John P Perdew. Tests of a ladder of density functionals for bulk solids and surfaces. *Physical Review B*, 69(7):075102, 2004.

[91] John P Perdew, Adrienn Ruzsinszky, Jianmin Tao, Viktor N Staroverov, Gustavo E Scuseria, and Gábor I Csonka. Prescription for the design and selection of density functional approximations: More constraint satisfaction with fewer fits. *The Journal of chemical physics*, 123(6):062201, 2005.

[92] John P. Perdew, Kieron Burke, and Matthias Ernzerhof. Generalized gradient approximation made simple. *Physical Review Letters*, 77(18):3865, 1996.

[93] John P. Perdew, Adrienn Ruzsinszky, Gábor I. Csonka, Gustavo E. Vydrov, Oleg A .and Scuseria, Lucian A. Constantin, Xiaolan Zhou, and Kieron Burke. Restoring the density-gradient expansion for exchange in solids and surfaces. *Physical Review Letters*, 100(13):136406, 2008.

[94] Aliaksandr V Krukau, Oleg A Vydrov, Artur F Izmaylov, and Gustavo E Scuseria. Influence of the exchange screening parameter on the performance of screened hybrid functionals. *The Journal of chemical physics*, 125(22):224106, 2006.

[95] Axel D. Becke and Erin R. Johnson. A simple effective potential for exchange. *The Journal of Chemical Physics*, 124 22:221101, 2006.

[96] J.P. Dahl and J. Avery. *Local Density Approximations in Quantum Chemistry and Solid State Physics*. Springer US, 2013.

[97] Jianmin Tao, John P. Perdew, Viktor N. Staroverov, and Gustavo E. Scuseria. Climbing the density functional ladder: Nonempirical meta–generalized gradient approximation designed for molecules and solids. *Physical Review Letters*, 91(14):146401, 2003.

[98] Yan Zhao and Donald G Truhlar. A new local density functional for main-group thermochemistry, transition metal bonding, thermochemical kinetics, and noncovalent interactions. *The Journal of Chemical Physics*, 125(19):194101, 2006.

[99] Axel D Becke. A new mixing of hartree–fock and local density-functional theories. *The Journal of Chemical Physics*, 98(2):1372–1377, 1993.

[100] Axel D Becke. Density-functional thermochemistry. III. the role of exact exchange. *The Journal of Chemical Physics*, 98(7):5648–5652, 1993.

[101] P. J. Stephens, F. J. Devlin, C. F. N. Chabalowski, and Michael J. Frisch. Ab initio calculation of vibrational absorption and circular dichroism spectra using density functional force fields. *The Journal of Physical Chemistry*, 98(45):11623–11627, 1994.

[102] Carlo Adamo and Vincenzo Barone. Toward reliable density functional methods without adjustable parameters: The PBE0 model. *The Journal of Chemical Physics*, 110(13):6158–6170, 1999.

[103] Jochen Heyd, Gustavo E Scuseria, and Matthias Ernzerhof. Hybrid functionals based on a screened Coulomb potential. *The Journal of Chemical Physics*, 118(18):8207–8215, 2003.

[104] Wilfried G. Aulbur, Lars Jönsson, and John W. Wilkins. Quasiparticle calculations in solids. *Solid State Physics*, 54:1–218, 1999.

[105] M. S. H. Suleiman. *A Theoretical Investigation of Structural, Electronic and Optical Properties of some Group 10, 11 and 12 Transition-Metal Nitrides.* PhD Thesis, University of the Witwatersrand, 2013.

[106] C. Friedrich and A. Schindlmayr. Many-Body Perturbation Theory: The GW Approximation. In Johannes Grotendorst, Stefan Blügel, and Dominik Marx, editors, *Computational Nanoscience: Do It Yourself!*, NIC Series Volume 31, pages 335–355. John von Neumann Institute for Computing, Jülich, 2006.

[107] Xia Leng, Fan Jin, Min Wei, and Yuchen Ma. Gw method and bethe–salpeter equation for calculating electronic excitations. *Wiley Interdisciplinary Reviews: Computational Molecular Science*, 6(5):532–550, 2016.

[108] M Shishkin and G Kresse. Implementation and performance of the frequency-dependent g w method within the paw framework. *Physical Review B*, 74(3):035101, 2006.

[109] Lars Hedin. New method for calculating the one-particle Green's function with application to the electron-gas problem. *Physical Review*, 139(3A):A796, 1965.

[110] Judith Harl. *The Linear Response Function in Density Functional Theory*. PhD Thesis, Universität Wien, 2008.

[111] Linda Hung, Fabien Bruneval, Kopinjol Baishya, and Serdar Ogut. Benchmarking the gw approximation and bethe–salpeter equation for groups IB and IIB atoms and monoxides. *Journal of chemical theory and computation*, 13(5):2135–2146, 2017.

[112] Rex W Godby and Pablo García-González. Density functional theories and self-energy approaches. In *A Primer in Density Functional Theory*, pages 185–217. Springer, 2003.

[113] Giovanni Onida, Lucia Reining, and Angel Rubio. Electronic excitations: density-functional versus many-body Green's-function approaches. *Reviews of Modern Physics*, 74(2):601, 2002.

[114] John M. Ziman. *Principles of the Theory of Solids*. Cambridge University Press, 1972.

[115] Jasprit Singh. *Modern Physics for Engineers*. John Wiley & Sons, 2008.

[116] Giovanni Pizzi, Dmitri Volja, Boris Kozinsky, Marco Fornari, and Nicola Marzari. Boltzwann: A code for the evaluation of thermoelectric and electronic transport properties with a maximally-localized wannier functions basis. *Computer Physics Communications*, 185(1):422–429, 2014.

[117] T. J. Scheidemantel, C. Ambrosch Draxl, T. Thonhauser, J. V. Badding, and J. O. Sofo. Transport coefficients from first-principles calculations. *Physical Review B*, 68(12):125210, 2003.

[118] Terry M. Tritt, editor. *Thermal Conductivity: Theory, Properties, and Applications*. Springer Science & Business Media, 2005.

[119] Simen Nut Hansen Eliassen. A first principles study of lattice thermal conductivity in XNiSn (X= Ti, Zr, Hf) half-heusler alloys for thermoelectric applications. Master's Thesis, University of Oslo, 2016.

[120] N.W. Ashcroft and N.D. Mermin. *Solid State Physics*. HRW international editions. Holt, Rinehart and Winston, 1976.

[121] Ma Guadalupe Moreno-Armenta and Gerardo Soto. Stability and electronic structure of intrinsic and intercalated copper nitride alloys. *Solid State Sciences*, 10(5):573–579, 2008.

[122] Michael P. Marder. *Condensed Matter Physics*. John Wiley & Sons, 2010.

[123] S. Raju, E. Mohandas, and V. S. Raghunathan. The pressure derivative of bulk modulus of transition metals: an estimation using the method of model potentials and a study of the systematics. *Journal of Physics and Chemistry of Solids*, 58(9):1367–1373, 1997.

[124] Pascal Vinet, John R. Smith, John Ferrante, and James H. Rose. Temperature effects on the universal equation of state of solids. *Physical Review B*, 35(4):1945, 1987.

[125] Pascal Vinet, James H. Rose, John Ferrante, and John R. Smith. Universal features of the equation of state of solids. *Journal of Physics: Condensed Matter*, 1(11):1941, 1989.

[126] Francis Birch. Finite elastic strain of cubic crystals. *Physical Review*, 71(11):809, 1947.

[127] F. D. Murnaghan. On the theory of the tension of an elastic cylinder. *Proceedings of the National Academy of Sciences of the United States of America*, 30(12):382–384, 1944.

[128] Francis Birch. Finite strain isotherm and velocities for single-crystal and polycrystalline nacl at high pressures and 300 K. *Journal of Geophysical Research: Solid Earth*, 83(B3):1257–1268, 1978.

[129] Mahmud Abdulsalam. *A theoretical investigation of the structural, electronic and optical properties of transition metal chalcogenides*. PhD Thesis, University of the Witwatersrand, 2015.

[130] Yong-Hua Duan, Yong Sun, Ming-Jun Peng, and Zhong-Zheng Guo. First principles investigation of the binary intermetallics in Pb–Mg–Al alloy: Stability, elastic properties and electronic structure. *Solid State Sciences*, 13(2):455–459, 2011.

[131] Félix Mouhat and François-Xavier Coudert. Necessary and sufficient elastic stability conditions in various crystal systems. *Physical Review B*, 90(22):224104, 2014.

[132] W. Voigt. *Lehrbuch der Kristallphysik: mit Ausschluss der Kristalloptik*. B.G. Teubners Sammlung von Lehrbüchern auf dem Gebiete der mathematischen Wissenschaften mit Einschluss ihrer Anwendungen. J.W. Edwards, 1928.

[133] A. Reuss. Account of the liquid limit of mixed crystals on the basis of the plasticity condition for single crystal. *Zeitschrift fur Angewandte Mathematik und Mechanik*, 9:49–58, 1929.

[134] R. Hill. The elastic behaviour of a crystalline aggregate. *Proceedings of the Physical Society. Section A*, 65(5):349, 1952.

[135] P. Ravindran, Lars Fast, P. A. Korzhavyi, B. Johansson, J. Wills, and O. Eriksson. Density functional theory for calculation of elastic properties of orthorhombic crystals: Application to $TiSi_2$. *Journal of Applied Physics*, 84(9):4891–4904, 1998.

[136] Damien Connétable and Olivier Thomas. First-principles study of the structural, electronic, vibrational, and elastic properties of orthorhombic NiSi. *Physical Review B*, 79(9):094101, 2009.

[137] T Hammerschmidt, IA Abrikosov, D Alfe, SG Fries, Lars Höglund, MHG Jacobs, J Koßmann, X G Lu, and G Paul. Including the effects of pressure and stress in thermodynamic functions. *Physica Status Solidi (b)*, 251(1):81–96, 2014.

[138] GM Dongho Nguimdo, George S Manyali, Mahmud Abdusalam, and Daniel P Joubert. Structural stability and electronic properties of $AgInS_2$ under pressure. *The European Physical Journal B*, 89(4):90, 2016.

[139] GV SinKo and NA Smirnov. Ab initio calculations of elastic constants and thermodynamic properties of bcc, fcc, and hcp Al crystals under pressure. *Journal of Physics: Condensed Matter*, 14(29):6989, 2002.

[140] O Gomis, D Santamaría Pérez, J Ruiz Fuertes, JA Sans, R Vilaplana, HM Ortiz, B García-Domene, FJ Manjón, D Errandonea, P Rodríguez-Hernández, et al.

High-pressure structural and elastic properties of Tl_2O_3. *Journal of Applied Physics*, 116(13):133521, 2014.

[141] Atsushi Togo and Isao Tanaka. First principles phonon calculations in materials science. *Scripta Materialia*, 108:1 – 5, 2015.

[142] Martin T Dove and Martin T Dove. *Introduction to Lattice Dynamics*, volume 4. Cambridge university press, 1993.

[143] G Kresse, J Furthmüller, and J Hafner. Ab initio force constant approach to phonon dispersion relations of diamond and graphite. *EPL (Europhysics Letters)*, 32(9):729, 1995.

[144] Paolo Giannozzi, Stefano De Gironcoli, Pasquale Pavone, and Stefano Baroni. Ab initio calculation of phonon dispersions in semiconductors. *Physical Review B*, 43(9):7231, 1991.

[145] E. Kaxiras. *Atomic and Electronic Structure of Solids*. Cambridge University Press, 2003.

[146] Karlheinz Schwarz. Electrons. In A. Authier, editor, *International Tables for Crystallography Volume D: Physical properties of crystals*, pages 294–313. Springer Netherlands, Dordrecht, 2003.

[147] A. Filippetti, A. Mattoni, C. Caddeo, M. I. Saba, and P. Delugas. Low electron-polar optical phonon scattering as a fundamental aspect of carrier mobility in methylammonium lead halide $CH_3NH_3PbI_3$ perovskites. *Physical Chemistry Chemical Physics*, 18(22):15352–15362, 2016.

[148] Scheidemantel Ambrosch-Draxl, C Thonhauser, T Badding, and JO Sofo. Transport coefficients from first-principles calculation. *Phys. Rev. B*, 68:125210–1, 2003.

[149] Ivo Souza, Nicola Marzari, and David Vanderbilt. Maximally localized wannier functions for entangled energy bands. *Physical Review B*, 65(3):035109, 2001.

[150] Arash A. Mostofi, Jonathan R. Yates, Young-Su Lee, Ivo Souza, David Vanderbilt, and Nicola Marzari. wannier90: A tool for obtaining maximally-localised wannier functions. *Computer Physics Communications*, 178(9):685 – 699, 2008.

[151] Atsushi Togo, Laurent Chaput, and Isao Tanaka. Distributions of phonon lifetimes in brillouin zones. *Phys. Rev. B*, 91:094306, Mar 2015.

[152] So Hirata and Martin Head-Gordon. Time-dependent density functional theory within the tammdancoff approximation. *Chemical Physics Letters*, 314(3):291 – 299, 1999.

[153] Michael M. Broido and John G. Taylor. Bethe-salpeter equation. *Journal of Mathematical Physics*, 10(1):184–209, 1969.

[154] M. Gajdoš, K. Hummer, G. Kresse, J. Furthmüller, and F. Bechstedt. Linear optical properties in the projector-augmented wave methodology. *Physical Review B*, 73(4):045112, 2006.

[155] M. Bass and Optical Society of America. *Handbook of Optics: Fundamentals, techniques, and design*. Number v. 1 in Handbook of Optics. McGraw-Hill, 1994.

[156] Mohammed S. H. Suleiman and Daniel P. Joubert. Quantum mechanical ab initio calculations of the structural, electronic and optical properties of bulk gold nitrides. *The European Physical Journal B*, 88(11):305, 2015.

[157] Jie-Qiong Hu, Ming Xie, Yong Pan, You-Cai Yang, Man-Men Liu, and Ji-Ming Zhang. The electronic, elastic and structural properties of Pd–Zr intermetallic. *Computational Materials Science*, 51(1):1–6, 2012.

[158] S. F. Pugh. XCII. Relations between the elastic moduli and the plastic properties of polycrystalline pure metals. *The London, Edinburgh, and Dublin Philosophical Magazine and Journal of Science*, 45(367):823–843, 1954.

[159] Wan-Jian Yin, Tingting Shi, and Yanfa Yan. Unusual defect physics in $CH_3NH_3PbI_3$ perovskite solar cell absorber. *Applied Physics Letters*, 104(6):063903, 2014.

[160] Tianqi Zhao, Wen Shi, Jinyang Xi, Dong Wang, and Zhigang Shuai. Intrinsic and extrinsic charge transport in $CH_3NH_3PbI_3$ perovskites predicted from first-principles. *Scientific Reports*, 6:19968, 2016.

[161] Jacky Even, Laurent Pedesseau, Jean-Marc Jancu, and Claudine Katan. Importance of spin–orbit coupling in hybrid organic/inorganic perovskites for photovoltaic applications. *The Journal of Physical Chemistry Letters*, 4(17):2999–3005, 2013.

[162] Towfiq Ahmed, T. Salim, Y. M. Lam, Elbert E. M. Chia, and Jian-Xin Zhu. Optical properties of organometallic perovskite: An ab initio study using rela-

tivistic GW correction and Bethe-Salpeter equation. *EPL (Europhysics Letters)*, 108(6):67015, 2015.

[163] Bing Li, Yukinobu Kawakita, Yucheng Liu, Mingchao Wang, Masato Matsuura, Kaoru Shibata, Seiko Ohira-Kawamura, Takeshi Yamada, Shangchao Lin, Kenji Nakajima, et al. Polar rotor scattering as atomic-level origin of low mobility and thermal conductivity of perovskite $CH_3NH_3PbI_3$. *Nature Communications*, 8:16086, 2017.

[164] G. Jeffrey Snyder and Eric S. Toberer. Complex thermoelectric materials. *Nature Materials*, 7(2):105–114, 2008.

[165] S. Bagci, Battal G. Yalcin, H. A. Rahnamaye Aliabad, S. Duman, and B. Salmankurt. Structural, electronic, optical, vibrational and transport properties of $CuBX_2$ (X= S, Se, Te) chalcopyrites. *RSC Advances*, 6(64):59527–59540, 2016.

[166] Loredana Protesescu, Sergii Yakunin, Maryna I Bodnarchuk, Franziska Krieg, Riccarda Caputo, Christopher H Hendon, Ruo Xi Yang, Aron Walsh, and Maksym V Kovalenko. Nanocrystals of cesium lead halide perovskites ($CsPbX_3$, X= Cl, Br, and I): novel optoelectronic materials showing bright emission with wide color gamut. *Nano letters*, 15(6):3692–3696, 2015.

[167] John P Perdew and Mel Levy. Physical content of the exact kohn-sham orbital energies: band gaps and derivative discontinuities. *Physical Review Letters*, 51(20):1884, 1983.

[168] J. Thijssen. *Computational Physics*. Cambridge University Press, 2007.

[169] Klaus Capelle. A bird's-eye view of density-functional theory. *Brazilian Journal of Physics*, 36(4A):1318–1343, 2006.

[170] Georg Kresse and Jürgen Furthmüller. Efficient iterative schemes for ab initio total-energy calculations using a plane-wave basis set. *Physical Review B*, 54(16):11169, 1996.

[171] G. Kresse and J. Hafner. Ab initio molecular-dynamics simulation of the liquid-metal–amorphous-semiconductor transition in germanium. *Physical Review B*, 49(20):14251, 1994.

[172] Moise Guy Nguimdo, Dongho. *Computational study of chalcogenide based solar energy materials*. PhD Thesis, University of the Witwatersrand, 2016.